An Investigation of the g-factor of Graphene

By

Timothy J. Lyon

A dissertation submitted in partial fulfillment of

the requirements for the degree of

Doctor of Philosophy

(Physics)

at the

UNIVERSITY OF WISCONSIN - MADISON

2017

Date of final oral examination: 12/12/2016

The dissertation is approved by the following members of the Final Oral Committee:
Robert J. Joynt, Professor, Physics
Max Lagally, Professor, Physics
James Reardon, Director of Instructional Labs, Physics
Zhenqiang Ma, Professor, Electrical and Computer Engineering
Peter Timbe, Professor, Physics

© Copyright by Timothy Lyon 2016
All Rights Reserved

Acknowledgments

I would like to thank my advisor, Prof. Robert Blick, for all of his support and wisdom. With his help, I have obtained invaluable experience that will aid me in many ways for the rest of my life. I would also like to thank August Dorn who provided invaluable insight and guidance that helped me get my research done well and on time. Special thanks to Prof. Jack Ma and Prof. Bob Joynt for helping me with the USA side of things while I worked on my research in Germany. Thanks as well to Marta Prada who helped greatly with the theoretical aspects and gave clear explanations of confusing concepts.

It was a pleasure working with my friends from Hamburg. Jonas Sichau helped me to find a greater appreciation for the finer points of life in Hamburg while working with him in the lab on his master's degree, and Bojan Bosnjak was also a great help while assisting in the lab during his bachelor's.

My friends back in Michigan have also given me strength and inspiration and I appreciate all of their support. I want to thank Josh Hunt for his lifelong friendship, his proofreading, and his 3D rendering skills, a small fraction of which are on display in Fig. 4-3(b). I also thank Carl Miller for his proofreading abilities and his wisdom which led to many interesting conversations through the years.

I'll always remember my time with the friends I made in Madison. Grilling and gaming sessions with them were some of the best times of my life; I don't know how I could have survived the insanity of grad school without them. Special thanks to Chris Anderson for proofreading.

Last but not least I want to thank my mother, who I know I can depend on for anything, including her keen eye for proofreading. She has been my rock and my biggest inspiration because of her tenacity and strong spirit. I wouldn't have been able to make it this far without her.

Abstract

This work investigates one of the fundamental properties of monolayer graphene, the g-factor of its charge carriers. This is done through analysis of resistive electron spin resonance (ESR) measurements that were performed on large-area graphene devices in both flat and mechanically modulated configurations. Discussion of the results follows, highlighting possible origins for the observed phenomena.

New techniques for sample fabrication were developed to produce the samples used in these experiments, including a method for transferring ultra large-scale CVD-grown graphene sheets to arbitrary substrates. The resulting sample size using the processes outlined here can be as large as several cm^2. The samples produced and described in this work were constructed by transferring graphene onto SiO_2 substrates.

The fabrication process described here is highly effective at preventing damage to the graphene at every step, from the graphene transfer stage all the way through metal lift-off, allowing for near-ideal carrier mobilities and the observation of the quantum Hall effect. The charge-neutral point is shown to move drastically to near-zero gate voltage after a 2-step post-fabrication annealing process, which also allows for greatly diminished magnetic hysteresis.

The precise value of the g-factor in graphene is of fundamental interest for all spin-related properties and their application. We investigate monolayer graphene on a Si/SiO_2 substrate by resistively detected electron spin resonance (ESR). Surprisingly, the magnetic moment and corresponding g-factor of 1.952 ± 0.002 is insensitive to charge carrier type, concentration, and mobility.

Resistive ESR measurements were also performed on graphene that was deposited on a periodic SiO_2 substrate with trenches 18 nm deep and 100 nm long, separated by mesas of 100 nm length. In these measurements, the ESR peaks seen in flat graphene reappear and are joined by a second set of peaks that is argued to be attributed to zero-field pseudospin splitting. The possible role of spin-orbit coupling in determining the magnitude of this zero-field splitting is also discussed.

Contents

Acknowledgments **i**

Abstract **ii**

1 Introduction **1**

2 Theoretical background **5**

2.1 Elementary electronic concepts and properties 5

2.1.1 Electronic structure of monolayer graphene 5

2.1.2 Pseudospin 9

2.1.3 Landau levels 10

2.1.4 Density of states 11

2.1.5 Capacitance 12

2.1.6 Wigner-Seitz radius 13

2.2 Magnetoresistance 14

2.2.1 Hall and quantum Hall effects 14

2.2.2 Shubnikov-de Haas effect 17

2.2.3 Two carrier transport 18

2.2.4 Weak localization 19

2.3 Electron spin resonance (ESR) 22

2.4 Spin relaxation mechanisms 24

2.5 Charged impurity concentration 25

2.6 Defects 26
2.7 Raman spectroscopy 27
2.8 Growth by chemical vapor deposition (CVD) 30

3 Sample fabrication and preparation 32
3.1 Graphene preparation 32
3.2 Substrate preparation 36
3.2.1 Wafer dicing 36
3.2.2 Substrate patterning 37
3.3 Graphene transfer 38
3.4 Metal contacts 42
3.5 Defining the graphene area 44
3.6 Sample mounting and bonding 45
3.7 Thermal annealing 50

4 Measurement setup 51
4.1 Leakage tests 51
4.2 Cryostat 52
4.3 Resistive measurements 52
4.3.1 Annealing monitoring 52
4.3.2 Electrical contact resistance 54
4.3.3 Magnetotransport 54
4.3.4 Microwave-induced ESR 55
4.4 Data acquisition and analysis 58

5 Large area graphene characterization 59
5.1 Raman analysis 59
5.2 Annealing 61
5.3 Magnetotransport 64
5.3.1 Transport properties 64

5.3.2 Quantum Hall levels 67
5.3.3 Weak localization 67
5.4 Capacitance 70
5.5 Charged impurities 74

6 The *g*-factor of graphene **75**
6.1 ESR measurements 75
6.2 g-factor origins 82
6.3 Spin lifetime 85
6.4 Further analysis 91

7 Graphene on a periodic substrate **92**
7.1 Secondary ESR peaks 92
7.2 Background 94
7.3 Hamiltonian 95
7.4 Analysis 99

8 Conclusions and outlook **104**

A Sample preparation recipes **106**
A.1 Graphene preparation 106
A.1.1 Coat with PMMA 106
A.1.2 Copper removal and cleaning 106
A.2 Transferring graphene 107
A.2.1 Substrate preparation 107
A.2.2 Move to substrate 108
A.2.3 PMMA Removal 108
A.3 Photolithography 108
A.3.1 Metal contacts 108
A.3.2 Contact deposit and lift-off 109

A.3.3 Hall bar 109
A.4 E-beam lithography 110
A.4.1 Alignment markers 110
A.4.2 E-beam lithography recipes 110
A.5 Thermal annealing 111

B List of samples **112**

C Lists of symbols **113**

Bibliography **115**

List of Figures

2-1 Lattice structure of graphene 6
2-2 Dispersion relation of graphene 8
2-3 Hall bar diagram with quantum Hall effect 14
2-4 Zeeman splitting due to ESR 23
2-5 Diagram of vacancy and adatom defects 27
2-6 Raman defect spectra 29
2-7 CVD growth process 31

3-1 Step-by-step diagram for graphene sample fabrication 33
3-2 1.92 mm graphene Hall bar 34
3-3 Photographs of graphene in various fabrication steps 35
3-4 Trench pattern made with e-beam lithography 38
3-5 Detailed steps for graphene transfer and contact deposition. 39
3-6 Large-area graphene converage of 4 µm period test pattern, 1.8 mm long 40
3-7 SEM scans of transferred graphene on trenches 41
3-8 Photomask design for Hall bar contacts 43
3-9 Photomask for defining the graphene bar 45
3-10 First photo of bonded flat 200 µm Hall bar used in g-factor experiments 47
3-11 Second photo of flat 200 µm Hall bar used in g-factor experiments . . 48
3-12 Photo of 200 µm Hall bar with 200 nm period 49

4-1 Cryostat diagram 53

4-2 Dual lock-in measurement setup 55
4-3 Photograph and schematic of sample in measurement setup 56

5-1 Raman measurement spectra of transferred graphene 60
5-2 Change in longitudinal resistance due to baking 62
5-3 Graph of carrier density and mobility vs. gate voltage 65
5-4 Evidence of quantum Hall levels seen in resistance measurements . . . 68
5-5 Plateaus in Hall conductance as evidence of the quantum Hall effect . 69
5-6 Weak localization peak fits 71
5-7 Anderson localization lengths derived from WL peak fits 72
5-8 Phase coherence and elastic scattering lengths derived from WL peak fits 73

6-1 Example of measurements with and without incident RF power to calculate ΔR_{xx} 77
6-2 Graph showing ΔR_{xx} for a range of incident RF power 78
6-3 ΔR_{xx} for a range of frequencies at V_{CNP} 80
6-4 g-factor results from ESR studies on graphene for a range of charge carrier densities 81
6-5 ESR peak widths, varying incident RF power with constant charge carrier density and incident RF frequency 86
6-6 ESR peak widths, varying incident RF frequency with constant charge carrier density and RF power 87
6-7 ESR peak widths, varying charge carrier density by adjusting back gate voltage, and with constant RF power and frequency 88
6-8 ESR peak fits 89
6-9 ESR peak fits, scaled for comparison 90

7-1 Pattern with 200 nm period etched on SiO_2 93
7-2 Projection of ESR signal amplitude for graphene on a periodic substrate displaying two sets of resonance. 96

7-3 Line fits for primary (spin) and secondary (pseudospin) ESR peaks . 97
7-4 Possible band structures consider spin-orbit coupling 100
7-5 Spin and pseudospin splitting transitions 101

List of Tables

5.1 Graphene defect properties calculated from Raman measurements . . 61
5.2 Calculated values from magnetoresistance measurements 67

6.1 ESR peak locations 79
6.2 Relevant systems with a g-factor near 2 85

B.1 List of samples 112

C.1 Physical constants 113
C.2 Abbreviations of common terms 114

Chapter 1

Introduction

Graphene is well-known for its desirable electrical properties [116], and with all of the intense focus on research in the material, new applications are constantly being discovered. While graphene is known to have its best electrical properties when it is single-crystalline and suspended [11, 31], those attributes are currently not feasibly attainable for mass-produced devices. There have been very exciting developments related to improving non-suspended graphene's mobility on more exotic substrates such as h-BN [29, 170, 5], as well as improving the chemical vapor deposition (CVD) growth process for producing better quality devices with large grain sizes [127, 168, 5]. However, these developments are currently difficult to scale up and automate.

On the other hand, CVD-grown graphene is still the best way to repeatably produce large areas of monolayer graphene, and SiO_2 is a well-known substrate that is already integrated into many processes from semiconductor physics to MEMS [13, 174], and beyond. Previous work has shown how to transfer large areas of CVD-grown graphene onto arbitrary substrates [86, 149, 146, 130] and remove contaminants [86, 55]. However, previous CVD-grown graphene on SiO_2 devices do not combine the desirable properties of high enough quality electrical characteristics to display the quantum Hall effect (QHE), a charge neutral point (CNP) near zero gate voltage, and a large device size, with typical finished devices being on the order of $10\,\mu m$ [150]. Large-scale

integration of easily manufactured, high-quality graphene devices is desirable in many different applications, such as graphene transistors, broadband optical modulators [88] and THz antennas [154].

Challenges arise when fabricating high-quality CVD-grown graphene devices, primarily due to contaminants of all kinds easily attaching to graphene. With each step, much care must be taken to remove any existing organic or inorganic contaminants on the graphene as well as prevent new contaminants from being attached. This thesis presents a fabrication method that produces devices with CVD-grown graphene on SiO_2 that are hundreds of microns in size and display the QHE. Samples made using this method are used in the experiments described later.

Graphene is widely recognized as a promising material for spintronics applications due to its many favorable properties, such as tunable charge carrier concentration, high electronic mobility, and long spin diffusion lengths [177, 160, 158, 18, 51, 136]. Initial theoretical investigations into spin relaxation [34] for pristine graphene predicted microsecond spin lifetimes, but experimental results have so far been orders of magnitude shorter [158, 157, 53, 133, 66, 128, 50, 64].

Although one may at first expect graphene to be nonmagnetic, evidence of magnetic impurities in graphene has been observed experimentally in a number of ways, including the Kondo effect [40, 24]. Resistively detected [148] spin resonance [97, 115, 58] from microwave photo-excited transport on graphene was pioneered by Mani *et al.* [95] on epitaxially grown [8, 27, 9] samples. This initial investigation provided valuable insights into electron spin resonance in graphene and allowed for the calculation of a magnetic moment and associated g-factor.

In this work we extend the investigation of resistively detected electron spin resonance in graphene to include different charge carrier types, densities, and mobilities, by employing a transistor geometry. We also perform ESR measurements on mechanically modulated graphene and observe peaks that we allege arise due to pseudospin splitting. These peaks are visible at a higher temperature than might be expected, possibly due

to effects caused by the modulation of the graphene.

The remaining chapters of this thesis are organized as follows:

- Chapter 2, *Theoretical background*, is a reference to various important concepts used in this work.
- Chapter 3, *Sample fabrication and preparation*, describes the fabrication methods for all samples used in this research.
- Chapter 4, *Measurement setup*, presents the equipment used for the measurements in the rest of this thesis and how it is used to test, characterize, and measure the samples made using the techniques presented in Ch. 3.
- Chapter 5, *Large area graphene characterization*, analyzes the characteristics of a 200 μm long graphene bar that was made using fabrication techniques described in Ch. 3. This includes investigations of the impurity concentrations from Raman analysis and a self-consistent formalism, performing weak localization analysis, and derivations of parameters found with magnetotransport measurements.
- Chapter 6, *The g-factor of graphene*, presents the results of ESR measurements for a flat graphene sample at various carrier densities and a derivation of the associated g-factors and spin lifetimes. An investigation into the origin of the g-factor is also presented.
- Chapter 7, *Graphene on a periodic substrate*, analyzes the g-factors found on a mechanically modulated graphene sample due to two sets of peaks and investigates possible theoretical explanations for these phenomena.
- Chapter 8, *Conclusions and outlook*, summarizes the results of this work and discusses the next steps in this research.

Some of the results discussed in this thesis can be found in writings that have been submitted for publication and are currently in the review process. The sample

fabrication process, as well as observation of the quantum Hall effect in a large-area graphene device on a SiO2 substrate, are found in [92], while the electron spin resonance (ESR) measurements and g-factor analysis on a flat graphene sample are reported in [91]. The results of completed and anticipated ESR experiments on mechanically modulated graphene as well as a theoretical analysis of zero-field pseudospin splitting and its origin will appear in a future publication.

Chapter 2

Theoretical background

This chapter outlines the theoretical background for the work described in this thesis and begins with a description of the unique electronic properties of monolayer graphene. The remaining sections delineate the different concepts necessary for understanding the measurements and analysis in the following chapters.

2.1 Elementary electronic concepts and properties

2.1.1 Electronic structure of monolayer graphene

Graphene is a truly two-dimensional material, made out of carbon atoms in a hexagonal or "honeycomb" lattice, which can be modeled as two interleaving triangular sublattices, as shown in Fig. 2-1(a). The electronic structure of graphene is heavily dependent on each carbon atom being sp^2 hybridized, which happens when one $2s$ orbital is combined with two of the three available $2p$ orbitals. The hybridized orbitals of each atom overlap with those of their neighbors resulting in σ-bonds, and the remaining p orbital forms an out-of-plane π-bond [116, 139].

To analyze the electronic properties of graphene, we begin by applying a tight-binding approach as described in Neto *et al.* [116] which is summarized below. The inter-carbon atom distance in graphene is $a \approx 1.42$ Å, and the real-space lattice vectors

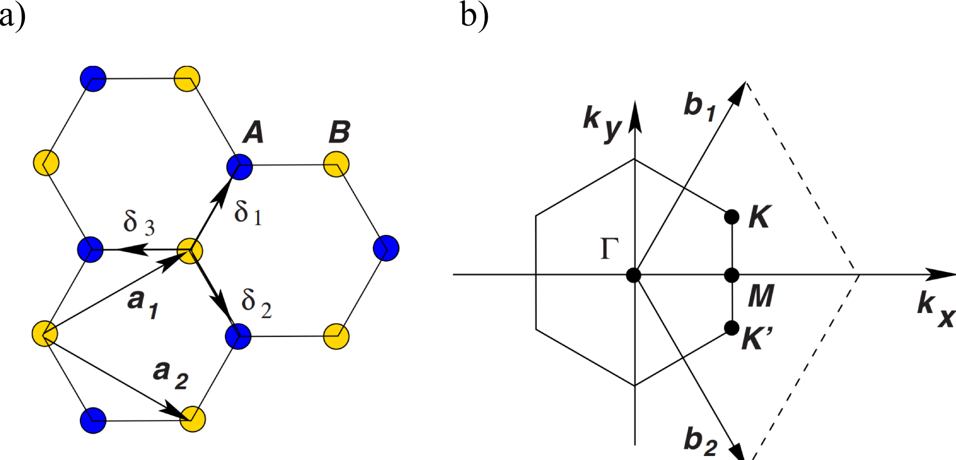

Figure 2-1: (a) Lattice structure of graphene, with A and B triangular sublattices. (b) The momentum-space Brillouin zone, with Dirac cones at the K and K' points. (Adapted with permission from Neto *et al.* [116], copyrighted by the American Physical Society.)

are written as

$$\boldsymbol{a}_1 = \frac{a}{2}\left(3, \sqrt{3}\right),\ \boldsymbol{a}_2 = \frac{a}{2}\left(3, -\sqrt{3}\right), \tag{2.1}$$

the reciprocal lattice vectors are represented by

$$\boldsymbol{b}_1 = \frac{2\pi}{3a}\left(1, \sqrt{3}\right),\ \boldsymbol{b}_2 = \frac{2\pi}{3a}\left(1, -\sqrt{3}\right), \tag{2.2}$$

and the Dirac points located in momentum space at the K and K' points given by

$$\boldsymbol{K} = \left(\frac{2\pi}{3}, \frac{2\pi}{3a\sqrt{3}}\right),\ \boldsymbol{K'} = \left(\frac{2\pi}{3}, -\frac{2\pi}{3a\sqrt{3}}\right). \tag{2.3}$$

The nearest-neighbor real-space vectors are written as

$$\boldsymbol{\delta}_1 = \frac{a}{2}\left(1, \sqrt{3}\right),\ \boldsymbol{\delta}_2 = \frac{a}{2}\left(1, -\sqrt{3}\right),\ \boldsymbol{\delta}_3 = -a\left(1, 0\right), \tag{2.4}$$

and the second-nearest-neighbors are

$$\boldsymbol{\delta}'_1 = \pm\boldsymbol{a}_1,\ \boldsymbol{\delta}'_2 = \pm\boldsymbol{a}_2,\ \boldsymbol{\delta}'_3 = \pm\left(\boldsymbol{a}_2 - \boldsymbol{a}_1\right). \tag{2.5}$$

A tight-binding Hamiltonian to model electrons hopping to nearest-neighbor and second-nearest-neighbor atoms is written as

$$\hat{H} = -t \sum_{\langle i,j \rangle,\sigma} \left(a^{\dagger}_{\sigma,i} b_{\sigma,j} + H.c. \right) - t' \sum_{\langle\langle i,j \rangle\rangle,\sigma} \left(a^{\dagger}_{\sigma,i} a_{\sigma,j} + b^{\dagger}_{\sigma,i} b_{\sigma,j} + H.c. \right). \tag{2.6}$$

The operator $a_{i,\sigma}$ ($a^{\dagger}_{i,\sigma}$) annihilates (creates) an electron on sublattice A on site $\boldsymbol{R}_i$ with spin $\sigma = (\uparrow, \downarrow)$. Similarly, $b_{i,\sigma}$ and $b^{\dagger}_{i,\sigma}$ are electron annihilation and creation operators for sublattice B. The energy to hop between nearest-neighbor atoms in different sublattices is $t \approx 2.8\,\mathrm{eV}$ and t' is the second-nearest-neighbor hopping energy between atoms in the same sublattice (not well known, but $0.02t \leq t' \leq 0.2t$) [116]. This Hamiltonian results in upper $(+, \pi)$ and lower $(-, \pi^*)$ bands represented by

$$\begin{aligned} E_{\pm}(\boldsymbol{k}) &= \pm t \sqrt{3 + f(\boldsymbol{k})} - t' f(\boldsymbol{k}), \\ f(\boldsymbol{k}) &= 2\cos\left(\sqrt{3} k_y a\right) + 4 \cos\left(\frac{\sqrt{3}}{2} k_y a\right) \cos\left(\frac{3}{2} k_x a\right). \end{aligned} \tag{2.7}$$

The Schrödinger equation in the region around one of the Dirac points, K, becomes

$$v_{\mathrm{F}} \hat{\boldsymbol{\sigma}} \cdot \boldsymbol{p} \Psi(\boldsymbol{r}) = E \Psi(\boldsymbol{r}), \tag{2.8}$$

which corresponds with the low-energy effective Dirac Hamiltonian [139]

$$\hat{H} = \hbar v_{\mathrm{F}} \hat{\boldsymbol{\sigma}} \cdot \boldsymbol{q} = \hbar v_{\mathrm{F}} \begin{pmatrix} 0 & q_x - \mathrm{i} q_y \\ q_x + \mathrm{i} q_y & 0 \end{pmatrix} \tag{2.9}$$

where $\hat{\boldsymbol{\sigma}} = (\hat{\sigma}_x, \hat{\sigma}_y)$ represents the Pauli spin matrices, $\boldsymbol{p} = (p_x, p_y)$, $\boldsymbol{q}$ is the 2D momentum vector relative to $\boldsymbol{K}$ ($\boldsymbol{k} = \boldsymbol{K} + \boldsymbol{q}$ and $|\boldsymbol{q}| \ll |\boldsymbol{K}|$), and $v_{\mathrm{F}} = 3ta/2 \approx 1 \times 10^{6}\,\mathrm{m\,s^{-1}}$ is the Fermi velocity. The energies in this linear region are

$$E_{\pm}(\boldsymbol{q}) \approx \pm \hbar v_{\mathrm{F}} |\boldsymbol{q}| \tag{2.10}$$

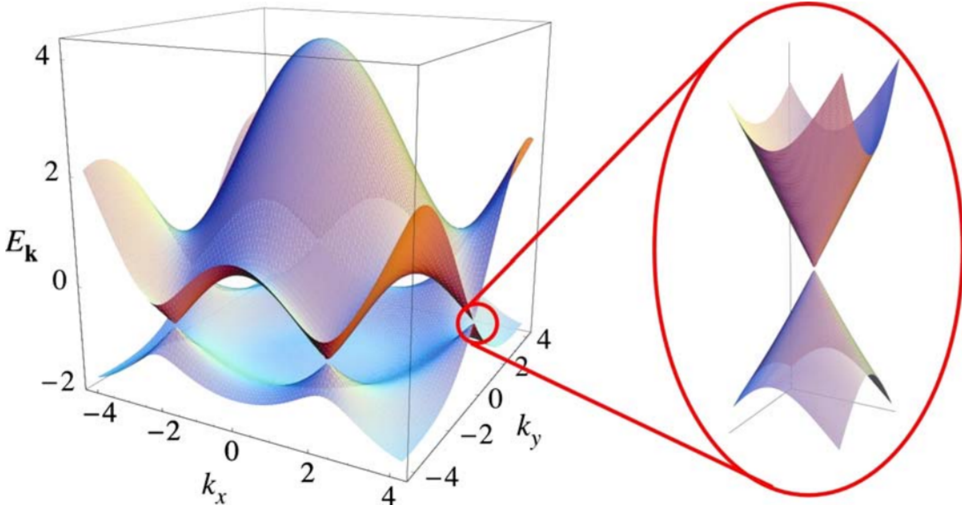

Figure 2-2: Dispersion relation of monolayer graphene. Right: Zoomed in linear region around a Dirac point. (Adapted with permission from Neto *et al.* [116], copyrighted by the American Physical Society.)

in the conduction (+) and valence (−) bands. A similar solution is found around K'.

The charge carriers that follow this equation are called Dirac fermions, which have an effective mass of zero at the Dirac points. The Fermi momentum in this regime is written as

$$k_{\mathrm{F}} = \sqrt{\frac{4\pi n}{g_{\mathrm{s}} g_{\mathrm{v}}}} = \sqrt{\pi n} \tag{2.11}$$

where $g_{\mathrm{s}} = 2$ is the spin degeneracy and $g_{\mathrm{v}} = 2$ is the valley degeneracy.

The Fermi wavelength is defined as

$$\lambda_{\mathrm{F}} = \sqrt{\frac{2\pi}{n}}. \tag{2.12}$$

This length scale is important to keep in mind when considering the sizes of the device structures being measured. Quantum mechanical confinement energies become important if any patterned structures approach this size. The largest Fermi wavelength measured in this thesis is ~63 nm, which is well below any of the dimensions of the large, flat Hall bars presented here, but close to the size of mesas and valleys in the wiggled sample measured in Ch. 7.

2.1.2 Pseudospin

If we consider the Hamiltonian in Eq. 2.6 in $\boldsymbol{k}$-space with $t' = 0$, after some derivation we find a two-component electron wave function that obeys the 2D Dirac equation (Eq. 2.8). The effective Hamiltonian is actually composed of two copies of this Dirac-like Hamiltonian for massless particles around the Dirac points, K and K', written as

$$\begin{aligned} \hat{H}^0_K &\cong \hbar v_{\mathrm{F}} \hat{\boldsymbol{\sigma}} \cdot \boldsymbol{q} \quad \text{with} \quad \boldsymbol{q} = \boldsymbol{K} - \boldsymbol{k}, \\ \hat{H}^0_{K'} &\cong \hbar v_{\mathrm{F}} \hat{\boldsymbol{\sigma}}^* \cdot \boldsymbol{q} \quad \text{with} \quad \boldsymbol{q} = \boldsymbol{K}' - \boldsymbol{k}, \end{aligned} \tag{2.13}$$

and with the Pauli matrices $\hat{\boldsymbol{\sigma}} = (\hat{\sigma}_x, \hat{\sigma}_y)$ and $\hat{\boldsymbol{\sigma}}^* = (\hat{\sigma}_x, -\hat{\sigma}_y)$. Now we solve for the eigenstates around $\boldsymbol{K}$ by writing

$$\hat{H}^0_K = \begin{pmatrix} 0 & \alpha^* \\ \alpha & 0 \end{pmatrix} \tag{2.14}$$

where $\alpha = \hbar v_{\mathrm{F}} q \mathrm{e}^{-\mathrm{i}\theta_q}$ and $\theta_q = \arctan\left(\frac{q_y}{q_x}\right)$. The eigenvectors are then

$$\Psi^{\pm} = \frac{1}{\sqrt{2}} \begin{pmatrix} \mathrm{e}^{\mathrm{i}\theta_q/2} \\ \pm\mathrm{e}^{-\mathrm{i}\theta_q/2} \end{pmatrix} \tag{2.15}$$

with the eigenvalues $\varepsilon = \pm|\alpha|$.

When we apply the rotation operator with 2π as the rotation angle, we find

$$\hat{R}^k_{2\pi} \Psi^{\pm} = \frac{1}{\sqrt{2}} \begin{pmatrix} \mathrm{e}^{\mathrm{i}(\theta_q + 2\pi)/2} \\ \pm\mathrm{e}^{-\mathrm{i}(\theta_q + 2\pi)/2} \end{pmatrix} = -\Psi^{\pm}, \tag{2.16}$$

which is simply the wave function changing phase by π as well as the eigenvectors for $\hat{H}^0_{K'}$. This change in phase is known as Berry's phase. The sublattice basis is called the pseudospin due to its spin-like behavior.

2.1.3 Landau levels

When discussing magnetic fields being applied perpendicularly to a 2D system, it is useful to define a quantity called the magnetic length, which is defined as the smallest radius of a circular orbit allowed by the uncertainty principle and is written as

$$l_{\mathrm{B}} = \sqrt{\frac{\hbar}{eB}} \tag{2.17}$$

where e is the elementary charge, $\hbar$ is the reduced Planck's constant, and B is the magnetic field. The cyclotron frequency of these orbits is defined as

$$\omega_{\mathrm{c}} = \sqrt{2}\frac{v_{\mathrm{F}}}{l_{\mathrm{B}}} = v_{\mathrm{F}}\sqrt{\frac{2eB}{\hbar}}. \tag{2.18}$$

where v_{F} is the Fermi velocity and the factor of $\sqrt{2}$ comes from the quantization of the system [116].

We now couple the free charge carriers to the electromagnetic field by minimal coupling and modify the Dirac equation (Eq. 2.8) to find

$$v_{\mathrm{F}}\left[\boldsymbol{\sigma}\cdot\left(\boldsymbol{p}+e\boldsymbol{A}\right)\right]\psi\left(\boldsymbol{r}\right) = E\psi\left(\boldsymbol{r}\right), \tag{2.19}$$

where $\boldsymbol{A}$ is the magnetic vector potential using the Landau gauge ($\boldsymbol{A} = B\left(-y, 0\right)$) and $\boldsymbol{B} = \boldsymbol{\nabla}\times\boldsymbol{A}$. The Landau level energies are found to be

$$E_N = \pm\hbar\omega_{\mathrm{c}} = \mathrm{sgn}\left(N\right)\sqrt{2e\hbar v_{\mathrm{F}}^2 B|N|} \tag{2.20}$$

where N is an integer representing an electron-like ($N > 0$) or hole-like ($N < 0$) index, with a Landau level at $N = 0$ that has both electron and hole features. This energy spectrum is the same at the K and K' points. Note that the energy levels are not linearly spaced, allowing the observation of the quantum Hall effect even at room temperature [119].

The degeneracy of the Landau states takes the form

$$g_{\mathrm{L}} = g_{\mathrm{s}} g_{\mathrm{v}} \frac{B}{\phi_0} = \frac{4eB}{h} \tag{2.21}$$

where $\phi_0 = h/e$ is the Dirac flux quantum. The number of occupied Landau levels is known as the filling factor, ν, and is written as

$$\nu = \frac{n}{g_{\mathrm{L}}} = \frac{hn}{4eB} \tag{2.22}$$

where n is the charge carrier density of graphene. From this relation, we can clearly see that higher magnetic fields reduce the number of occupied Landau levels.

2.1.4 Density of states

Most of the interest in graphene transport properties is in the low carrier density regime, with the charge carriers close to the Dirac points of the band structure. In this regime, the energy-momentum relationship is linear, with conduction and valence bands intersecting at $q = 0$. In this region, we can write the Fermi energy E_{F} in terms of the Fermi momentum by

$$E_{\mathrm{F}} = \hbar v_{\mathrm{F}} k_{\mathrm{F}} = \hbar v_{\mathrm{F}} \sqrt{\pi n}, \tag{2.23}$$

which by convention is positive for electrons and negative for holes. As shown earlier, graphene is estimated to have $v_{\mathrm{F}} \approx 1 \times 10^{6}\,\mathrm{m\,s^{-1}}$ in an empty band with no carriers, with slight modifications to this number with increased charge carrier density due to interaction effects.

The density of states of graphene near the Dirac points is

$$D(E) = \frac{\mathrm{d}n}{\mathrm{d}E} = \frac{g_{\mathrm{s}} g_{\mathrm{v}} E}{2\pi(\hbar v_{\mathrm{F}})^2} = \frac{2E}{\pi(\hbar v_{\mathrm{F}})^2}, \tag{2.24}$$

and when at the Fermi level,

$$D_0 = D\left(E_{\mathrm{F}}\right) = \frac{\sqrt{g_{\mathrm{s}} g_{\mathrm{v}} n}}{\hbar v_{\mathrm{F}} \sqrt{\pi}} = \frac{2}{\hbar v_{\mathrm{F}}} \sqrt{\frac{n}{\pi}}. \tag{2.25}$$

2.1.5 Capacitance

Electrostatic capacitance due to a graphene layer on an oxide with a back gate is typically represented as a capacitance per unit area by the equation

$$C_{\mathrm{ox}} = \frac{\kappa \varepsilon_0}{t_{\mathrm{ox}}} \tag{2.26}$$

where κ is the relative permittivity of the gate oxide, ε_0 is the permittivity of free space, and t_{ox} is the oxide thickness. For the SiO_2 samples used in this work, $t_{\mathrm{ox}} = 300\,\mathrm{nm}$ and $\kappa = 3.9$, so $C_{\mathrm{ox}} = 1.15\,\mathrm{F\,m^{-2}}$. This geometrically defined capacitance is not the only capacitance in the system, however.

If we model our system as a parallel plate capacitor, the first plate is degenerately doped silicon, essentially behaving as a metal, and the second plate is graphene. The graphene plate is a two-dimensional system with a much lower density of states than the metallic side, so the effects of band filling and emptying must be considered. This is a consequence of the Pauli exclusion principle requiring more and more energy to fill higher occupation levels.

As described by Xia *et al.*, the quantum capacitance in graphene can be written as

$$C_{\mathrm{Q}} = \frac{2e^2}{\hbar v_{\mathrm{F}} \sqrt{\pi}} \sqrt{n} \tag{2.27}$$

when $E_{\mathrm{F}} \gg k_{\mathrm{B}} T$ and can be modeled as being in series with the geometric oxide capacitance [167].

As we can note from above, as t_{ox} increases, C_{ox} decreases and beyond a certain point becomes the dominant capacitance in the system, causing the charge carrier density dependence on gate voltage to become linear away from the charge neutral

point (CNP). Capacitance near the CNP becomes rounded due to electron and hole puddles induced by charged impurities in the substrate. The linear region can be modeled by the relation [65]

$$n = \alpha \left(V_{\mathrm{g}} - V_{\mathrm{CNP}}\right) \tag{2.28}$$

where α is a linear factor that is dominated by the gate capacitance, but may differ from the theoretical geometric capacitance due to other parasitic capacitances in the system such as charge traps at the substrate/graphene interface.

The total capacitance per unit area can then be calculated by

$$C_{\mathrm{tot}} = \alpha e. \tag{2.29}$$

2.1.6 Wigner-Seitz radius

The Wigner-Seitz radius, also known as the interaction parameter and the effective fine structure constant, is found by dividing the electric potential energy between electrons by the Fermi energy [139]. It is a dimensionless quantity that allows us to estimate if the Coulomb interaction between electrons is significant. This parameter is denoted by r_{s} and does not depend on charge carrier density or effective mass in monolayer graphene due to its linear dispersion relation and is defined as

$$r_{\mathrm{s}} = \frac{e^2}{\varepsilon_0 \left(\kappa_1 + \kappa_2\right) h v_{\mathrm{F}}} \tag{2.30}$$

where κ_1 and κ_2 are the relative permittivities of the materials on each side of the graphene. Using $\kappa_1 = 3.9$ for SiO_2, $\kappa_2 = 1$ for vacuum, and $v_{\mathrm{F}} = 1.1 \times 10^6\,\mathrm{m\,s^{-1}}$ as a typical Fermi velocity for graphene on SiO_2 results in $r_{\mathrm{s}} \approx 0.8$ [139]. In fact, the entire range of possible values in monolayer graphene is $0 \leq r_{\mathrm{s}} \leq 2.2$ and in general, the charge carriers are always relatively weakly interacting compared to 2DEG systems [139].

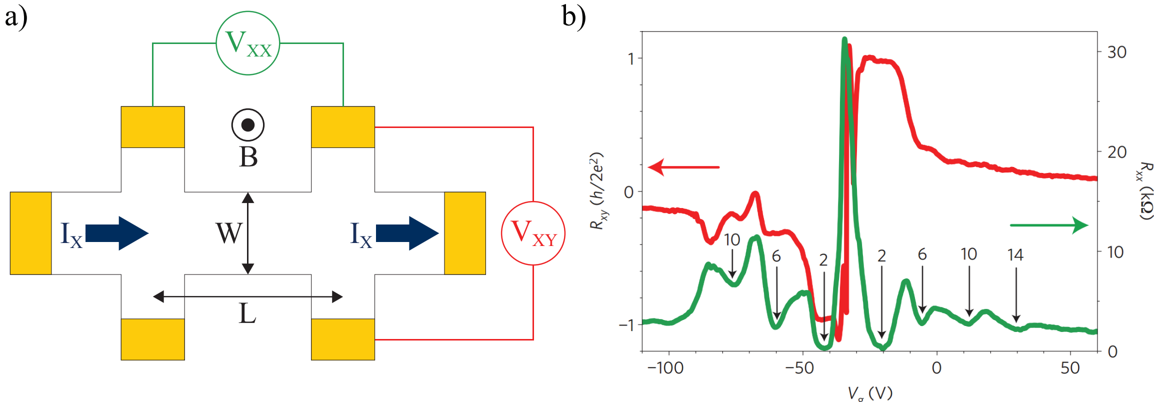

Figure 2-3: (a) Hall bar configuration, with applied current I_x, measured voltages V_{xx} and V_{xy}, and distances W and L labeled. (b) R_{xx} and R_{xy} for a clean single layer of graphene at $T = 1.5\,\mathrm{K}$ and $B = 9\,\mathrm{T}$, with quantum Hall levels with filling factors labeled, in a clean single layer of graphene (adapted with permission from Yang *et al.* [169], copyrighted by Nature Publishing Group).

2.2 Magnetoresistance

Magnetoresistance measurements determine the dependence of the electrical resistance of a material placed in an external magnetic field and are a standard way to characterize a 2-dimensional system. This is typically done with a Hall bar geometry by running a current I_x through the sample while measuring V_{xx} and V_{xy}, which are the electric potentials between the pairs of longitudinal contacts and the Hall contacts, respectively, and applying a strong magnetic field perpendicular to the current direction and the sample surface, as seen in Fig. 2-3(a).

2.2.1 Hall and quantum Hall effects

When a magnetic field is applied in a direction perpendicular to the flow of current through a conductor a transverse force pushes the charge carriers to one side of the conductor, generating a measurable voltage difference across the two sides. In a

two-dimensional material such as graphene the longitudinal resistivity is

$$\rho_{xx} = \frac{W}{L}\frac{V_{xx}}{I_x} \tag{2.31}$$

and the Hall resistivity is

$$\rho_{xy} = \frac{V_{xy}}{I_x} \tag{2.32}$$

where W and L are the physical dimensions of the bar as shown in Fig. 2-3(a). Note that in two dimensions, resistance (conductance) and resistivity (conductivity) both have units of Ohms (Siemens) and are commonly used interchangeably in the literature. In general, ρ (resistivity) and σ (conductivity) will be used in this work for theoretical purposes while R (resistance) and G (conductance) will be used for experimental results.

From the classical Hall effect, we can determine charge carrier density and mobility of the sample with the relations

$$n = \frac{B}{e\rho_{xy}} = \left(e\frac{\mathrm{d}\rho_{xy}}{\mathrm{d}B}\right)^{-1} \tag{2.33}$$

and

$$\mu = \frac{1}{en\rho_{xx}}. \tag{2.34}$$

The mean free path for ballistic transport of the charge carriers is found by

$$l_\mathrm{m} = \frac{h\mu}{2e}\sqrt{\frac{n}{\pi}}. \tag{2.35}$$

This quantity can be limited by scattering from many sources, including intrinsic ripples in the graphene sheet [69, 73], defects such as vacancies and grain boundaries [123, 147, 114, 14], and charged impurities [1]. It has been shown that even if charged impurities are screened with a high-κ dielectric, other scattering types can still hinder mobility and the mean free path [42].

The ballistic mean free path is related to the transport scattering time, τ_{m}, through the Fermi velocity by

$$l_{\mathrm{m}} = v_{\mathrm{F}}\tau_{\mathrm{m}}. \tag{2.36}$$

τ_{m} is related to the DC conductivity and is defined by the solution of the Boltzmann equation in the relaxation time approximation, and is written as

$$\tau_{\mathrm{m}} = \frac{\mu E_{\mathrm{F}}}{e v_{\mathrm{F}}^2}. \tag{2.37}$$

The values of ρ_{xx} and ρ_{xy} can also be used to find the longitudinal (σ_{xx}) and Hall (σ_{xy}) conductivities by inverting the resistivity matrix [121, 32] to find

$$\sigma_{xx} = \frac{\rho_{xx}}{\rho_{xy}^2 + \rho_{xx}^2} \tag{2.38}$$

and

$$\sigma_{xy} = \frac{\rho_{xy}}{\rho_{xy}^2 + \rho_{xx}^2}. \tag{2.39}$$

In 2D systems such as a two-dimensional electron gas (2DEG) or graphene, a perpendicular magnetic field will create discrete quantum mechanical orbitals known as Landau levels. However, while a typical 2DEG has a quantum Hall plateau at $\rho_{xy} = 0$ this is not possible in graphene due to the presence of a Landau level at $N = 0$. As a result, plateaus appear at

$$\sigma_{xy} = \pm\nu\frac{e^2}{h} \tag{2.40}$$

and

$$\rho_{xy} = \pm\frac{h}{\nu e^2} \tag{2.41}$$

where positive (negative) values correspond to electrons (holes), $\nu = 4\left(N + \frac{1}{2}\right)$ is the filling factor, and N is the Landau level index ($N = 0, 1, 2, ...$). These Hall plateaus appear at the same time that ρ_{xx} vanishes. This phenomenon is known as the half-integer quantum Hall effect [121, 175, 48] because of the different possible

values for the filling factor when compared to 2DEG systems. Fig. 2-3(b) shows a measurement of this effect with observed filling factors labeled.

The Fermi velocity for a graphene system can be found using the slope of the n vs. V_g curve and is written as

$$v_F = \frac{\sqrt{g_s g_v/\pi}}{\hbar D_0}\sqrt{n} = \frac{2}{\hbar D_0}\sqrt{\frac{n}{\pi}}. \tag{2.42}$$

Also, the effective mass of the charge carriers can be calculated from the charge carrier density by the equation [156]

$$m^* = \frac{k_F}{v_F} = \frac{\hbar}{v_F}\sqrt{\pi n}. \tag{2.43}$$

2.2.2 Shubnikov-de Haas effect

While the Quantum Hall effect describes the plateaus that appear in the Hall resistance (ρ_{xy}), the minima in the longitudinal resistance (ρ_{xx}) are explained by the Shubnikov-de Haas (SdH) effect.

The applied magnetic field causes the free charge carriers in the graphene to move in circular paths with energy eigenvalues described by the Landau levels with the cyclotron frequency ω_c (Eq. 2.18). Charge carriers away from the edges that are able to complete their circular paths do not contribute to the current. Charge carriers close enough to the edge to be scattered by it continue in the initial direction of propagation due to the Lorentz force. As a result, only the charge carriers at the edges contribute to the current, moving in what are known as edge channels. The number of edge channels is equal to the number of Landau levels below the Fermi energy [142].

Shubnikov-de Haas oscillations (SdHO) are only observable when the thermal broadening of the Fermi level is less than the spacing between Landau levels ($k_B T \ll \hbar\omega_c$). When this condition is met, sweeping the magnetic field produces oscillations in R_{xx} with minima that occur periodically in $1/B$. This oscillation frequency characterizes

the Fermi surface, allowing direct examination of the charge carrier density by using the relation

$$\Delta\left(\frac{1}{B}\right) = \frac{g_\mathrm{s} g_\mathrm{v} e}{nh} = \frac{4e}{nh}. \tag{2.44}$$

2.2.3 Two carrier transport

In physical graphene systems, both electrons and holes exist at and around the Dirac point for several reasons, including charge impurities, temperature broadening of energy levels leading to thermal fluctuations in the electron and hole densities, and ripples in the graphene which cause broadening of the Dirac point [99]. It is useful here to define the charge neutral point (CNP) of a graphene sample as the necessary voltage that must be applied to a gate to achieve equal concentrations of electrons and holes. The CNP can also be described as the point that the charge carrier density is minimized and the mobility is maximized. The smooth transition of the Hall resistivity ρ_{xy} through $V_\mathrm{g} = V_\mathrm{CNP}$[1] can be explained by a finite concentration of both electrons and holes at and around the CNP, with n_n and n_p the electron and hole concentrations, respectively [165, 56].

The analysis presented here is valid when there is no magnetic field induced splitting of the lowest Landau levels. This is represented by the expression $\mu_\mathrm{q} B \ll 1$, where μ_q is the quantum mobility, defined by the inverse magnetic field at which the aforementioned Landau level splitting occurs (when $\mu_\mathrm{q} B = 1$). When this is the case, we can use the two carrier model of conduction as derived by Hilke *et al.* [56], where

$$\begin{aligned} \rho^\eta_{xx} &= \frac{1}{\sigma_\eta}, \\ \rho^\eta_{xy} &= sgn\left(q_\eta\right)\frac{B}{\eta}, \\ \rho_\mathrm{tot} &= \frac{1}{\hat{\sigma}_\mathrm{n} + \hat{\sigma}_\mathrm{p}}, \end{aligned} \tag{2.45}$$

$\eta = n_\mathrm{n}$ or n_p for the densities of electrons and holes, respectively, and $\hat{\sigma}_\eta$ are single

[1]Some texts refer to V_CNP as V_Dirac.

band conductivity matrices. The longitudinal resistivity then becomes

$$\rho_{xx}^{\mathrm{tot}} = \frac{\left(n_{\mathrm{n}}n_{\mathrm{p}}\right)^{2}\left(\sigma_{\mathrm{n}}+\sigma_{\mathrm{p}}\right)+B^{2}\sigma_{\mathrm{n}}\sigma_{\mathrm{p}}\left(n_{\mathrm{n}}^{2}\sigma_{\mathrm{p}}+n_{\mathrm{p}}^{2}\sigma_{\mathrm{n}}\right)}{\left(n_{\mathrm{n}}n_{\mathrm{p}}\right)^{2}\left(\sigma_{\mathrm{n}}+\sigma_{\mathrm{p}}\right)^{2}+B^{2}\left(\sigma_{\mathrm{n}}\sigma_{\mathrm{p}}\right)^{2}\left(n_{\mathrm{n}}-n_{\mathrm{p}}\right)^{2}}. \tag{2.46}$$

The relative field dependence is then represented by

$$\frac{\Delta\rho_{xx}}{\rho_{xx}} = \frac{\rho_{xx}\left(B\right)-\rho_{xx}\left(0\right)}{\rho_{xx}\left(0\right)} = \frac{\left(B/B_{0}\right)^{2}}{1+\left(B/B_{1}\right)^{2}} \tag{2.47}$$

with

$$\begin{aligned} B_{0} &= \frac{en_{\mathrm{n}}n_{\mathrm{p}}\left(\sigma_{\mathrm{n}}+\sigma_{\mathrm{p}}\right)}{\sqrt{\sigma_{\mathrm{n}}\sigma_{\mathrm{p}}}\left(n_{\mathrm{p}}\sigma_{\mathrm{n}}+n_{\mathrm{n}}\sigma_{\mathrm{p}}\right)} = \frac{\rho_{\mathrm{max}}}{\rho_{xx}\sqrt{\mu_{\mathrm{n}}\mu_{\mathrm{p}}}} \cong \frac{en_{0}\rho_{\mathrm{max}}^{2}}{\rho_{xx}} \\ B_{1} &= \frac{en_{\mathrm{n}}n_{\mathrm{p}}\left(\sigma_{\mathrm{n}}+\sigma_{\mathrm{p}}\right)}{\left|n_{\mathrm{n}}-n_{\mathrm{p}}\right|\sigma_{\mathrm{n}}\sigma_{\mathrm{p}}} \cong \frac{n_{0}B_{0}}{\left|n_{\mathrm{n}}-n_{\mathrm{p}}\right|} \end{aligned} \tag{2.48}$$

where μ_{n} and μ_{p} are the mobilities of electrons and holes, n_0 is the residual carrier density measured at the CNP, and ρ_{max} is the zero-field longitudinal resistivity at the CNP. From this expression the parabolic dependence of resistivity on the magnetic field B is made clear.

2.2.4 Weak localization

Weak localization (WL) is a quantum-mechanical effect that occurs due to disorder in an electronic system and gives rise to a macroscopically observable increase in resistivity. The total quantum probabilities of the paths of each charge carrier around are described by not only the individual probabilities of each diffusive path but quantum interference terms as well; these interference terms lead to self-intersecting paths in both clockwise and counterclockwise directions around scattering centers. Since the loop in each direction is identical in length, the quantum phases exactly cancel out, leading to a non-zero probability for the charge carriers to move in circles. Applying a magnetic field perpendicular to the charge transport breaks time-reversal

symmetry which leads to a sharp drop in the resistivity, effectively suppressing weak localization.

In contrast, weak anti-localization results in a reduced resistivity but only appears with spin-orbit interactions that cause the spins of the charge carriers to rotate as they move along self-intersecting paths. The direction of spin rotation depends on the direction of the path so that clockwise and counterclockwise paths interfere destructively.

Magnetoresistance measurements can reveal many details about the structure of the electronic system being measured. Analyzing the zero-field resistance peak that occurs in all graphene systems studied in this work reveals information about electronic disorder and charge scattering characteristics of the system. The model applied in this work was proposed by Hilke *et al.* [56] and takes into account two carrier transport in addition to localization effects. Previous theoretical work by McCann *et al.* [98] also models the contributions of weak localization and weak anti-localization to the magnetoresistance, the latter of which can appear in graphene systems with low carrier densities combined with high temperatures [155].

The expression proposed by Hilke *et al.* includes five parameters and only one independent variable, B, and is written as

$$\left.\frac{\Delta R_{xx}}{R_{xx}}\right|_{\mathrm{tot}} \cong \frac{L_\phi}{L_\mathrm{c}} \frac{F\left(B/B_\mathrm{e} + B_{\mathrm{c}\phi}\right) - F\left(B/B_{\mathrm{c}\phi}\right)}{\ln\left(1 + B_\mathrm{e}/B_{\mathrm{c}\phi}\right)} + \frac{\left(B/B_0\right)^2}{1 + \left(B/B_1\right)^2} \tag{2.49}$$

where $F(z) = \psi(1/2 + 1/z) + \ln(z)$, $\psi(z)$ is the digamma function, and $\Delta R_{xx} = R_{xx}(B) - R_{xx}(0)$ with small variations. The relevant length scales are the sample length L, the spin coherence length L_ϕ, the elastic scattering length L_e, and the Anderson localization length L_c, with which we can present the final assumption of $L_\phi < L_\mathrm{c} \ll L$. The first term in Eq. 2.49 considers localization effects and describes the zero-field peak. The parabolic contribution of the second term is evaluated with the Drude model using two charge carrier types due to the presence of charge puddles, which as noted above, is valid when $\mu_\mathrm{q} B \ll 1$.

Elastic scattering in graphene can be categorized into two main categories, intravalley scattering and intervalley scattering, represented by their characteristic times τ_{a} and τ_{e}, respectively. Intravalley scattering is usually a very strong effect and is due to long-range potentials caused by large-scale inhomogeneities, the most typical example being the charged impurities in the substrate. These long range potentials induce regions of varied potential in the graphene known as charge puddles which contain both electrons and holes [60]. Intravalley scattering due to charge puddles does not result in coherent backscattering and thus does not contribute to weak localization.

Only intervalley scattering causes coherent backscattering and leads to weak localization. Intervalley scattering from $\boldsymbol{K}$ to $\boldsymbol{K'}$ is usually induced by atomically sharp defects such as the edges of the sample or grain boundaries. While charged impurities on the graphene can also cause coherent backscattering, their long-range Coulomb potentials can also contribute to weak anti-localization.

Strong localization, also known as Anderson localization, is a related effect that emerges when the disorder is high enough such that localized states appear. Localized states are eigenstates that decay exponentially away from a center and occur when the mean free path becomes comparable to the wavelength.

Finally, the aforementioned characteristic lengths and other quantities can be determined with the relations

$$L_{\mathrm{c}}^{-2} + L_{\phi}^{-2} = \frac{4eB_{\mathrm{c}\phi}}{\hbar}, \tag{2.50}$$

$$L_{\mathrm{e}}^{-2} = \frac{4eB_{\mathrm{e}}}{\hbar}, \tag{2.51}$$

$$B_0 \cong \frac{\rho_{\mathrm{max}}}{\mu\rho_{xx}}, \tag{2.52}$$

and

$$B_1 \cong B_0\left|\frac{n_0}{n}\right| \tag{2.53}$$

where ρ_{max} is the resistance at $V_{\mathrm{g}} = V_{\mathrm{CNP}}$ and zero magnetic field, n_0 is the residual

charge carrier density defined by the carriers from the charge puddles plus any thermal carriers, and n is the total charge carrier density found with Hall measurements.

2.3 Electron spin resonance (ESR)

Electron spin resonance (ESR) is a measurement technique for studying materials with unpaired electrons [145]. In an ESR experiment, two magnetic fields are required. The first field is static and causes spin splitting of electronic energy levels. The magnetic moments of the electrons precess around this field in a phenomenon known as Larmor precession. A second weaker and alternating field is then applied perpendicularly to the first and can cause the electron to be "tipped" to the other orientation when the frequency of the second field is equal to the Larmor frequency.

When electrons are exposed to an external magnetic field, they align themselves either parallel or antiparallel with the field according to their spin magnetic quantum number, $m_{\mathrm{s}} = \pm\frac{1}{2}$. The potential energy of a magnetic dipole moment in a magnetic field is

$$E = -\boldsymbol{\mu} \cdot \boldsymbol{B} \tag{2.54}$$

and the energy levels due to Zeeman splitting are

$$E = \pm\frac{1}{2} g \mu_{\mathrm{B}} B \tag{2.55}$$

where $\mu_{\mathrm{B}} = \frac{e\hbar}{2m_{\mathrm{e}}}$ is the Bohr magneton and g is the g-factor. An unpaired electron can jump between these two energy levels by either absorbing or emitting a photon with an energy that matches the level separation. This change of energy is written as

$$\Delta E = hf = g\mu_{\mathrm{B}} B \tag{2.56}$$

where f is the photon frequency. When the system is in thermal equilibrium, as modeled by the Maxwell-Boltzmann distribution, there are typically more electrons in

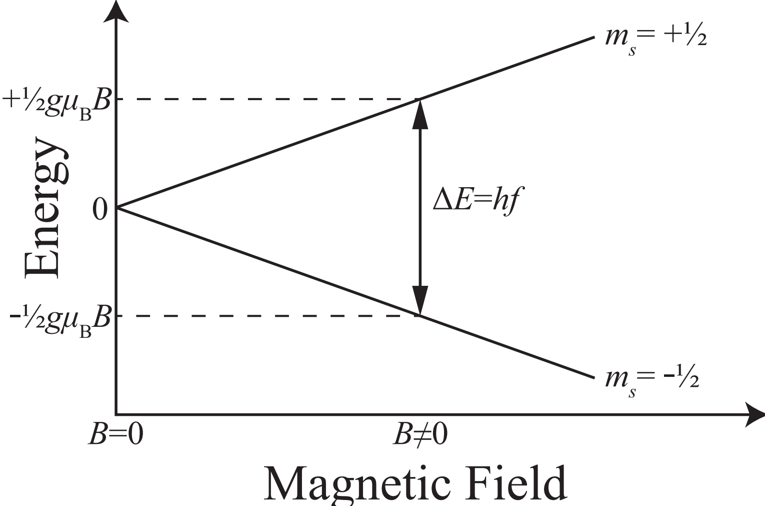

Figure 2-4: Diagram outlining Zeeman splitting of an electron in a static magnetic field. At resonance, an electron will jump the energy gap by either emitting or absorbing a photon of the correct frequency.

the lower energy state, meaning the transition from the lower to the higher level more probable than the opposite case and that the weak magnetic field of the RF signal causes a net absorption of energy in the sample.

The g-factor of the charge carriers in a material can be determined with ESR measurements by finding multiple resonance conditions and using the relation

$$g = \frac{\mu}{\mu_\mathrm{B}} \tag{2.57}$$

where μ is the magnetic moment which is found by

$$\mu = h\frac{\mathrm{d}f}{\mathrm{d}B}. \tag{2.58}$$

The spin relaxation time τ_s, which is the average time before dephasing, is found with the equation

$$\tau_\mathrm{s} = \frac{\hbar}{2\Delta E}, \tag{2.59}$$

with

$$\Delta E = \mu \Delta B, \tag{2.60}$$

where ΔB is the half-width of the resonance peak in a measurement of longitudinal resistance versus applied magnetic field.

Finally, we can use τ_{s} with the diffusion constant D, which is defined as

$$D = \frac{1}{2} v_{\mathrm{F}} l_{\mathrm{m}} \tag{2.61}$$

to calculate the spin diffusion length λ_{s}, which we write as

$$\lambda_{\mathrm{s}} = \sqrt{D\tau_{\mathrm{s}}}. \tag{2.62}$$

2.4 Spin relaxation mechanisms

As stated earlier, graphene is a material of great interest due to its predicted long spin relaxation times on the order of 1 μs, though experimentally realized values have fallen short of any theoretical prediction by a few orders of magnitude. To understand why this is the case will require analysis of the different mechanisms of spin relaxation. The Elliot-Yafet (EY) and D'Yakanov-Perel (DP) mechanisms are the two main mechanisms for describing spin relaxation in metals and semiconductors [12]. Both involve spin-orbit coupling (SOC), with the EY mechanism dependent on intrinsic SOC and the DP mechanism arising from other sources [126].

In an EY-like mechanism, momentum scattering events lead to random changes in momentum directions and also changes spin direction. However, in a DP-like mechanism, an effective magnetic field arises, which causes spin precession. Put another way, an EY-like mechanism has the spin relaxation rate proportional to the momentum scattering rate, while for a DP-like mechanism the spin relaxation rate is inversely proportional to the momentum scattering rate.

There has been much debate which spin-relaxation mechanism is dominant in graphene though it is likely that both mechanisms play a role [176]. For graphene on SiO_2, however, a DP-like mechanism seems to be dominant [161].

2.5 Charged impurity concentration

As described by Chen *et al.* [23], mobility in graphene can be limited by many things, including phonons, corrugations, mid-gap states, and impurity scattering. The largest limiting factor to the quality of mobility of graphene on a substrate such as SiO_2, however, is scattering due to charged impurities [1].

Charged impurities create different potentials all over the graphene, which at low carrier densities divides the system into puddles of electrons and holes that screen external electric potential. The chemical potential is spatially changed all over the graphene sheet, which induces a residual density that exists even when the gate is tuned to the Dirac point, which minimizes conductivity. The experimentally determined value for minimum conductivity is most commonly quoted to be $\sigma_0 = 4e^2/h$, though this value is not universally observed [1, 116].

The total charge carrier density can be approximated by

$$n = |n_{\mathrm{G}}| + |n^*|, \tag{2.63}$$

where n_{G} is the gate-induced charge carrier density, and n^* is the induced residual charged impurity density due to charged impurities which can be extracted by measuring the total charge carrier density at the charge neutral point [167]. According to a self-consistent procedure described by Adam *et al.* [1], once n^* is known, it is possible to deduce the charged impurity concentration, n_{imp}. This self-consistent theory uses a

random phase approximation (RPA)-Boltzmann formalism and is represented by

$$n_{\mathrm{imp}} = \frac{n^*}{\left[2r_{\mathrm{s}}^2 C_0^{\mathrm{RPA}}\left(r_{\mathrm{s}}, a = 4d\sqrt{\pi n^*}\right)\right]} \tag{2.64}$$

where r_{s} and n^* are previously discussed quantities and d is the average distance of charged impurities from the graphene, typically taken to be $d \approx 1\,\mathrm{nm}$. This formalism uses Boltzmann kinetic theory with the assumptions that $T \ll T_{\mathrm{F}}$ (where $T_{\mathrm{F}} = E_{\mathrm{F}}/k_{\mathrm{B}}$), $n^*/n_{\mathrm{imp}} \gg 0.01$, and that we are in the diffusive transport regime. The last assumption is reasonable considering our devices are many microns in length while the mean free path is only tens of nanometers. The RPA correlation function is written as

$$\begin{aligned} C_0^{\mathrm{RPA}}\left(r_{\mathrm{s}}, a\right) = &-1 + \frac{4E_1\left(a\right)}{\left(2 + \pi r_{\mathrm{s}}\right)^2} + \frac{2\mathrm{e}^{-a} r_{\mathrm{s}}}{1 + 2r_{\mathrm{s}}} \\ &+ \left(1 + 2r_{\mathrm{s}} a\right) \mathrm{e}^{2r_{\mathrm{s}} a}\left(E_1\left[2r_{\mathrm{s}} a\right] - E_1\left[a\left(1 + 2r_{\mathrm{s}}\right)\right]\right) \end{aligned} \tag{2.65}$$

where $E_1\left(z\right) = \int_z^\infty t^{-1}\mathrm{e}^{-t}\,\mathrm{d}t$.

2.6 Defects

There are many types of defects that modify the honeycomb lattice structure of graphene and change its properties [87]. The simplest is the Stone-Wales defect which rotates one C-C bond to transform four hexagons into two pentagons and two heptagons. Many other defect types are common as well, including vacancies of one or more carbon atoms, substitutional atoms, adatoms at various sites on the graphene sheet, grain boundaries between two different domains of lattice orientations, and edge defects.

Defects may appear during growth or sample processing steps, though they may also be deliberately added by irradiation or chemical treatments in order to tune the graphene to have specific properties. Further discussion of graphene defects in this work will be limited to the analysis of the quality of the fabricated samples as well as

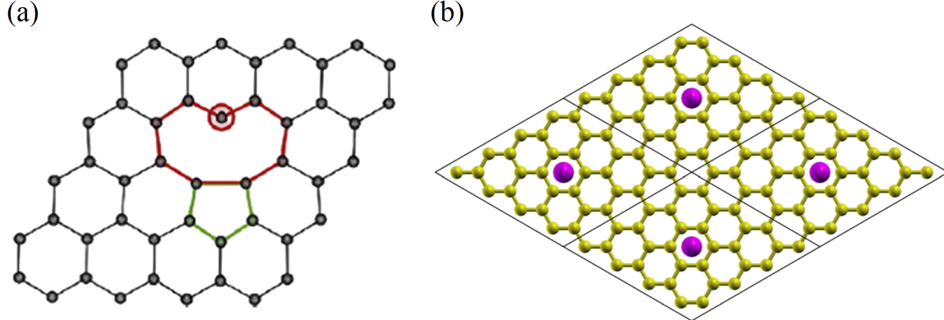

Figure 2-5: (a) The atomic structure of graphene with a specific type of single vacancy (adapted with permission from Liu *et al.* [87], copyrighted by Elsevier). (b) Graphene with adatoms in hollow sites at the center of carbon hexagon rings (adapted with permission from Chan et al. [20], copyrighted by the American Physical Society).

any influence they may have on the measurement results.

2.7 Raman spectroscopy

Raman spectroscopy is a technique that probes molecular vibrations and can be used for sample identification and analysis [143]. It is used in this work to validate that the graphene samples are indeed monolayer as well as investigate defect density and general quality. This technique is performed by shining a monochromatic light source on a sample and detecting the scattered light and is a form of vibrational spectroscopy, much like infrared (IR) spectroscopy. Raman bands arise from a change in polarizability due to scattered light while IR bands occur due to changes in the dipole moment of the sample molecule from absorbed or transmitted light. Depending on the molecular symmetries of a sample, different vibrational modes may be accessible with one, both, or neither techniques.

In a Raman measurement, impinging photons excite the sample to an electronic excited state that couples together initial and final vibrational states. Most of the detected light is Rayleigh scattered, meaning that it is elastically scattered: the initial and final vibrational states are the same, and the impinging and scattered light has

the same energy. However, a small fraction of impinging photons, on the order of 1 in 10^7, are instead inelastically scattered with the energy difference being equal to the shift in energy between the vibrational modes. When this energy difference is negative, meaning that the scattered photon has lost energy and the sample has been excited to a higher vibrational state, it is known as a Stokes shift; an anti-Stokes shift is the opposite case such that the scattered photon has higher energy than the impinging photon and the final vibrational state is lower energy than the initial state. At room temperature, however, the thermal population of vibrationally excited states is generally low, leading to a weaker anti-Stokes-shifted Raman spectrum than a Stokes-shifted spectrum.

In graphene, the G peak (~1,580 cm^{-1}) is a primary in-plane vibrational mode and the 2D peak (~2,700 cm^{-1}, also known as the G′ peak) is a second-order two-phonon process and is an overtone (transition of greater than one vibrational level) of the D peak. No defects are required for the 2D peak due to it originating from a process in which phonons with opposite wavevectors satisfy momentum conservation; this is not the case for the D peak (~1,350 cm^{-1}), which is due to breathing modes of the six-atom Carbon rings in the graphene lattice and is strictly forbidden unless disorder is present. Grain boundaries produce a pronounced D peak [173], which is of particular interest to CVD graphene due to its growth typically resulting of many domains.

The 2D and G peaks shift location due to changes in charge carrier concentration and the ratio of their intensities can be used to find carrier concentration and monitor the level of electron or hole doping [19, 26]. Observation of the shape, intensity, and location of each of these peaks also allows for quick identification of the number of layers [38, 15, 16]. Both the 2D and G peaks are also sensitive to strain [118, 102, 25] and the G peak changes shape depending on the edge configuration [141, 140]. The D and 2D modes are dispersive, meaning their location depends on the excitation wavelength [39].

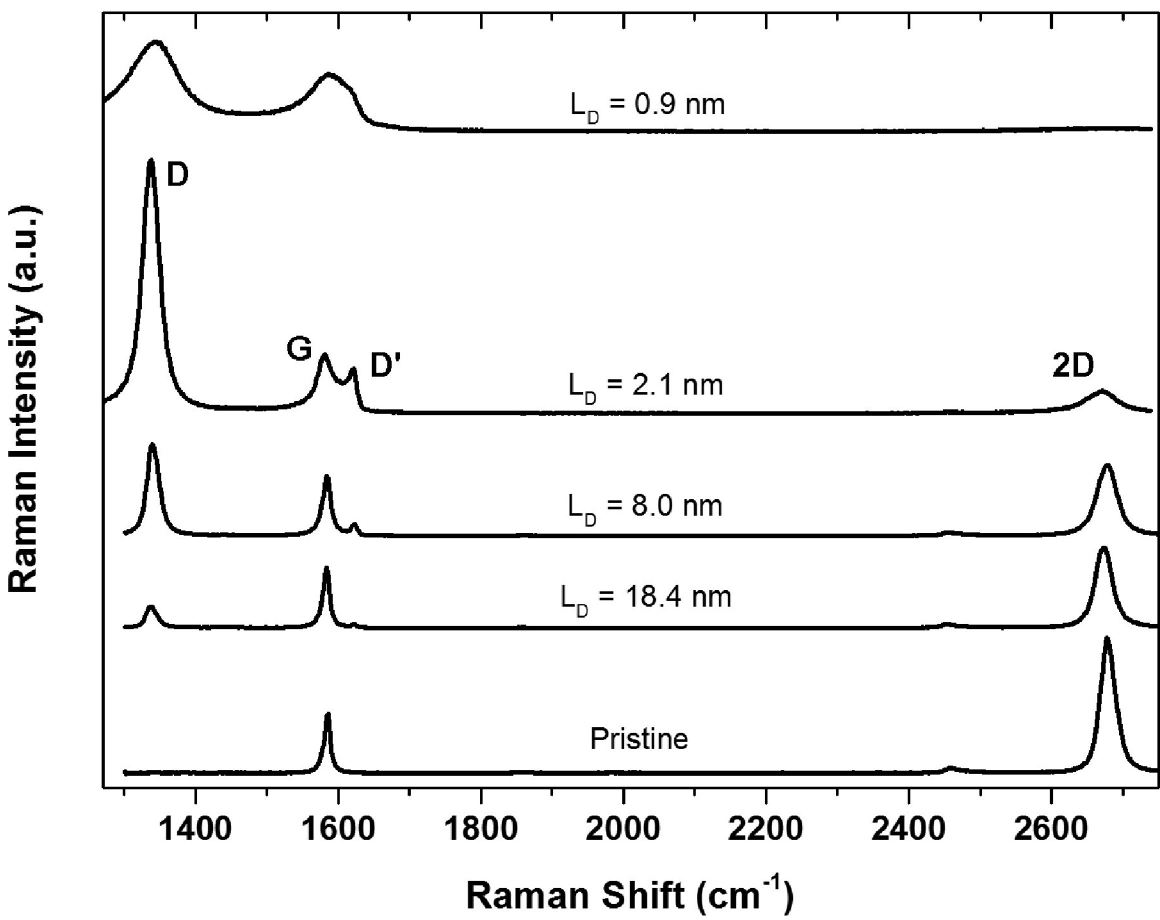

Figure 2-6: Raman spectra of graphene obtained with a 532 nm excitation laser for increasing defect densities produced by Mn ion-bombardment. L_{D} is the distance between defects, n is the defect density, and the G^* peak located at ~2,460 cm^{-1} is not labeled. Spectra are vertically offset for illustrative purposes. (Adapted with permission from Pollard *et al.* [132], copyrighted by AIP Publishing LLC.)

The small bump to the left of the 2D peak is known as the G^* peak (~2,460 cm^{-1}) and arises from a combination of one transverse optical (TO) phonon and one longitudinal acoustic (LA) phonon. This peak is also slightly dispersive and shifts to lower wavelengths with increasing number of graphene layers [144, 94]. The last peak of interest is the D' peak (~1,620 cm^{-1}), which splits off of the G peak and only appears as the system becomes more disordered.

A number of studies have researched the relationship between Raman peaks and the nature of graphene defects. A quantitative formula has been found by Cançado et al. [17] that relates the mean distance between defects, L_D, with the relative intensities of the G and D peaks in graphene, I_G and I_D.

$$L_D^2 \left(\mathrm{nm}^2\right) = (1.8 \pm 0.5) \times 10^{-9} \lambda_L^4 \frac{I_G}{I_D} \tag{2.66}$$

where λ_L is the Raman excitation wavelength in nm. This is related to the defect density n_D by the equation

$$n_D \left(\mathrm{cm}^{-2}\right) = \frac{10^{14}}{\pi L_D^2}. \tag{2.67}$$

These relations are valid for point defects such in the limit of large L_D though it should be noted that they are limited to describing Raman-active defects that generate a D peak. Perfect zigzag edges, charged impurities, and other defects must be detected by analyzing other Raman peaks.

2.8 Growth by chemical vapor deposition (CVD)

A process for creating graphene with chemical vapor deposition (CVD) is shown in Fig. 2-7. First, pyrolysis of a precursor material requires a high temperature, and graphene CVD growth is performed on a metal substrate such as copper in order to reduce the temperature of the reaction down to about 1,000 °C. A typical precursor is CH_4 and pyrolysis must be done at the surface in order to avoid the formation

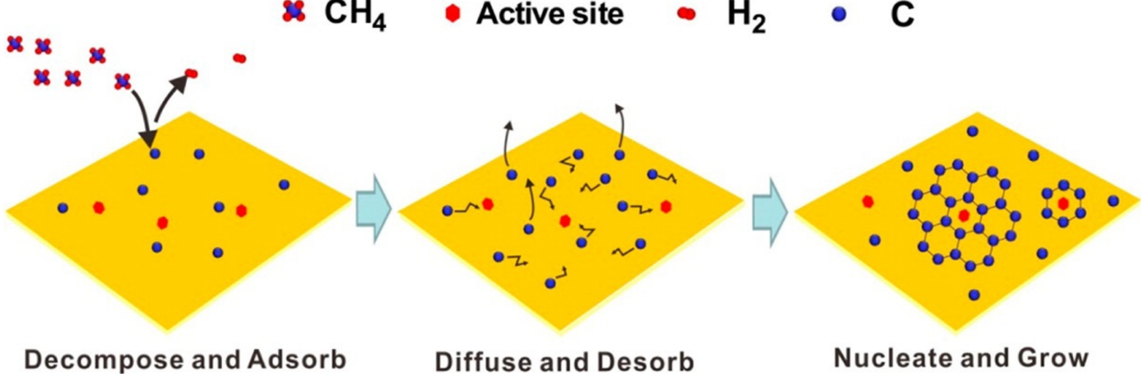

Figure 2-7: A graphene growth process on CVD. CH_4 is decomposed by pyrolysis and active carbon species adsorb, diffuse, and desorb from the surface until some of them attach to nucleation sites. Each nucleation site grows until the copper is coated in graphene. (Adapted with permission from Yan *et al.* [168]. Copyright 2012 American Chemical Society.)

of carbon clumps. Once the active carbon species are separated out they are free to be adsorbed by the copper surface. The carbon-copper reaction is weak and the active carbon species that adsorb on the surface diffuse and desorb, eventually agglomerating into thermodynamically stable species on active sites forming graphene nuclei. These nucleation sites are generally believed to be locations of impurities in the copper substrate [90]. Further active carbon species have a higher probability of being captured by existing nucleation sites than forming new ones [168].

This process is self-limiting due to the low solubility of carbon in copper making it relatively simple to ensure the growth of monolayers [85]. One of the most important factors for improving electrical characteristics of CVD graphene is minimizing the number of nucleation sites and thus the number of grain boundaries in the finished graphene layer. This involves careful optimization of the CVD process and copper substrate though these methods are beyond the scope of this work.

Chapter 3

Sample fabrication and preparation

This chapter describes all of the techniques used and steps performed to fabricate the graphene samples analyzed in this work. Each measured device has a Si/SiO_2 substrate, though samples with many other types of substrates could be produced without significant modifications to the procedures outlined in this chapter.

3.1 Graphene preparation

A sheet of copper is supplied by Graphenea with CVD-grown graphene on only one side. Other sources of CVD graphene on copper typically have graphene on both sides of the foil, and in that case, an oxygen plasma can be used to remove graphene from one side. A wet transfer process is used to place the graphene on the substrate, with cleaning steps to remove inorganic and organic contaminants from the bottom of the graphene before transfer. These steps are similar to the method detailed by Liang *et al.*, which itself includes a "modified RCA clean" process [86].

It is important to be sure that all contaminants from the graphene are removed, as any resist residues can act as dopants and scattering centers to degrade electrical performance [11, 31] as well as increase contact resistance [84, 80]. Acetone or other common solvents are not sufficient to remove residues from resists such as

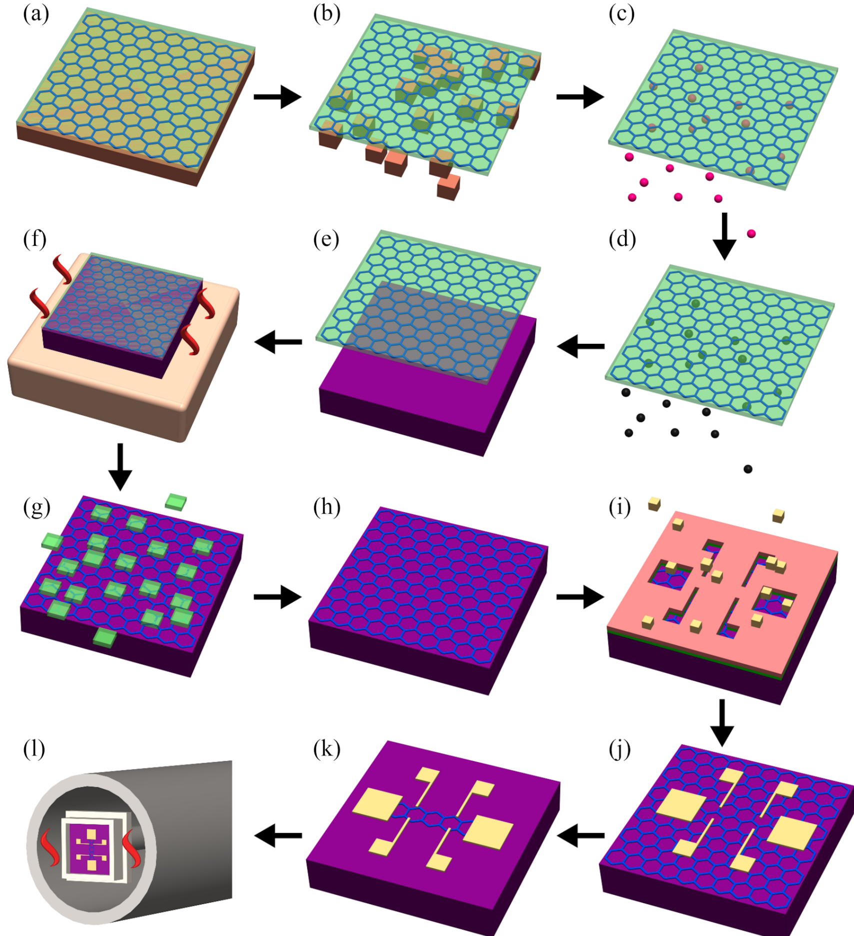

Figure 3-1: Flow diagram of the sample preparation. PMMA is spun onto the graphene-copper stack (a) before the copper is etched away (b). The graphene is cleaned in multiple steps removing inorganic (c) and organic (d) contaminants, scooped up with a SiO_2 wafer piece (e) and then dried (f). The PMMA layer is removed with acetic acid (g) and the result is shown in (h). For the definition of the Hall contacts, the sample is coated with layers of LOR and photoresist, exposed and developed, before Ni and Au are deposited as adhesion and contact materials, respectively (i). After lift-off (j), the excess graphene is etched away (k) and the sample is mounted in a probe and baked under vacuum (l).

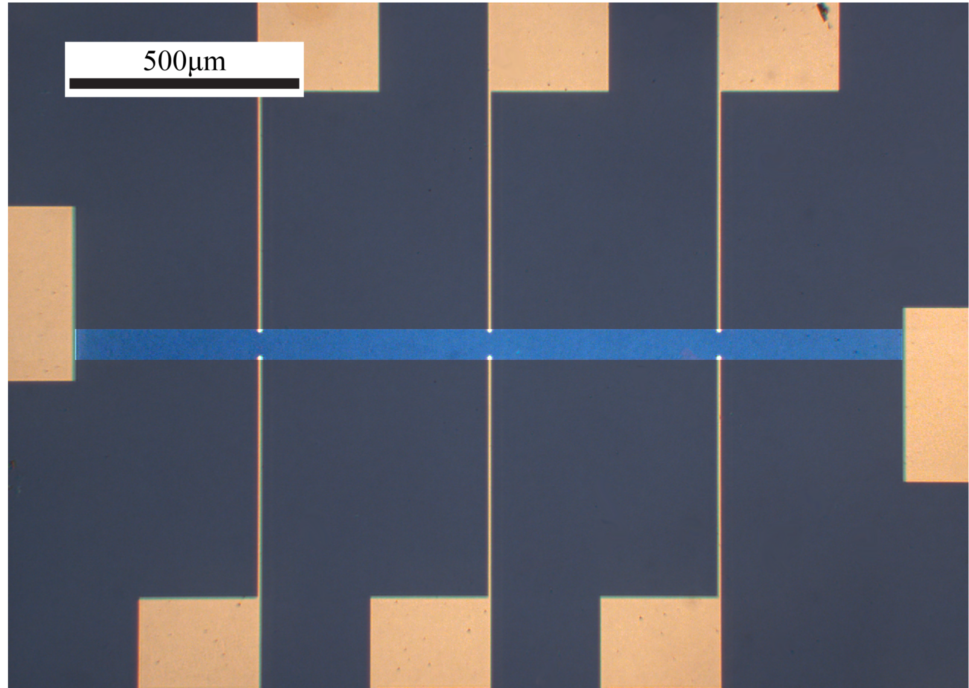

Figure 3-2: Photo of mm-scale graphene Hall bar, 1.92 mm long and 66 µm wide. Graphene contrast is increased for visual effect.

poly(methyl methacrylate) (PMMA). A common technique to clean small graphene devices is to use current annealing [104, 77], especially when the graphene is suspended, as it can effectively evaporate many contaminants and allow the graphene to self-heal [6]. Other cleaning methods include mechanical cleaning with atomic force microscopy [46], exposure to ultra-violet light [22], ozone treatment [22, 84], and annealing in vacuum [131] or with gas flow [62]. In the process detailed in this paper, the graphene is cleaned before transfer to a clean substrate and then cleaned again after fabrication by a 2-step thermal annealing process.

The size of the graphene/copper foil pieces used here is 1 cm $\times$ 1 cm, however, the process can easily be upscaled to sizes of several cm^2. PMMA with a molecular weight of 950K is spun onto the graphene/copper foil and dried by air (Fig. 3-1(a)). A solution of $Fe(NO_3)_3$ is prepared with 5 g/100 mL of deionized (DI) water and the PMMA/graphene/copper stack is placed to float in the solution with the copper side down, then left for at least 10 hours for the copper to etch away (Fig. 3-1(b)).

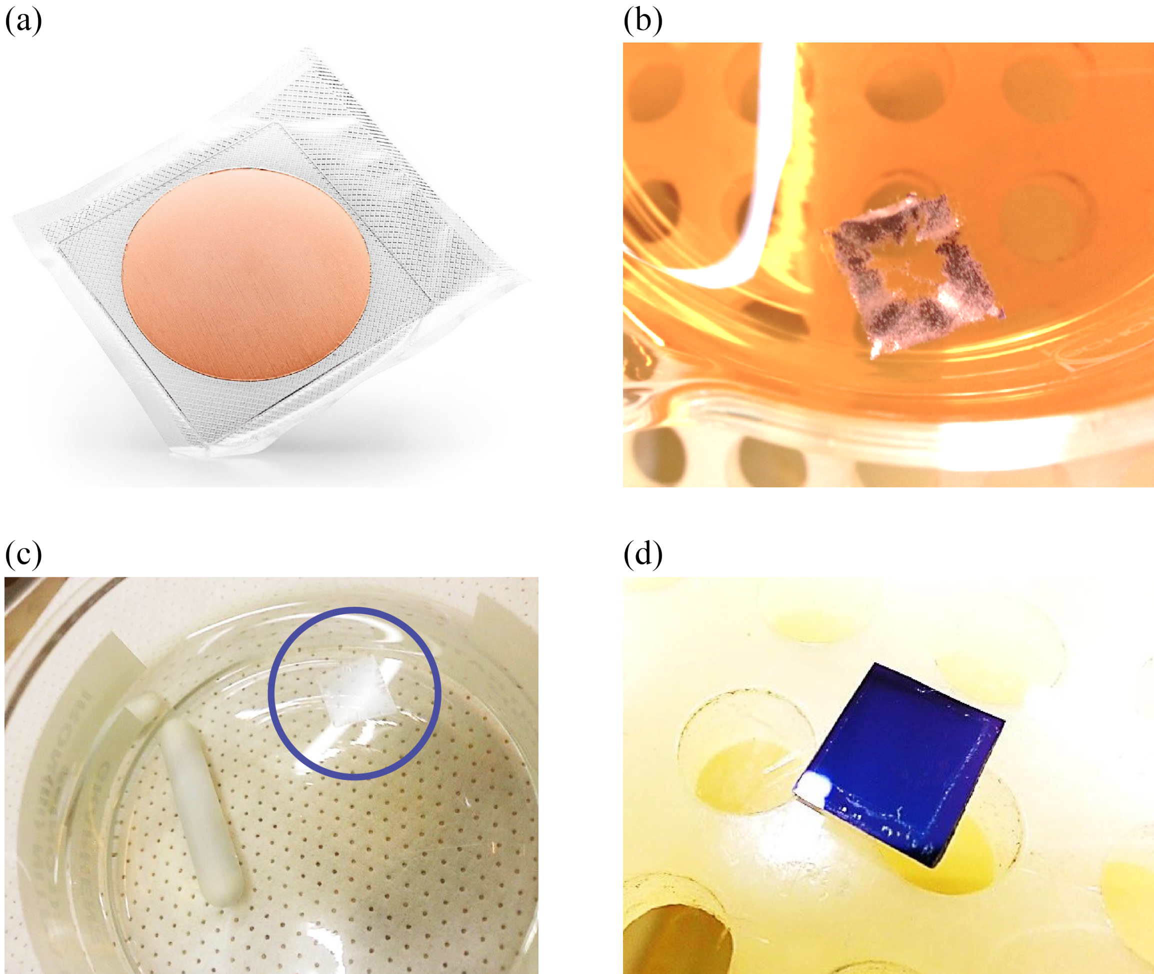

Figure 3-3: Photos of graphene at various stages during sample preparation. (a) Graphene on copper foil supplied by Graphenea. (b) Copper being etched away with iron(III) nitrate. (c) A PMMA/graphene stack floating on DI water circled in purple. By itself, a single layer of graphene only absorbs $\approx 2.3\%$ of light [109]. PMMA is also highly transparent, so it can still be difficult to see the combined stack on the surface of the water. (d) Graphene on SiO_2 after transfer, baking, and cleaning steps.

Subsequently, the graphene stack is transferred to clean DI water at least twice, waiting 5 minutes after each transfer. Similarly to Liang *et al.*, the RCA clean step referred to as Standard Clean 2 (SC-2) is next, with a $HCl/H_2O_2/H_2O$ solution prepared in a 1:1:20 ratio. The stack is placed on this solution to clean inorganic contaminants not removed by the $Fe(NO_3)_3$, such as oxides, for 15 minutes (Fig. 3-1(c)). The stack is then once again transferred to clean beakers of DI water at least twice for 5 minutes each. Finally, the RCA clean step known as Standard Clean 1 (SC-1) is performed with a $NH_4OH/H_2O_2/H_2O$ solution in a 1:1:100 ratio for 5 minutes (Fig. 3-1(d)) to remove organic contaminants. The cleaning time and chemical concentrations of H_2O_2 and NH_4OH in SC-1 are lower than reported in the modified RCA clean process in order to avoid bubble formation. Bubbles that get under the graphene stack can lead to the graphene tearing and are very difficult to remove before transfer. After the SC-1 step is complete, the graphene is again transferred to clean beakers of DI-water twice, waiting 5 minutes after each transfer.

At this point, the PMMA/graphene stack can remain floating on the surface of clean DI water until there is a suitable piece of substrate ready to scoop it up.

3.2 Substrate preparation

3.2.1 Wafer dicing

Si/SiO_2 wafers are cheap and readily available and are commonly used in the semiconductor industry for all kinds of devices due to their desirable electronic properties and the relatively low effort required to integrate into large-scale processes. The wafers used here are 500-550 µm thick Si(100) degenerately *p*-doped with boron to have a resistivity of ~0.005 Ω m, and a thermally grown and polished 300 nm thick top layer of SiO_2. The charge carrier density of a completed graphene device is controlled by capacitive coupling with the layer of degenerately doped silicon.

The wafers are cut into pieces greater than 1 cm^2 with a diamond scribe while

being held firmly on cleanroom tissue with the polished side down. It is not necessary to cut all the way through the wafer, only to scratch it deep enough so that when sufficient pressure is placed on each side of the scratch the wafer will break along the etched line. Contaminants are cleaned off by sonication in acetone and then isopropanol. Finally, the wafer pieces are dried with a nitrogen gun.

3.2.2 Substrate patterning

Periodic patterns on SiO_2 substrates were developed to examine the effects of mechanically modulated graphene. Electron beam lithography was used to define a pattern of trenches with an "FEI Quanta FEG 250" electron beam microscope and recipes described in Appendix A. Trenches were etched with reactive ion etching (RIE) using C_4F_8 gas in a "Sentech ICP-RIE Plasma Etcher SI 500." Alignment markers were sputtered onto the sample from an Au/Pd target after defining the marker area using photolithography.

When graphene is transferred onto a sample with trenches using the wet transfer process described in the next section, it is pulled down to conform to the surface as the water underneath evaporates, putting the graphene under strain. The graphene will tear if the height differential between the highest and lowest points is too great. The deepest etch depth found to not break our graphene using the process methods described here is 18 nm when using 100 nm trenches and 100 nm mesas. In general, broken graphene resulted when the etch depth was greater than about 15-20% of the width of the trenches or mesas. This can be seen in scans taken with a scanning electron microscope (SEM) of defective graphene devices in Fig. 3-7. SEM scans are generally only performed on defective samples as even low energy electron beams damage graphene.

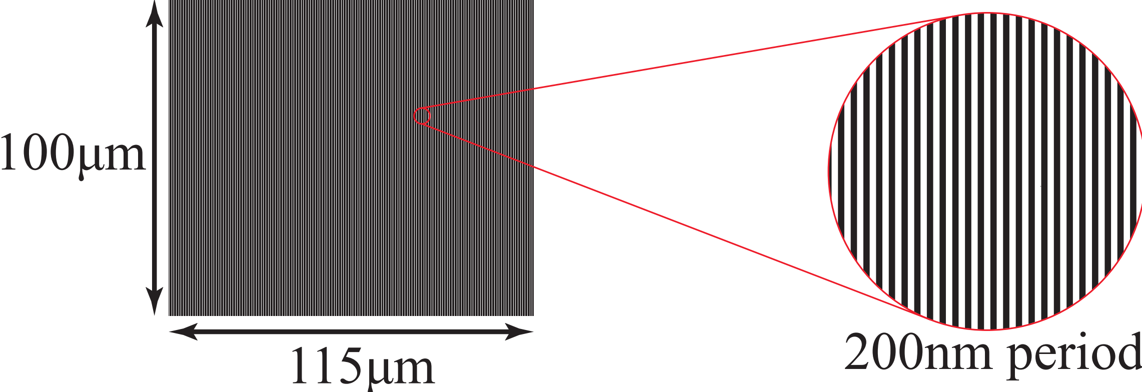

Figure 3-4: SEM pattern for etching 100 nm trenches and 100 nm mesas for a total 200 nm period. Alignment markers not shown.

3.3 Graphene transfer

The SiO_2 surface is treated with O_2 plasma in order to make the surface more hydrophilic [107] so that the graphene will stick to it more readily and minimize breakage. Within one minute of the substrate's O_2 plasma exposure, the PMMA/graphene stack is scooped up and dried in an oven set to 150 °C for 15 minutes (Fig. 3-1(e) and (f)).

Finally, the PMMA is removed with acetic acid (Fig. 3-1(g)), which is more effective than acetone and does not damage the graphene or the SiO_2 substrate [55]. At this point, the graphene is cleanly transferred to the substrate with minimal cracks or tears (Fig. 3-1(h)), with most defects existing previous to the transfer process. Many other defects can be explained by bumps, folds, or other surface features in the copper foil that the graphene was grown on. It is very important to keep the copper foil as flat as possible at all times in order to minimize graphene tearing during processing.

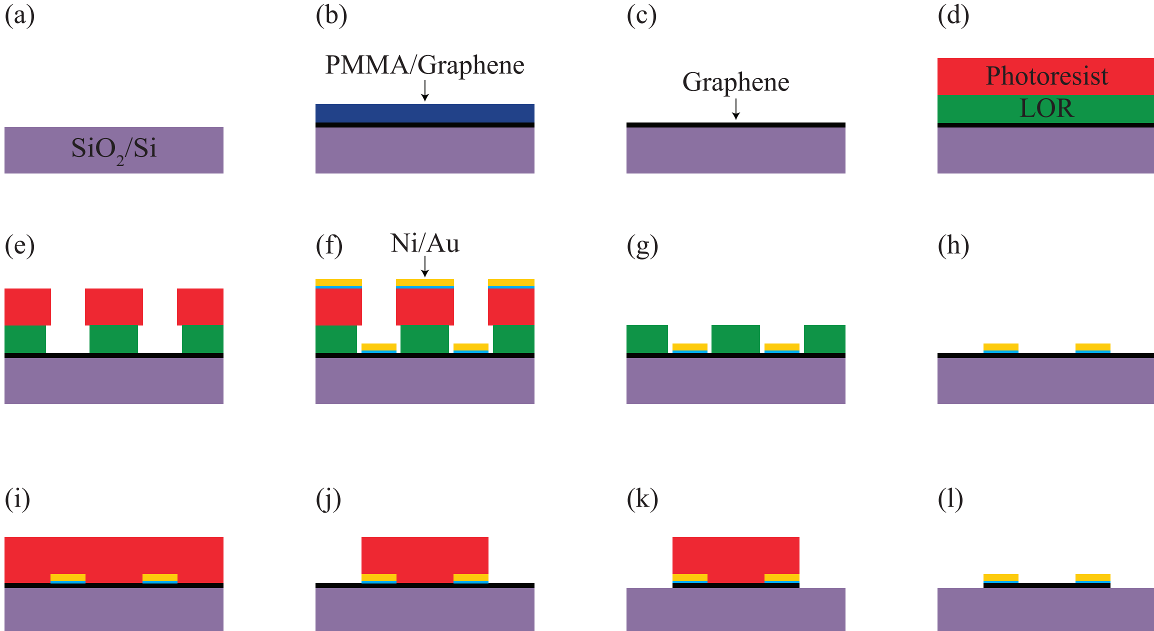

Figure 3-5: Step-by-step layered view of the workflow for transferring the graphene to the substrate, depositing the contacts, lift-off, and defining the graphene area. (a) Clean Si/SiO_2 substrate. (b) Transfer PMMA/graphene stack and dry. (c) Remove PMMA with acetic acid, rinse in isopropanol, then dry with a nitrogen gun. (d) Deposit LOR, bake, deposit photoresist, and bake again. (e) Expose and develop the contact pattern. (f) Deposit gold contacts with nickel adhesion layer. (g) Lift-off photoresist using gentle agitation with a pipette in a bath of acetone. (h) Remove LOR 5A with Microposit Remover 1165, rinse in isopropanol, then dry with a nitrogen gun. (i) Deposit photoresist and bake. (j) Expose and develop the area where graphene is not desired. (k) Use O_2 plasma to remove exposed graphene. (l) Remove photoresist with acetone, rinse in isopropanol, then dry with a nitrogen gun. The sample is now ready for bonding and mounting.

Figure 3-6: Photo displaying typical coverage of graphene transfer process on an etched test pattern. The pattern has 2 µm trenches separated by 2 µm mesas and is 1.8 mm long.

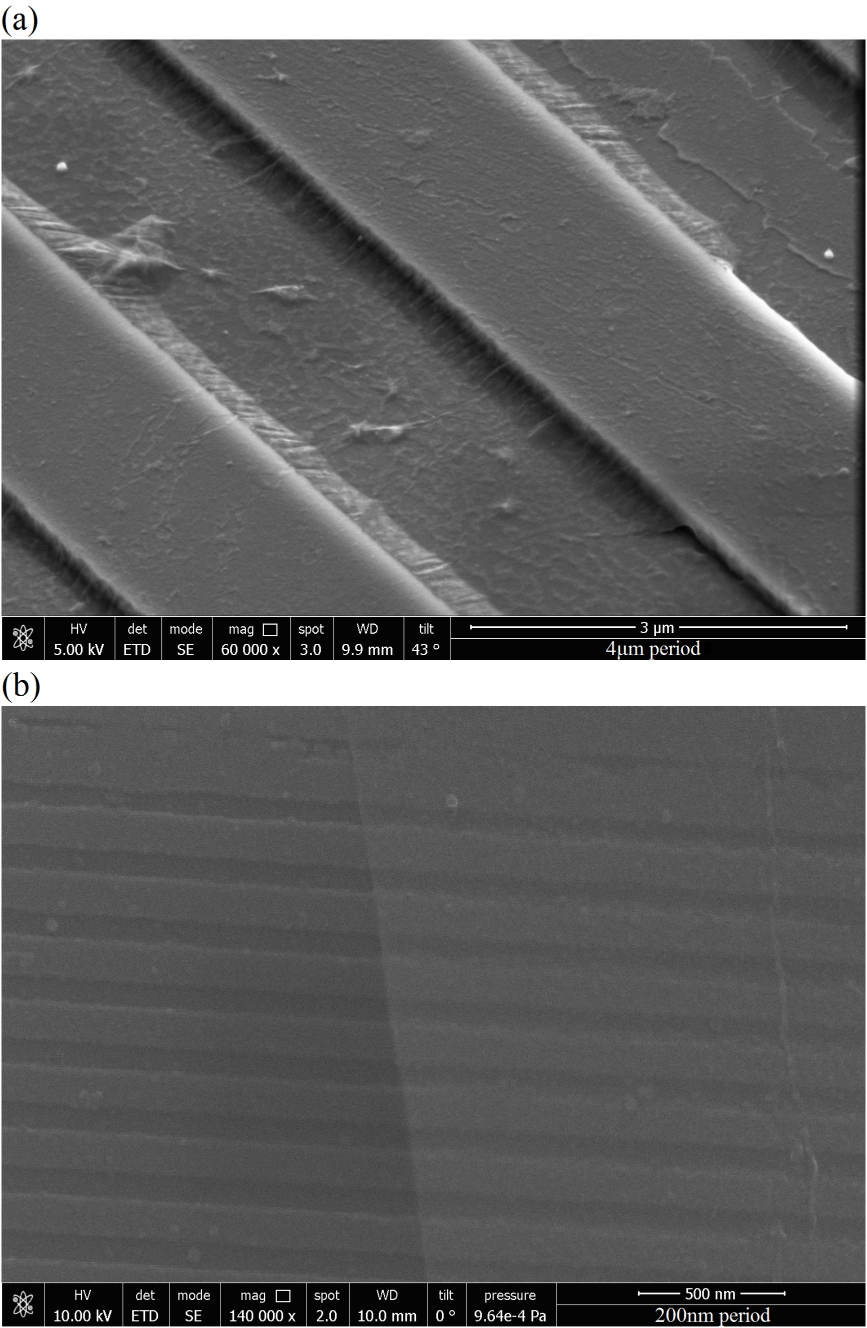

Figure 3-7: SEM scans of graphene on SiO_2 substrate with trenches. (a) 2 µm trenches alternating with 2 µm mesas resulting in a 4 µm period. The etch depth is 198 nm. The graphene attempts to conform to the surface resulting in suspended areas between the high and low areas. Note the tearing evident in the lower right. (b) ~200 nm period with ~100 nm trenches and mesas and 18 nm etch depth. Graphene is on the right side.

3.4 Metal contacts

At this stage, graphene is on the target substrate, but metal contacts must still be deposited. The graphene must also be patterned into whatever shape is desired. Both of these steps must ideally be done without damaging or contaminating the graphene any more than absolutely necessary. Optical lithography was used to define the contacts due to the length scales involved being greater than 2 µm. Positioning and exposure was performed with a commercially available Karl Suss MJB4 mask aligner.

A significant benefit of the graphene transfer process described earlier is that there is no need to carefully hunt for the ideal spot to place your device. The large area of unbroken, high-quality graphene allows us to make masks designed for producing many devices at once. For example, this work uses a mask with a 5x5 grid of contacts for Hall bars in an area of ~1cm^2. The end contacts are 200 µm apart, the longitudinal contacts are separated by 100 µm, and each pair of Hall contacts is separated by 16 µm. Bonding pads were made to be a minimum of 300 µm in both length and width in order to facilitate bonding by hand.

Much trial-and-error went into finding an effective recipe for depositing contacts on a large Hall bar. The single largest issue was the unintentional removal of graphene during lift-off. Performing optical photolithography with a typical resist such as Microchem S1805 gave varying results, with some graphene being removed during lift-off in an uncontrollable fashion. There appeared to be a time-dependent factor, with more graphene being removed the longer it took to complete the processes for metal deposition and lift-off. Multiple trials with a variety of resists were used with no notable improvement. Negative photoresists resulted in the worst cases with near-total removal of graphene after lift-off, possibly due to crosslinking of polymer chains during exposure.

Microchem LOR 5A is a resist normally used to aid in lift-off by ensuring that there is an undercut even when used with positive resists. In order to add it to the

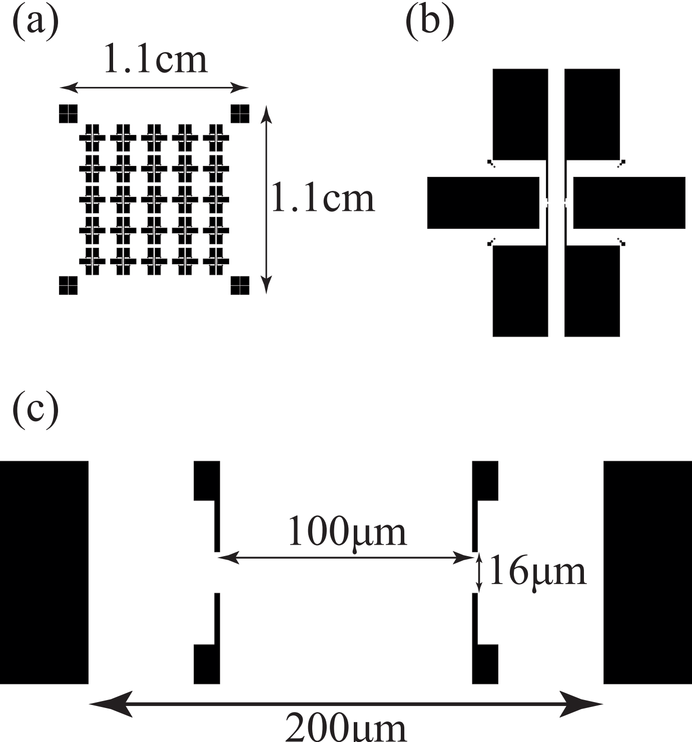

Figure 3-8: Photomask design for the Hall bar contacts. Black areas indicate areas to be exposed and developed for a positive resist. (a) The entire photomask of the 5x5 matrix of Hall bar contacts with alignment markers in the corners. (b) One set of contacts magnified 10x with alignment markers for later fabrication steps now more visible. (c) The Hall contacts in the area that touches the graphene Hall bar enlarged a further 15x.

process, one simply deposits and bakes it on the graphene before the main resist. This bi-layer stack tends to remove much more cleanly than photoresist alone [113] and after removal can result in high-quality devices [159, 134]. In our observation, use of LOR also results in a higher final yield of usable devices due to less undesired graphene removal during lift-off.

Resists are deposited, baked, exposed, and developed according to the recipes in Appendix A. Gold contacts were then deposited after a thin nickel adhesion layer (Fig. 3-1(i)) using physical vapor deposition (PVD). Titanium and chrome are other options for the adhesion layer, but each had a drawback in practice. Lift-off was easy with a Titanium adhesion layer, but it also tended to roll up at the contact edges, and sometimes release from the graphene completely even when using a very thick gold layer on top. Chrome tended to stick very well and not roll up at all, but lift-off was difficult without using an ultrasonic bath, which destroyed the graphene. Nickel gave a very good compromise, sticking to the graphene well enough to not roll up but still allowing lift-off with gentle agitation.

After metal deposition, lift-off is performed in a two-step process. First, the sample is soaked in a bath of acetone, which removes the photoresist and lifts off the excess metal. Since an ultrasonic bath will damage the graphene, excess metal is instead gently removed by squeezing a pipette to agitate the acetone. Second, after all of the excess metal is removed, the LOR layer is removed by being soaked in Microposit Remover 1165 for five minutes. Finally, the sample is rinsed with isopropanol and dried with a nitrogen gun. The result is shown in Fig. 3-1(j).

3.5 Defining the graphene area

Photoresist protects the areas of graphene we want to keep while exposed graphene is removed with O_2 plasma. The plasma is generated with a custom-made plasma asher set to ~300 W, but a reactive ion etcher (RIE) could be used instead. The sample is

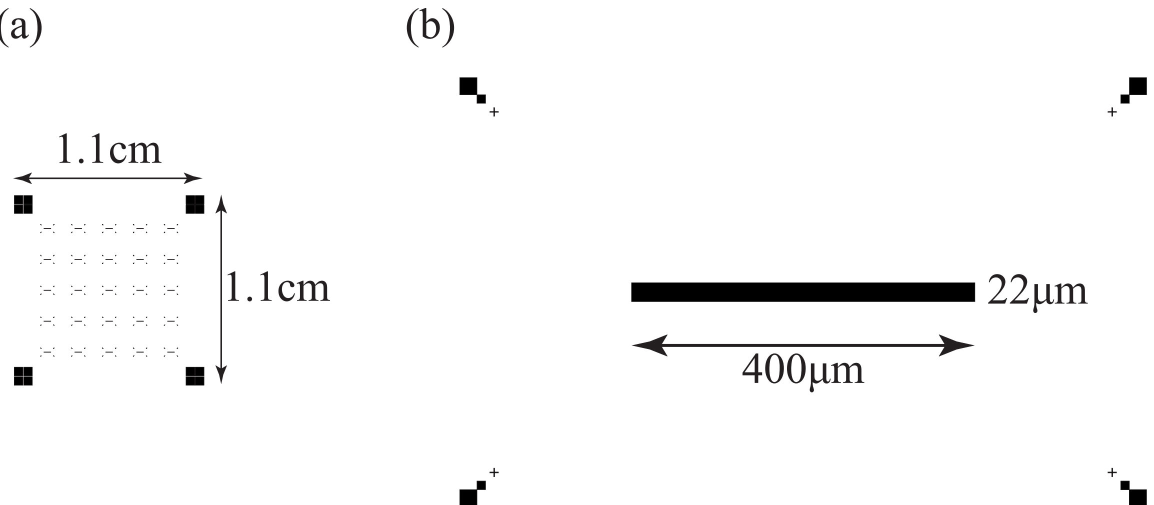

Figure 3-9: Photomask design for defining the graphene into 22 µm wide Hall bars. Alignment markers line up with Hall contacts described above. Black areas indicate areas to block from exposure of a positive resist. (a) The entire photomask for the Hall bars in a 5x5 matrix. (b) One Hall bar pattern enlarged by 150x as compared to a. Alignment markers around the bar are meant to aid in micro-alignments. The length of the bar on the mask is 400 µm. This is much longer than the distance between the end contacts in Fig. 3-8 in order to make it compatible with possible future designs.

chemically cleaned for a final time with acetone and isopropanol, then dried with N_2. Fig. 3-1(k) and 3-11 show the final result.

3.6 Sample mounting and bonding

The sample is glued into a chip carrier using conductive silver paint, which not only holds the sample in place but allows for efficient application of a voltage to the back gate.

Conductive silver paint is available from different manufacturers and made with different solvents in which the silver particles are suspended. While manufacturers do not always disclose the type of solvent used, one can usually tell by the scent. Silver paint with methyl isobutyl ketone (MIBK) works very well for gluing a sample into a chip carrier. The paint used for sample mounting was "Acheson Silver DAG 1415 M,"

available from a number of retailers and found online easily.

Once the sample is in place, wire bonds are made with a “TPT HB02 Manual Wire Bonder” using 25 µm gold wire and a TiC wedge. It is important to note that bonding directly to the gold bonding pads leads to cracks in the oxide layer which result in significant leakage currents, so the bonds are not made directly to the bonding pad. Instead, a bond is first made somewhere far away from the target pad then carefully moved over to the pad using tweezers. One hand then applies silver paint while the other holds the wire steady over the pad. Only a very small amount of paint is needed and can be applied with a sharpened toothpick. This procedure is performed while looking at the sample with the stereomicroscope at the bonding station. The best conductive silver paint for this application is made with an ethanol solvent since it has a good flow and does not dry out too fast. This type of paint is commonly available at many scientific suppliers, though the specific paint used in this thesis is sold in bottles with the description “Silberleitlack Art.-Nr. 530042, 3g” and was purchased from Conrad, a German supplier.

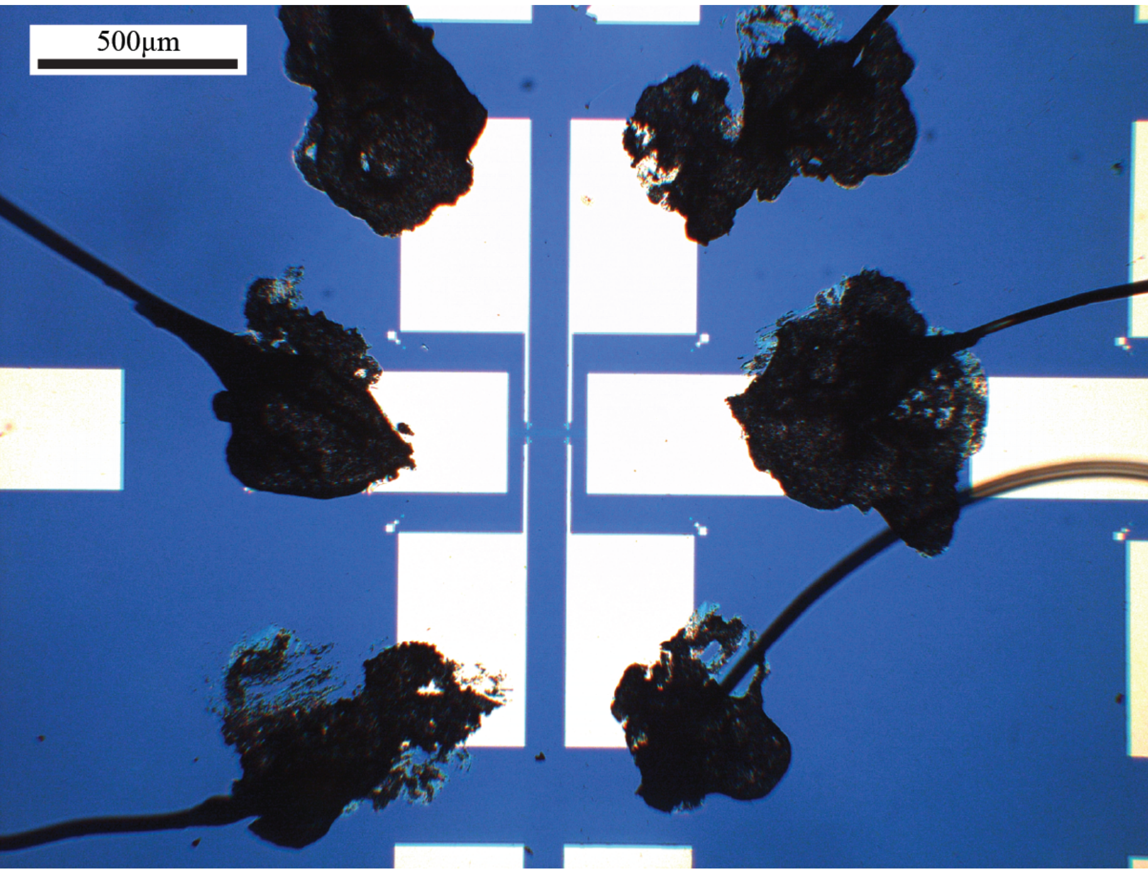

Figure 3-10: Optical microscopy photo taken at 5X magnification of the 200 μm Hall bar used in g-factor measurements. Bonding wires are connected to gold contact pads with conductive silver paint.

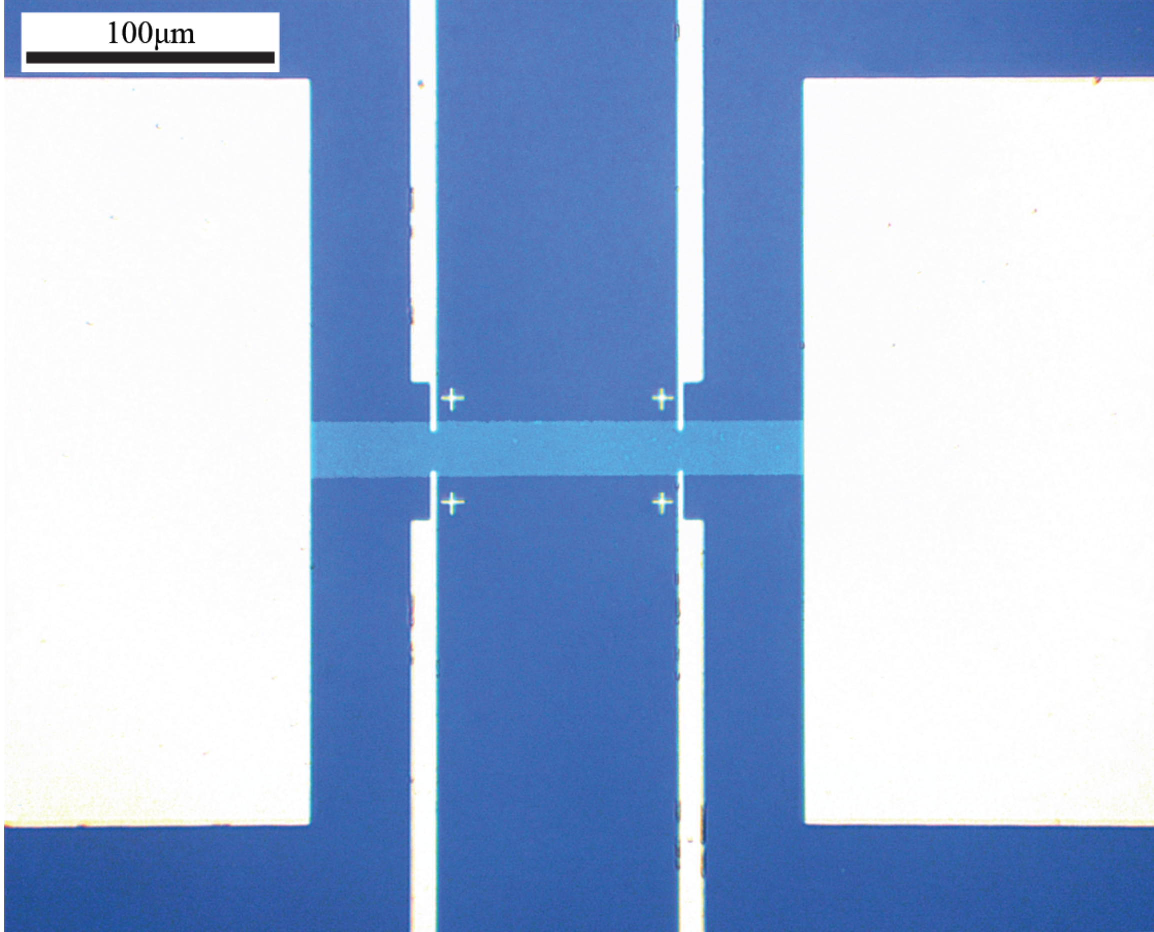

Figure 3-11: Further zoomed in view of the Hall bar in Fig. 3-10 at 20X magnification. Graphene contrast is increased for visual effect.

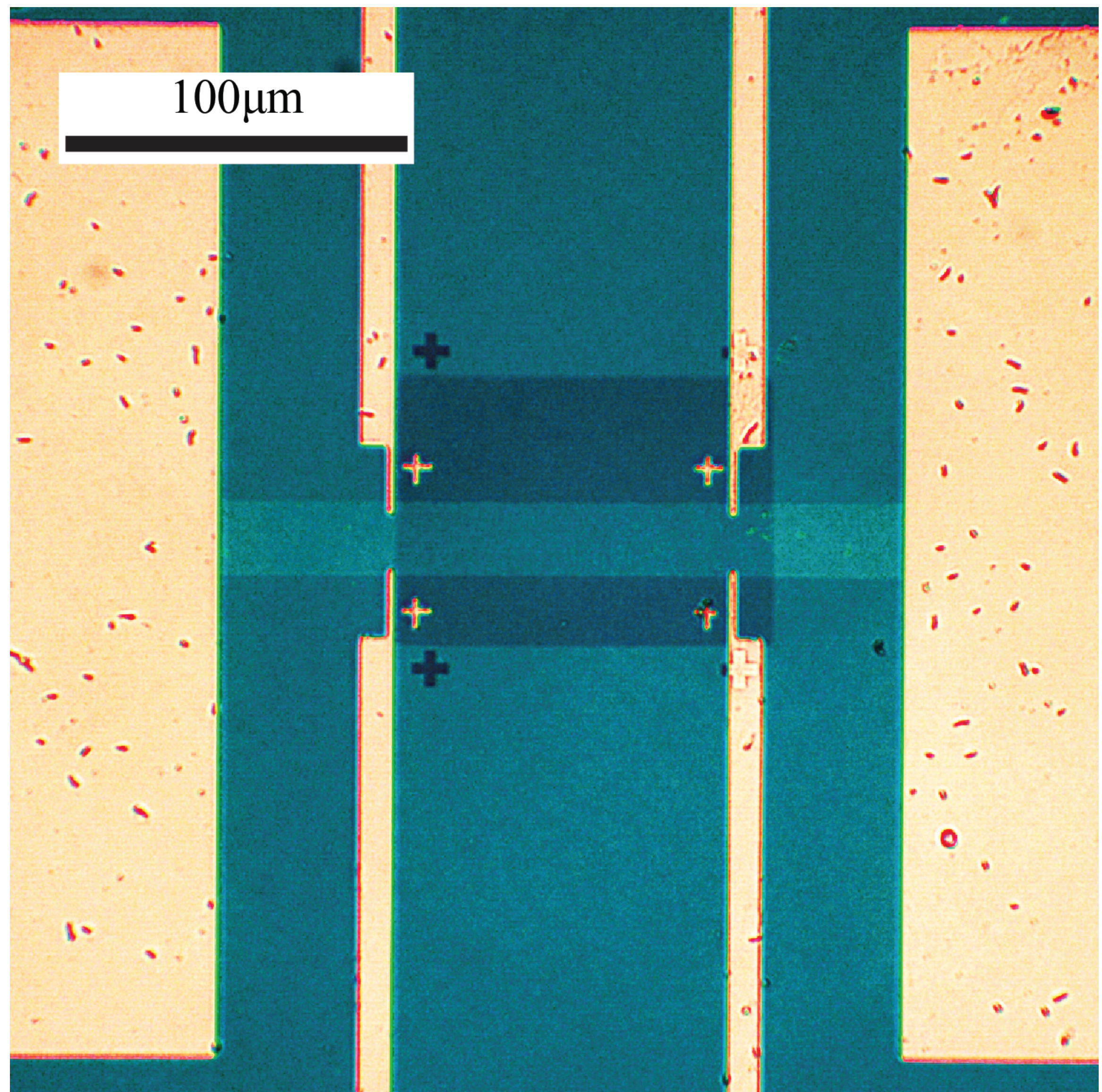

Figure 3-12: Photo of 200 μm Hall bar with 200 nm period analyzed in Chapter 7. Colors adjusted to enhance contrast.

3.7 Thermal annealing

Contaminants such as water must be removed from the graphene to optimize its transport properties. This is done with a two-step annealing process, first under vacuum in a rapid thermal annealer (MTI Corporation OTF-1200-X) to remove as many contaminants as possible, then once more after being mounted in the probe with a tabletop ceramic tube oven (the full procedure is outlined in detail in Appendix A). Both baking steps are performed at a relatively low temperature of 140 °C in order to prevent any possible damage. The annealing measurement setup is described in Sec. 4.3.1 and the results of this process can be seen in Sec. 5.2.

Chapter 4

Measurement setup

This chapter outlines the different experimental setups and equipment required for verification, testing, and measurement of the samples used in this work.

4.1 Leakage tests

All samples were tested to ensure that there was no detectable gate leakage before being considered for further measurements. Leakage currents may sometimes be due to defects in the dielectric layer as delivered from the wafer manufacturer, but they are much more commonly due to cracks that occur from sample preparation and bonding. This is especially true for thin dielectrics, but even 300 nm SiO_2 regularly cracks when a bonder is used to bond gold wire to 50 nm gold pads, leading to leakage currents that can easily be orders of magnitude greater than a measurement current of ~10 nA. This can burn out the sample, or even worse, lead to bad data.

Leakage testing was performed after mounting the samples in the cryostat and after they cooled to 4.2 K. To test for leakage currents, a voltage source (Keithley 230) applied a voltage range of $\pm$101 V to the back gate, and a preamplifier (DL-Instruments OTF-1200-X) in series with a 1 MΩ safety resistor was successively connected to each device contact to detect any leakage currents. The voltage output of the preamplifier

was read out with an HP multimeter, and no detectable leakage currents were detected outside of the noise floors of the measurement equipment, down to the picoampere range. This is three orders of magnitude less than the lowest current applied to any samples in this thesis, so leakage current is not considered to be a significant factor in any of the measurements described here.

4.2 Cryostat

The primary cryostat used for these measurements was an Oxford Instruments liquid ^{4}He cryostat with a superconducting magnet capable of 8 T at 4.2 K. Before measurement, the sample is mounted inside of a probe that is pumped to ~1×10^{-3} mbar before adding a small amount of helium gas. The probe is then placed inside of the cryostat insert, with the sample positioned carefully within the middle of the solenoid in order to experience the expected target magnetic field, and cooled to 4.2 K.

4.3 Resistive measurements

4.3.1 Annealing monitoring

As described earlier, the first thermal annealing step for each sample is completed before mounting inside the cryostat probe and the second step is performed after.

While baking, the total resistance of the Hall bar can be used as a rough metric for the cleanliness of the graphene. Contaminants adsorbed from the air act as dopants, adding charge carriers and moving the charge neutral point (CNP) further away from zero gate voltage. These excess charges also add extra scattering centers and worsen the mobility of the sample.

The resistance measured over the ends of the Hall bar depends on the bar geometry. It was observed that flat graphene samples made with this method in a 200 µm × 22 µm geometry had a resistance that started anywhere from 20-40 kΩ and tended to about

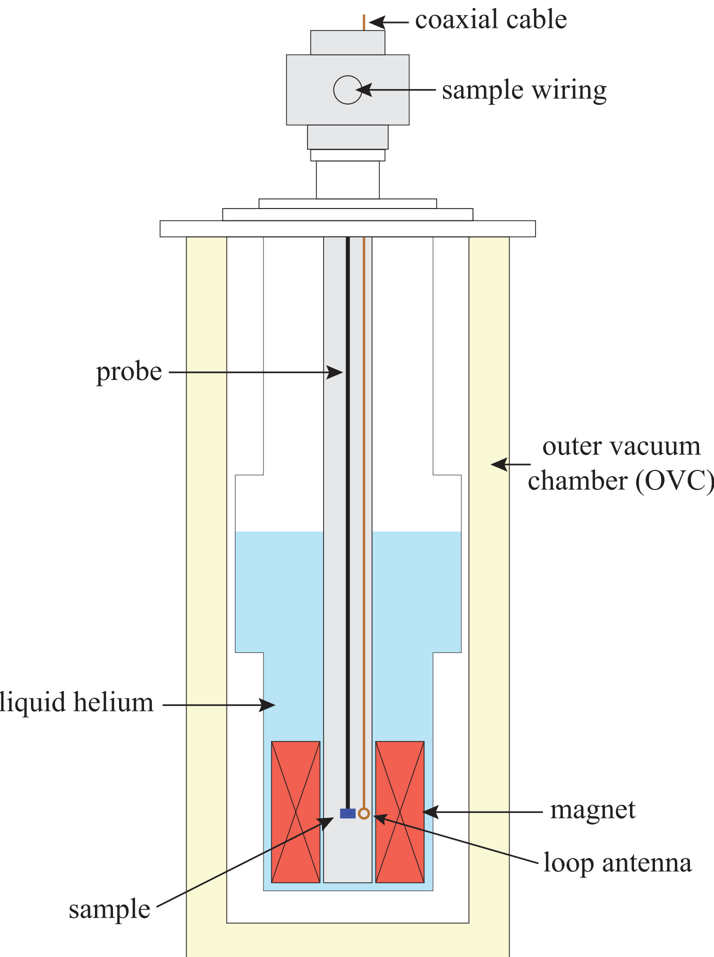

Figure 4-1: Oxford Instruments liquid helium cryostat with 8 T superconducting magnet. The probe has a coaxial cable connected to a loop antenna that is aimed at the sample.

57 kΩ at the end of the second annealing step.

4.3.2 Electrical contact resistance

Electrical contact resistance, or just contact resistance, is the contribution of the metal-graphene interface to the total resistance of the system. While not a focus of the research presented here, it can be a useful metric for device performance. To find the contact resistance R_c, two-contact and four-contact resistance measurements are made and then plugged into the equation

$$R_c = \frac{W}{2}\left[R_2 - R_4\left(\frac{l}{L}\right)\right] \tag{4.1}$$

where R_2 is the two-contact measurement across the ends of the Hall bar, R_4 is the four contact resistance, W is the width of the channel, l is the length between the end contacts of the Hall bar, and L is the distance between the voltage contacts in the four-contact measurement [81].

Contact resistances for the samples presented in this thesis were measured to be ~1 kΩ µm which is reasonable for samples prepared with no special steps taken to minimize contact resistance [137], though the value calculated here is only used as a general metric for reasonable contact since we did not take into account the dependence of R_c on gate voltage [108]. If reduced contact resistance is needed in future samples, further steps can be added to the fabrication process, including using O_2 plasma to remove contaminants before metal deposition [135] or creating excess zigzag edges in the contact area [81].

4.3.3 Magnetotransport

Magnetotransport measurements were made with two Stanford SRS 830 lock-in amplifiers. The samples measured in this experimental setup were all relatively low resistance (< 100 kΩ). When a sample is placed in series with a much larger resistance

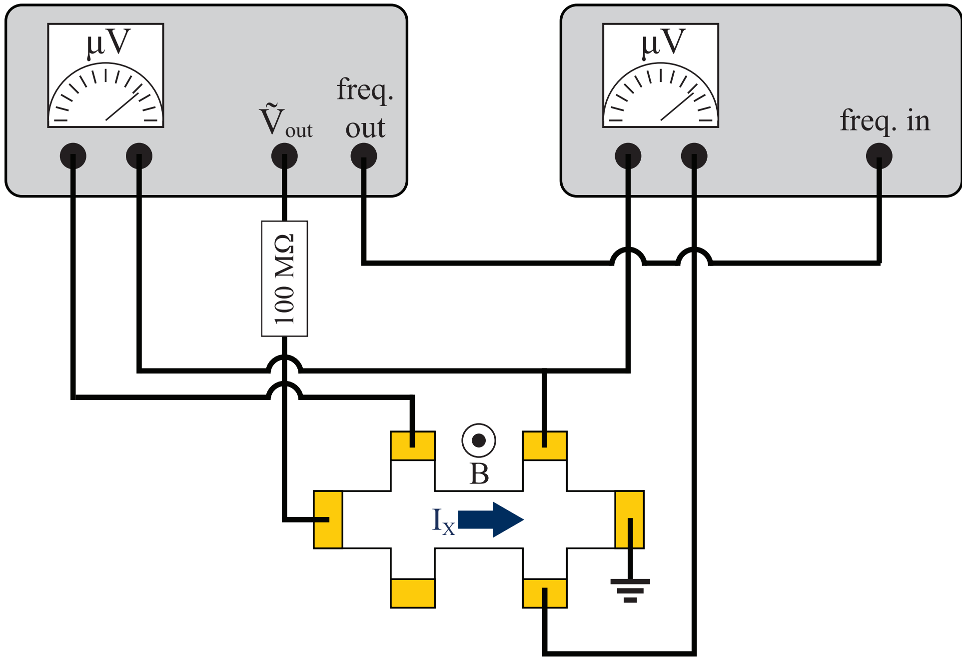

Figure 4-2: Dual lock-in measurement setup. The connection of the back gate to a voltage source is not shown.

(100 MΩ), an AC signal (1 V_{RMS}, 37 Hz) is converted to an approximately constant current (~10 nA). Each lock-in was configured to measure AC voltage drops at the same frequency as the signal with one connected to a pair of longitudinal contacts and the other connected to a pair of Hall contacts. Voltage was applied to the back gate by a Yokogawa 7651 with a low-pass filter to remove line noise.

4.3.4 Microwave-induced ESR

A custom probe for the cryostat was designed and constructed to perform measurements with a microwave source radiating on the sample. A 50 Ω stainless steel coax line (Micro-Coax UT-085B-SS) was placed in the probe to connect a microwave signal generated by a source (Agilent E8257D) to deliver to a rotatable loop antenna placed very close to the sample. A diagram of the probe placement in the cryostat is seen in Fig. 4-1 and a close up photo and schematic of the loop antenna placement in relation to the sample are seen in Fig. 4-3.

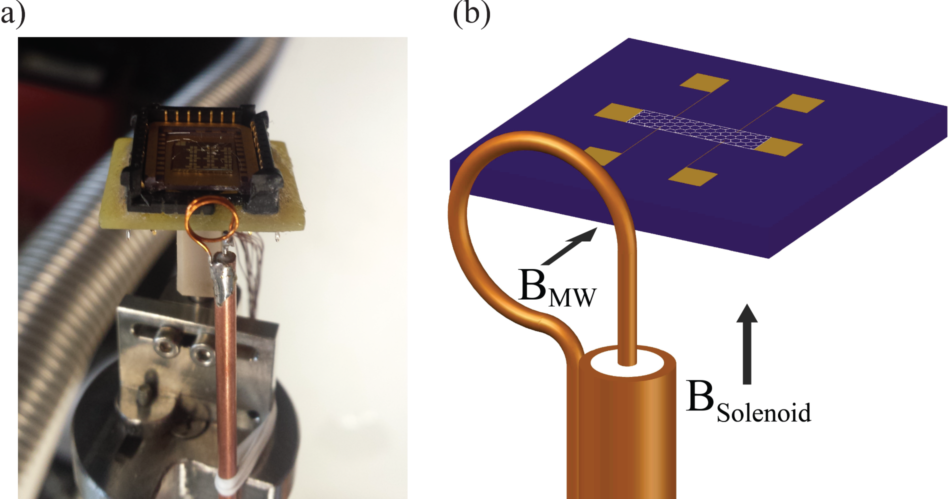

Figure 4-3: Images of a sample mounted in probe with a loop antenna. (a) Photograph (Two-loop antenna is shown, though a single loop is used in the ESR measurements detailed in Ch. 6.) (b) Schematic denoting the orientations of fields in relation to the sample (3D rendering done with assistance from Joshua Hunt).

The antenna is a simple loop antenna with an approximate self inductance of $L_{Loop} = 68.5\,\mathrm{nH}$ that is calculated with [30]

$$L_{Loop} \cong N_{\mathrm{Loop}}^2 \mu_0 \mu_{\mathrm{r}} \frac{D}{2} \left(\ln \left(\frac{8D}{d} \right) - 2 \right), \tag{4.2}$$

where $D = 4.4\,\mathrm{mm}$ is the loop diameter, $d = 0.4\,\mathrm{mm}$ is the wire diameter, $N_{\mathrm{Loop}} = 1$ is the number of turns, μ_0 is the permeability of free space, and $\mu_{\mathrm{r}} \approx 1$ is the relative permeability of air or helium gas. Impedance matching at $Z = 50\,\Omega$ results in a frequency of $f = 116\,\mathrm{MHz}$. The sample is placed close enough to the loop to be in the near field of emitted radiation, and the loop diameter is more than 40 times the size of the graphene device length under test, resulting in the sample experiencing an approximately uniform field.

Now we calculate an order of magnitude estimate of the maximum magnetic field that the loop antenna can deliver to the sample. We assume that the device under test is about $r = 3\,\mathrm{mm}$ from the sample and that all of the power from the signal generator is emitted so that $P = 20\,\mathrm{dBm} = 100\,\mathrm{mW}$. The Poynting vector describes

the rate of energy transport per unit area of an electromagnetic field and is written as

$$\boldsymbol{S} = \frac{1}{\mu_0}\boldsymbol{E} \times \boldsymbol{B}. \tag{4.3}$$

For a sinusoidal electromagnetic wave we get the result

$$S = \frac{c_0 B_\mathrm{m}^2}{2\mu_0} \tag{4.4}$$

where B_m is the amplitude of the magnetic field component, c_0 is the speed of light in vacuum, and μ_0 is the permeability of free space. If we approximate the radiation pattern as spherical and recognize that the power delivered to the sample is

$$P = SA = \frac{c_0 B_\mathrm{m}^2}{2\mu_0}\left(4\pi r^2\right) \tag{4.5}$$

then the magnetic field at the sample is approximated by

$$B_\mathrm{m} = \sqrt{\frac{\mu_0 P}{2\pi c_0 r^2}}. \tag{4.6}$$

Using the approximations and the values stated above results in a magnetic field magnitude of $B_\mathrm{m} \approx 50\,\mu\mathrm{T}$. We must remember that this is only an estimate, especially given that the assumptions used in this calculation are not completely accurate, especially those regarding the radiation pattern and the total power that is radiated by the antenna. However, since we measure electron spin resonance peaks while the superconducting magnet generates static fields on the order of $1\,\mathrm{T}$ we can safely say the applied microwave radiation is much weaker by comparison and plays a strictly perturbative role in the experiments.

4.4 Data acquisition and analysis

A number of software packages were used to perform data acquisition and analysis. Labview 2013 by National Instruments was used to write custom programs to control the instruments and collect data for resistive measurements, including ESR experiments. Analysis of the data including curve fitting was performed with Origin 2015 by OriginLab.

Chapter 5

Large area graphene characterization

The 200 µm × 22 µm flat graphene Hall bar in Fig. 3-11 was extensively measured to derive many relevant characteristics and verify the high-quality of the graphene sample.

5.1 Raman analysis

Raman spectra were taken at multiple locations to verify the reproducibility of the measurements as well as the quality and uniformity of the graphene monolayer. Measurements were performed using a Renishaw inVia Raman Microscope with a 532 nm laser and a 100X objective with numerical aperture NA=0.85 allowing for a spot size of 382 nm. All measurement points showed very similar peaks. Three representative measurement points are shown in Fig. 5-1.

From this, we can immediately see that the graphene is monolayer not only due to the peak shapes and locations but also because the ratio between the 2D and G peaks is much larger than unity. The D peak is very small, the G and 2D peaks are sharp, and the D′ peak is practically non-existent, all of which hint toward good quality and

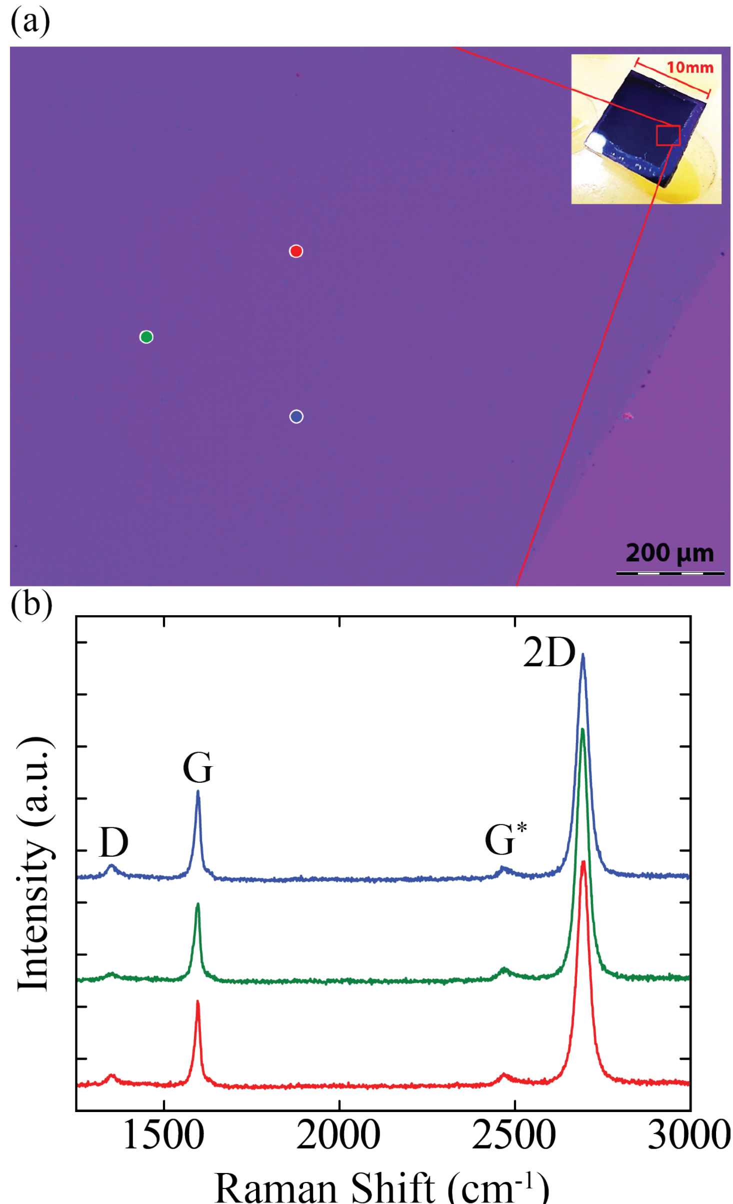

Figure 5-1: (a) Optical microscopy image of a large clean area of graphene (dark purple) on an SiO_2 substrate (light purple). Inset: Picture of a 1 cm × 1 cm SiO_2 wafer with CVD graphene on top (dark blue). (b) Raman spectra with a 532 nm laser taken at the colored spots shown in (a), displayed with an artificial offset for clarity. The defect peak D is very small in all three measurements, which speaks for a high quality of graphene. Also, due to the relative height of the G peaks to the 2D peaks, which is about one third, we can confirm that we see a monolayer of graphene [38].

Table 5.1: Point defect density (n_D) and distance between defects (L_D) calculated from Raman measurements.

Point (color)	L_D (nm)	L_D error (nm)	n_D ($\times 10^{10}\,\mathrm{cm}^{-2}$)	n_D error ($\times 10^{10}\,\mathrm{cm}^{-2}$)
red	30	16	3.6	1.0
green	34	18	2.8	0.77
blue	31	16	3.3	0.92

low defect density. G* appears as expected though is not used for this analysis.

Point defect density, n_D, and the distance between defects, L_D are now found by analyzing the ratio of the D and G peaks by using Eq. 2.66 and 2.67 for the three points in Fig. 5-1.

Interestingly, L_D is on the order of the ballistic mean free path, l_m, which is calculated later in this chapter. This may suggest that some of the defects that give rise to the D peak are also primarily responsible for the limited value for l_m. More analysis is needed to verify if this is indeed the case.

5.2 Annealing

The longitudinal resistance is measured over a range of applied gate voltages at a temperature of 4.2 K at zero magnetic field. The sample is annealed under vacuum for 16 hours at 350 °C to remove all water, including water trapped between the graphene and substrate. The sample is then removed from vacuum and quickly mounted in a probe, and once again annealed in a tube oven under vacuum (Fig. 3-1(l)) at 140 °C for 72 hours to remove any water absorbed from the atmosphere during mounting. During this time, the 2-point resistance of the Hall bar is observed to steadily increase from approximately 25 kΩ to a new maximum of 57 kΩ. Fig. 5-2 shows the increase in peak longitudinal resistance along with a dramatic shift of the charge neutral point (CNP) from V_g=27 V to −4 V before and after annealing, respectively, which is evidential of the concentration of charged impurities being significantly reduced [1]. The large peak

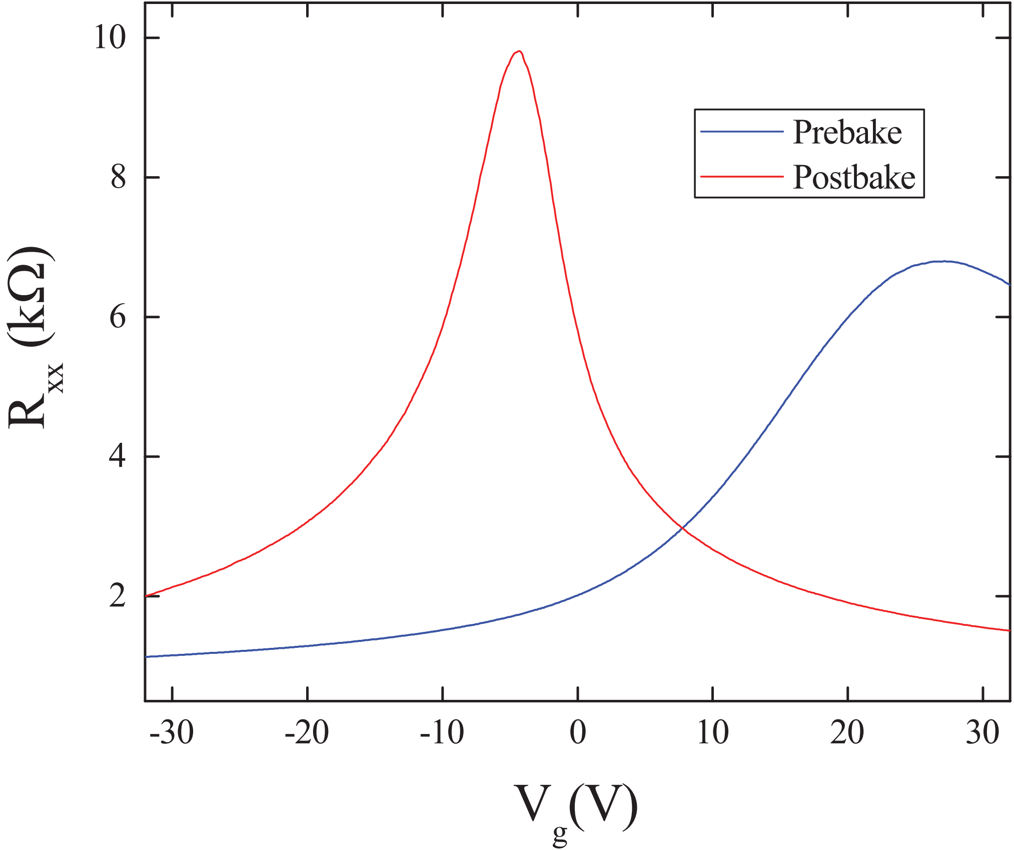

Figure 5-2: Longitudinal resistance R_{xx} of the graphene strip versus gate voltage V_{g} before (blue) and after (red) baking out the sample. The measurements were recorded at $T = 4.2\,\mathrm{K}$. A possible explanation for the postbake shift of the CNP of over 30 V is the removal of contaminants on the graphene that act as dopants, originating from resist residues or the atmosphere.

shift is indicative of the removal of a majority of p-type dopants such as water [120]. The settling of the CNP at a negative gate voltage may be due to doping by the metal contacts or contact doping by SiO_2 and any contaminants trapped between the graphene and metal during processing [43, 108].

The shape of the resistance curve and the location of its peak can provide insight into graphene contaminants and doping effects. Adsorbents can preferentially affect carrier mobility of either electrons or holes as well as move the CNP [61, 37], but even clean graphene can display asymmetric behavior and a CNP shift due to doping from metal contacts [43, 108]. This doping causes a p-n junction to form when the

gate voltage is set such that the graphene has opposite charge carriers to the dopants, reducing mobility. This doping effect depends on the metal/graphene interaction and is not simply due to the difference in work functions, $\Delta\Phi$ [43]. The picture is further complicated by the effect of contaminants that can be trapped between the metal and graphene, especially from organic compounds used in sample preaparation [108].

A 5 nm layer of nickel is used as the adhesion layer for the gold contacts. Previous work on graphene FETs has seen nickel contacts provide holes as dopants [106, 108], but experimental evidence of n-doping of graphene on a clean Ni(111) surface has been observed as well [122].

Water has been previously seen as a common p-type dopant on graphene [120]. The measured peak shift in Fig. 5-2 implies that many p-type dopants were removed during the annealing stages, in agreement with the assumption that water is being removed, though other contaminants introduced during processing may also have doping effects [125].

The shape of the postbake curve in Fig. 5-2 is only slightly asymmetric with the left side tail being slightly higher than the right side indicating that the mobility of holes is slightly worse than that of electrons. A previous study reported the charge transfer region at the metal/graphene interface to extend ~0.5 µm into the channel [166]. This is a much smaller distance than our sample channel length of 200 µm suggesting that the observed asymmetry in the resistance is less likely to be influenced by metal contact doping than by contaminants. The location of the CNP in the negative voltage region indicates that the graphene channel region is n-doped at $V_{\mathrm{g}} = 0\,\mathrm{V}$ which agrees with the picture of the p-doping of the graphene under the metal contacts, though any effects due to adsorbents cannot be ruled out. Further tests would need to be done to analyze any contaminants. However, both the shape of the resistance peak, as well as its large shift after baking off contaminants, imply relatively clean graphene.

The postbake shift in the CNP that arises from sweeping the gate voltage in opposite directions is at most 0.1 V. When there is still a significant amount of water

on the substrate, this hysteresis can easily be on the order of a few or even tens of volts [65, 164, 107, 63]. This effect is typical of graphene on SiO_2 and the relatively low hysteresis seen in this sample implies that most of the water has been removed by the previous annealing step [79]. Other work has used hydrophobic substrates such as hexamethyldisilazane (HMDS) to reduce the amount of dipolar adsorbates such as water [79], which in turn reduces hysteresis, but as shown here a 2-step thermal annealing process also results in small hysteresis of large graphene devices on SiO_2 without requiring extra substrate layers.

Finally, we can invert the resistivity graph to find the minimum conductance to be $G_0 \approx 2.66e^2/h$. This is reasonably close to other experiments that have found values near $4e^2/h$ [152, 41].

5.3 Magnetotransport

Magnetotransport measurements were taken according to the procedures outlined in Sec. 4.3.3 and the analysis of these measurements are presented here.

5.3.1 Transport properties

The mobility and charge carrier density were found for nine different back gate voltages. These measurements were performed by setting the back gate and then measuring R_{xx} and R_{xy} while sweeping the magnetic field perpendicular to the Hall bar and then applying equations 2.33 and 2.34 on the data around B=0. A summary of these results is shown in Fig. 5-3. The charge carrier density is linear with respect to gate voltage away from the charge neutral point (CNP), which implies the gate oxide provides the dominant capacitive effect which is expected due to the oxide thickness [36]. The rounding of the charge carrier density graph near the CNP is due to charged electron/hole puddles induced by charged impurities, including those in the substrate [1].

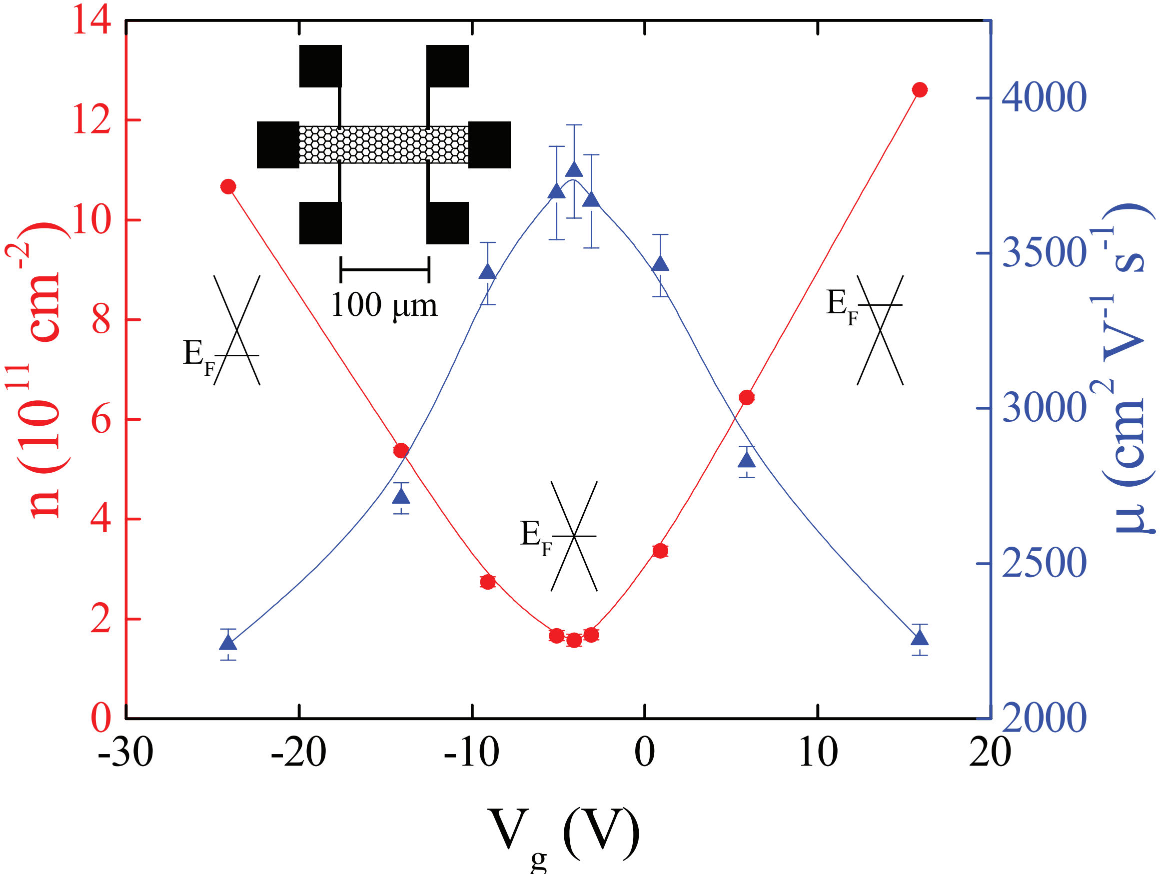

Figure 5-3: The charge carrier density (red) and mobility (blue) versus the gate voltage V_{g} at 4.2 K after the final annealing step. The values were obtained by performing magnetoresistance measurements at the displayed values for V_{g}. Points are connected by B-spline curves. The charge carrier density is linear with respect to gate voltage away from the CNP, implying that the gate oxide provides the dominant capacitive effect which is expected due to the oxide thickness [36]. Inset: Schematic of the graphene strip and contacts.

At the CNP, the Hall mobility is measured to be around $\mu_{\mathrm{CNP}} = 3{,}760\,\mathrm{cm^2\,V^{-1}\,s^{-1}}$ and the charge carrier density $n_{\mathrm{CNP}} = 1.58 \times 10^{11}\,\mathrm{cm^{-2}}$. These measurements show that the fabrication method results in a mobility that approaches values obtained when using exfoliated graphene on SiO_2 [57]. This implies that the graphene is very clean and has been minimally damaged by the sample production process.

Charge carrier density can also be calculated by analyzing Shubnikov-de Haas oscillations and applying Eq. 2.44. However, for this sample, only the measurements made when the gate is set to $V_{\mathrm{g}} = V_{\mathrm{CNP}} \pm 20\,\mathrm{V}$ can be evaluated with this method as they are the only two measurements that displayed more than one complete oscillation. In each case, the n calculated from the frequency of the SdH minima was less than 1% different from the value derived from the Hall measurements, implying that there was no significant leakage or parallel conduction in the sample.

The derivative of the n vs. V_{g} curve can be taken to find the Fermi velocity by using Eq. 2.42; for the data presented above this results in a relatively constant $v_{\mathrm{F}} = 1.1 \times 10^6\,\mathrm{m\,s^{-1}}$, which is very similar to values found in other work for experiments of graphene on SiO_2 [175, 28, 153, 75] and will thus be used for all further calculations.

Table 5.2 displays derived physical quantities found from magnetotransport measurements including charge carrier density, mobility, Fermi energy, ballistic mean free path, Fermi wavelength, and charge carrier effective mass.

Table 5.2: Calculated values from magnetoresistance measurements performed on 200 µm Hall bar at different gate voltages (Gate voltage relative to CNP ($V_g - V_{CNP}$), charge carrier density (n, Eq. 2.33, +/− signifies electrons/holes), mobility (μ, Eq. 2.34), Fermi energy (E_F, Eq. 2.23), ballistic mean free path (l_m, Eq. 2.35), Fermi wavelength (λ_F, Eq. 2.12), and charge carrier effective mass (m^*, Eq. 2.43)).

$V_g - V_{CNP}$ (V)	n ($\times 10^{11}$ cm^{-2})	μ (cm^2 V^{-1} s^{-1})	E_F (meV)	l_m (nm)	λ_F (nm)	m^* (m_e)
-20	-10.7	2240	-133	27.0	24.3	0.019
-10	-5.38	2710	-94.1	23.2	34.2	0.014
-5	-2.74	3430	-67.2	21.0	47.9	0.010
-1	-1.66	3700	-52.4	17.6	61.4	0.008
0	1.58	3760	50.9	17.4	63.1	0.007
1	1.68	3670	52.6	17.5	61.1	0.008
5	3.36	3460	74.4	23.4	43.2	0.011
10	6.44	2830	103	26.5	31.2	0.015
20	12.6	2250	144	30.0	22.3	0.021

5.3.2 Quantum Hall levels

The magnetic field is then set to 8 T and the gate voltage is scanned once more at 4.2 K. Multiple quantum Hall levels were seen, as shown in Fig. 5-4. Clear plateaus for the Hall resistance, R_{xy}, at filling factors of $\nu = \pm 4(n + 1/2)$ and Landau level index $n = 0, 1, ...$ are seen with corresponding drops in the longitudinal resistance, R_{xx} [175]. The Hall conductance is calculated by Eq. 2.39 and further emphasizes the quantum Hall effect occurring at the lower filling factors, as seen in Fig. 5-5.

5.3.3 Weak localization

Weak localization peak fits were performed on the graphene Hall bar used for graphene g-factor analysis over a range of gate voltages according to the theory outlined in Sec. 2.2.4. The peak fit equation only works for positive values of the magnetic field. Though there is some asymmetry in magnetoresistance measurements due to a slight mixing of R_{xx} and R_{xy}, the WL peak itself is highly symmetric. The characteristic scattering lengths were extracted from the fits with data summarized

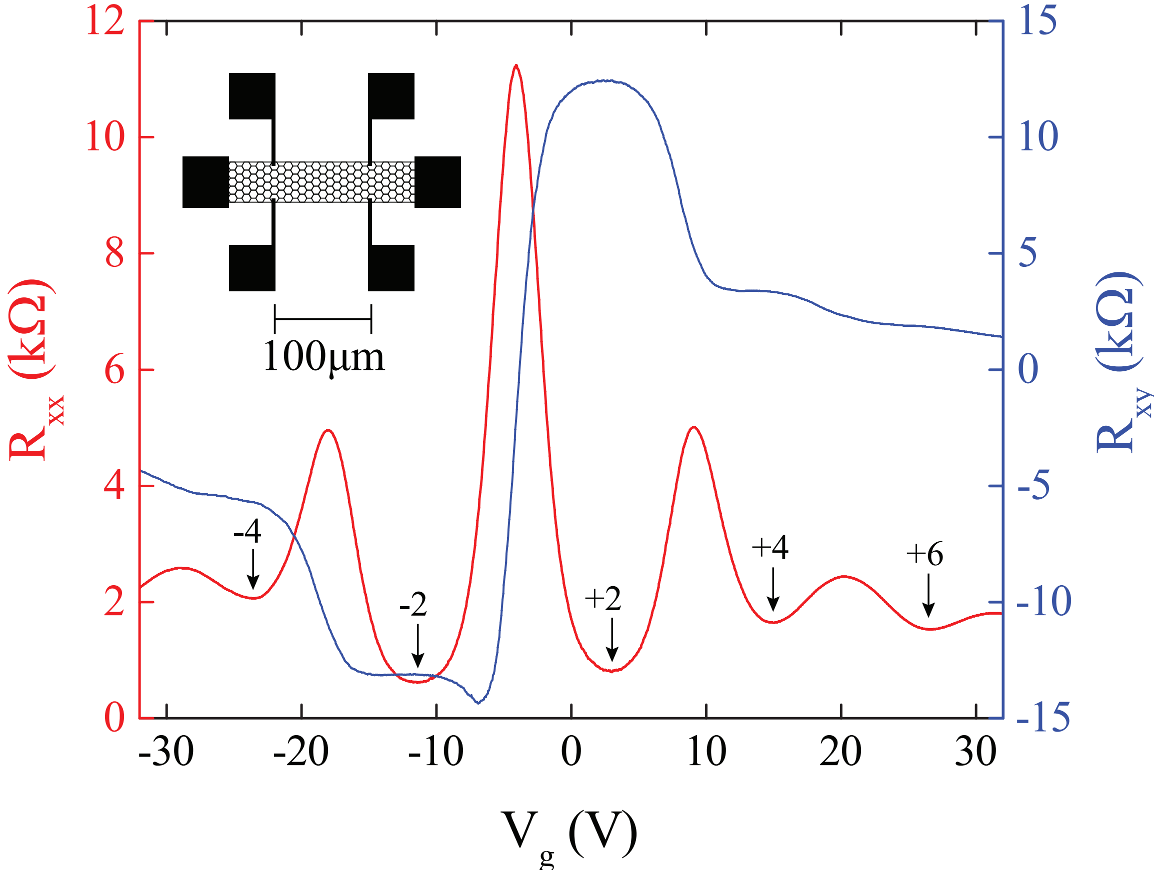

Figure 5-4: The longitudinal (red) and Hall resistance (blue) versus the gate voltage V_g at fixed magnetic field $B = 8\,\mathrm{T}$ measured at 4.2 K, obtained through a standard 4-point-measurement approach, show multiple quantum Hall levels. Inset: Schematic of the graphene strip and contacts.

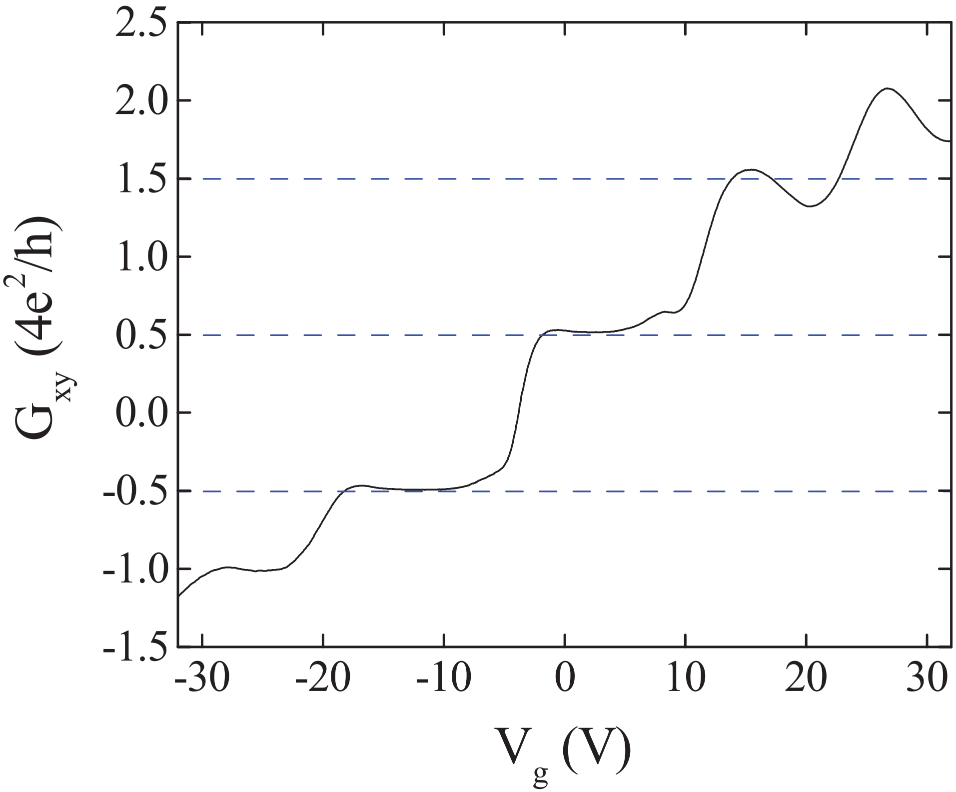

Figure 5-5: Hall conductance for the same sample measured in Fig. 5-4 (in units of $4e^2/h$). Clear plateaus for Hall conductance are seen. Blue dashed lines represent theoretical quantum Hall levels in monolayer graphene.

in Fig. 5-7 and 5-8. As can be seen in Fig. 5-6, peak fits match very well for the entire measurement range, implying that two carrier transport provides the primary contribution to magnetoresistance in this sample.

The elastic scattering length, $L_e \approx 0.1\,\mu m$, may be relatively constant because elastic scattering primarily depends on atomically sharp defects such as grain boundaries (intervalley scattering) that do not change with varying carrier density. The graphene datasheet from the manufacturer notes grain sizes up to $10\,\mu m$ though grain sizes on the order of L_e are likely to exist. Elastic intravalley scattering may explain the slight downward trend in L_e with increasing gate voltage.

The phase coherence length, L_ϕ, is minimized at V_{CNP} due to increased inelastic scattering. Previous work has shown that electron-hole puddles can increase inelastic scattering between charge carriers via both a direct electron-electron interaction and the interaction of an electron with the fluctuating electromagnetic field generated by the movement of neighboring electrons, with both effects leading to phase breaking [72, 101].

The Anderson localization length, L_c, is larger than L_ϕ at all gate voltages, which means the sample is always in the weak localization regime and never in the strong localization regime. L_c is minimized at the charge neutral point and appears to be roughly linear on both sides of the graph, hinting at a possible dependence on the charge carrier density. Indeed, this relationship was found by other works, and it is likely due to induced charge carriers screening charged impurities [105, 4].

5.4 Capacitance

Quantum capacitance depends on charge carrier density, as shown by Eq. 2.27, and the largest calculated value for the measurements in this work is $C_{Q,Max} = 2.8 \times 10^{-2}\,F\,m^{-2}$. This is much larger than the expected value of the gate oxide capacitance for a 300 nm thick layer of SiO_2, $C_{ox} = 1.15 \times 10^{-4}\,F\,m^{-2}$, leading to a change in the total system

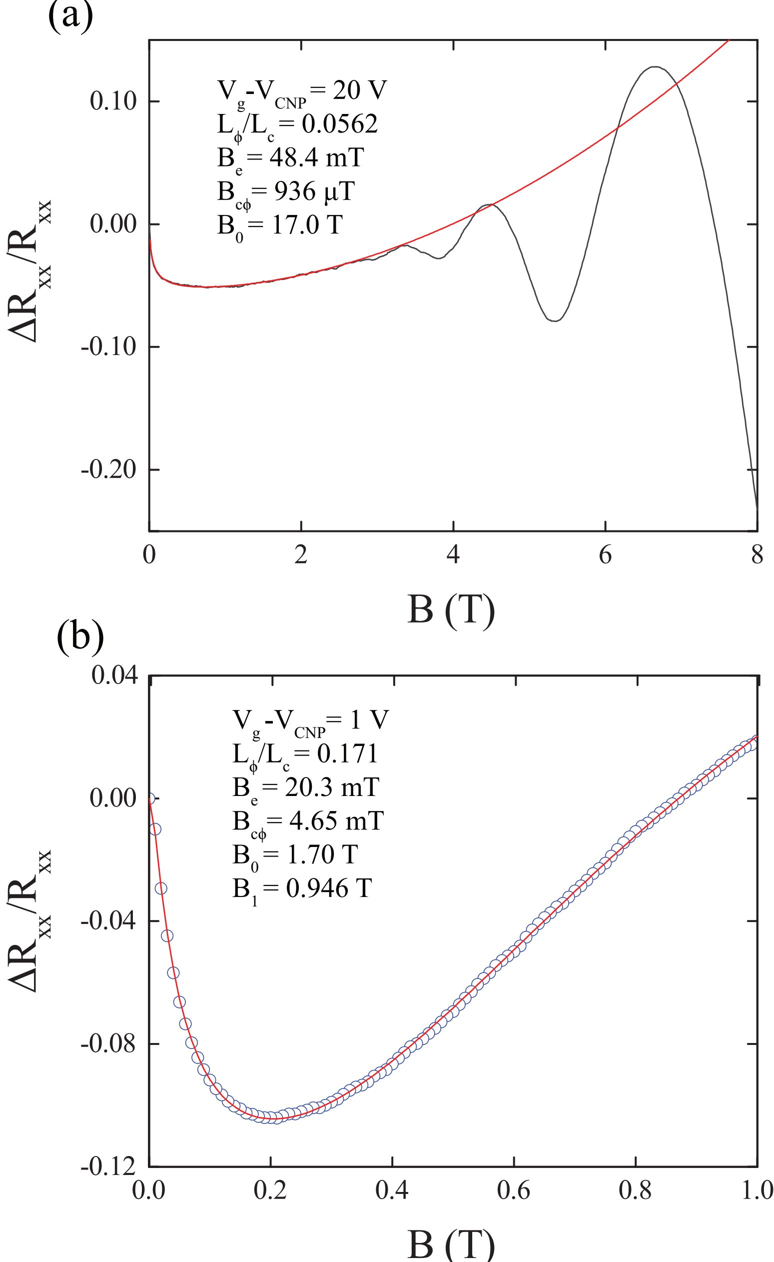

Figure 5-6: Typical weak localization peak fits. (a) A very good fit (red) for the entire measurement with the gate set to 20 V above the CNP (black). B_1 is too large to affect the fit. (b) Zoomed in fit (red) for the gate set to 1 V above the CNP (blue circles).

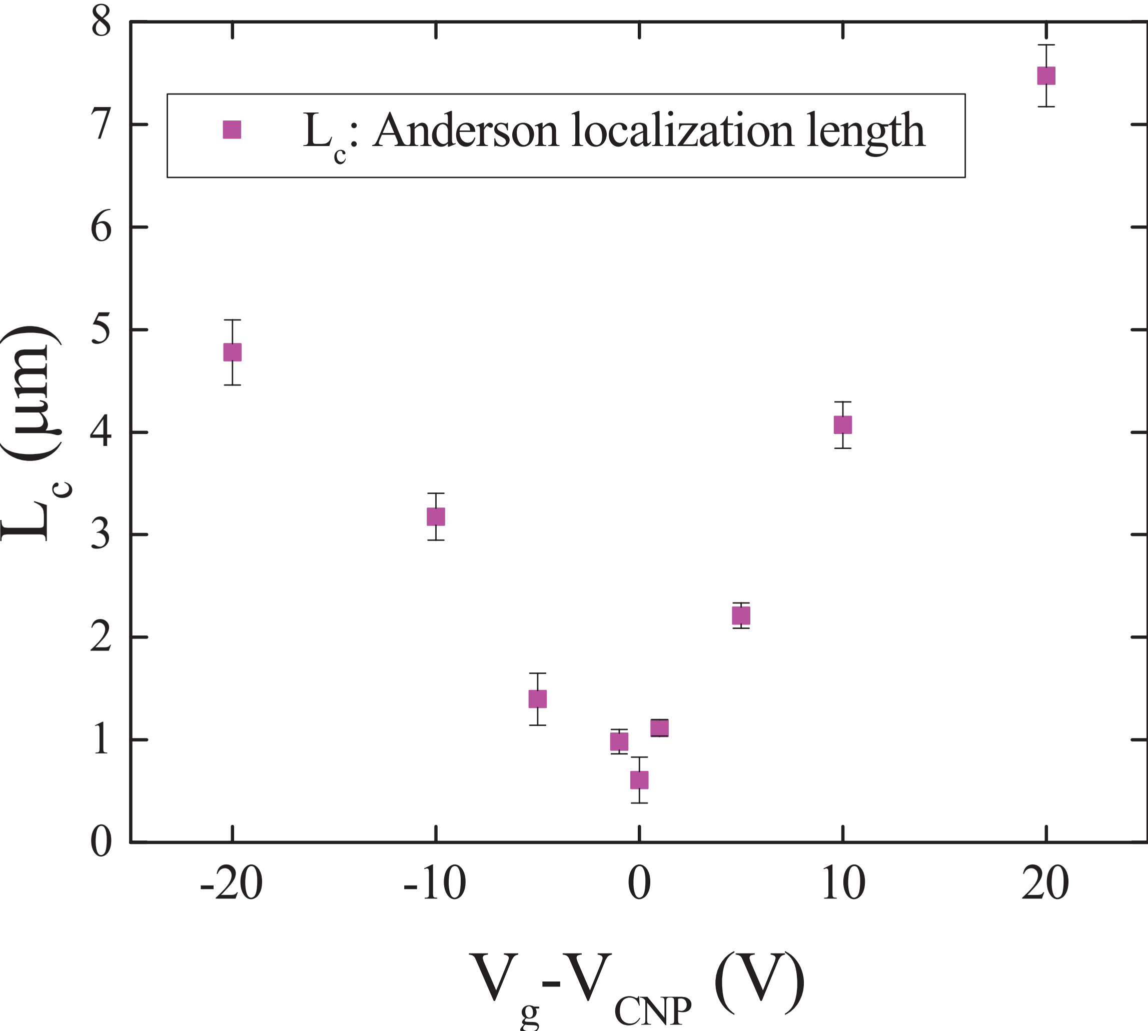

Figure 5-7: Characteristic Anderson localization lengths from WL peak fits. The minimum value is found when $V_{\mathrm{g}} = V_{\mathrm{CNP}}$.

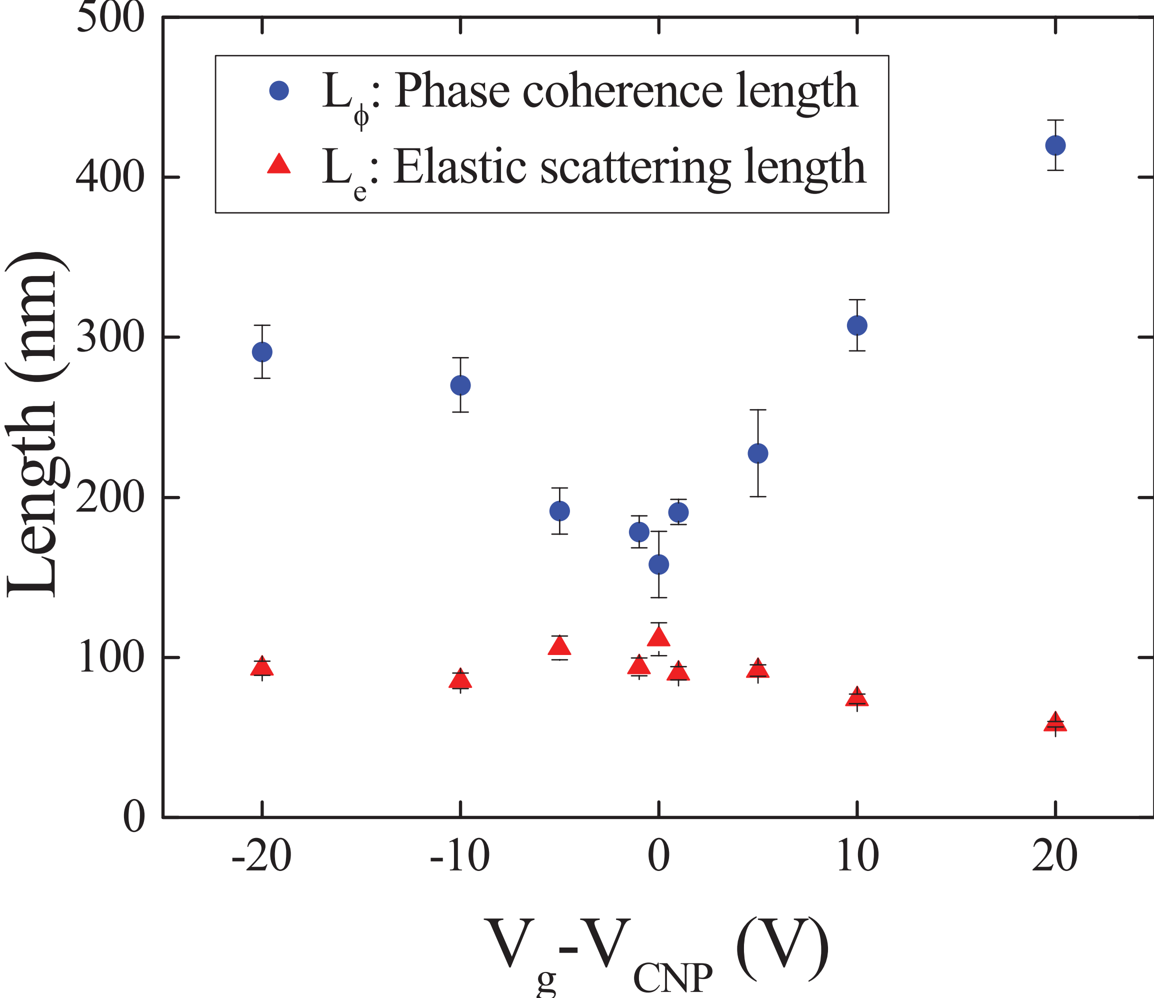

Figure 5-8: Characteristic phase coherence and elastic scattering lengths from WL peak fits. Phase coherence length (blue circles) increases as the gate is moved away from V_{CNP} while the elastic scattering length (red triangles) is relatively constant.

capacitance of less than 0.4%. The effect of quantum capacitance is overwhelmed by the 5% manufacturing tolerance of the oxide thickness and thus is ignored as an insignificant contribution to the total capacitance of the system.

As described in equations 2.28 and 2.29, the slope of the linear region on each side of the charge carrier density graph in Fig. 5-3 can be used to calculate the total capacitance. These equations result in $\alpha_+ = 6.17 \times 10^{10}\,\mathrm{V^{-1}\,cm^{-2}}$ and $\alpha_- = 5.29 \times 10^{10}\,\mathrm{V^{-1}\,cm^{-2}}$ for the electron (+) and hole (−) sides, respectively, leading to total capacitances of $C_{\mathrm{tot},+} = 8.47 \times 10^{-5}\,\mathrm{F\,m^{-2}}$ and $C_{\mathrm{tot},-} = 9.88 \times 10^{-5}\,\mathrm{F\,m^{-2}}$. These values are different enough from the expected value of C_{ox} for 300 nm to imply a measurable contribution to the capacitance from sources such as charged impurities or trapped charges.

5.5 Charged impurities

The charged impurity density, n_{imp}, is now estimated using residual carrier density $n^* = n_{\mathrm{CNP}} = 1.58 \times 10^{11}\,\mathrm{cm^{-2}}$ by a self-consistent formalism described in Section 2.5. Using equations 2.65 and 2.64 with $d \approx 1$ being the average distance between charged impurities and the graphene sheet and the interaction parameter $r_{\mathrm{s}} \approx 0.8$ for SiO_2, it is found that $n_{\mathrm{imp}} \approx 5 \times 10^{11}\,\mathrm{cm^{-2}}$. This is a typical value for the concentration of charged impurities in a SiO_2 substrate [36], which may imply that the substrate is the most significant source of charged impurities in this sample.

Chapter 6

The *g*-factor of graphene

This chapter describes the results of electron spin resonance (ESR) experiments on the 200 µm × 22 µm flat graphene sample characterized in Ch. 5. The g-factor of graphene is calculated from multiple measurements of the locations of ESR peaks to find its dependence on charge carrier type, density, and mobility. Half-widths of the ESR peaks are then extracted from these measurements to find spin relaxation times. In addition, a theoretical analysis of the origin of the measured peaks is presented.

6.1 ESR measurements

The measurement setup for ESR measurements is described in Ch. 4. Magnetoresistance measurements were made with two Stanford Research Systems SR830 Lock-in Amplifiers. Microwave frequencies were generated with an Agilent E8257D signal generator. All measurements are done at a temperature of 4.2 K in a liquid helium cryostat with a solenoid magnet capable of generating a field of 8 T. The sample was mounted inside the solenoid such that the field is perpendicular to the plane of the Hall bar. A radio frequency (RF) signal is then sent down a coaxial cable and radiates from a loop antenna mounted to the end of the coaxial cable. A schematic of the setup is shown in the inset of Fig. 6-1. Several frequencies f in the range of 15 to 31 GHz

which produce a standing wave are chosen for the measurements described below. This assures maximum RF power transmission to the graphene sample. Additionally, the charge carrier density of the graphene is varied by adjusting the back gate voltage. ESR measurements are performed for each frequency at nine different accessible charge carrier densities, around and including the charge neutral point (CNP) at $V_{\mathrm{g}} = -4\,\mathrm{V}$. The magnetic field B was incremented in steps of $0.01\,\mathrm{T}$, and this value was used as the uncertainty in determining ESR peak locations.

Plots of the change in magnetoresistance induced by applying RF radiation of varying power are shown in Fig. 6-2, with $\Delta R_{xx} = R_{xx}(\mathrm{RF}) - R_{xx}(\mathrm{dark})$. We attribute the resistance minima around $\pm 0.5\,\mathrm{T}$ to electron spin resonance. In this case, the applied radiation acts as a tipping field causing microwave-induced heating of the charge carriers, which in turn leads to a decrease in resistance at resonance [10, 54]. Thermal activation of charge carriers by RF irradiation thermally changes the charge carrier density by only ~1%. The temperature dependence of the electrical conductivity of any particular piece of graphene emerges due to a complex interplay of competing mechanisms [2, 21, 54]; in this sample, it is likely that activated transport across electron-hole puddles is the most significant effect, leading to the observed inverse relationship between resistance and temperature [83]. As displayed in Fig. 6-2, varying the applied RF power does not result in significant differences in peak widths or positions. The weak localization peak around $B = 0\mathrm{T}$ [7, 151, 103, 71, 35] is also altered by RF irradiation, which corroborates our claim that the observed changes in resistance are caused by charge carrier heating. The maximum RF power which could be applied with our source at all frequencies is $20\,\mathrm{dBm}$ and is used for all of the following measurements. ESR peak locations are shown in Table 6.1.

For each gate voltage, a linear relationship is found between the frequency of the applied microwave radiation and the magnetic field at which the resonance peak appears. This relationship is shown in Fig. 6-3, in which the sample is tuned to the charge neutral point, $V_{\mathrm{g}} = -4\,\mathrm{V}$. The linear fit for this graph results in a slope of

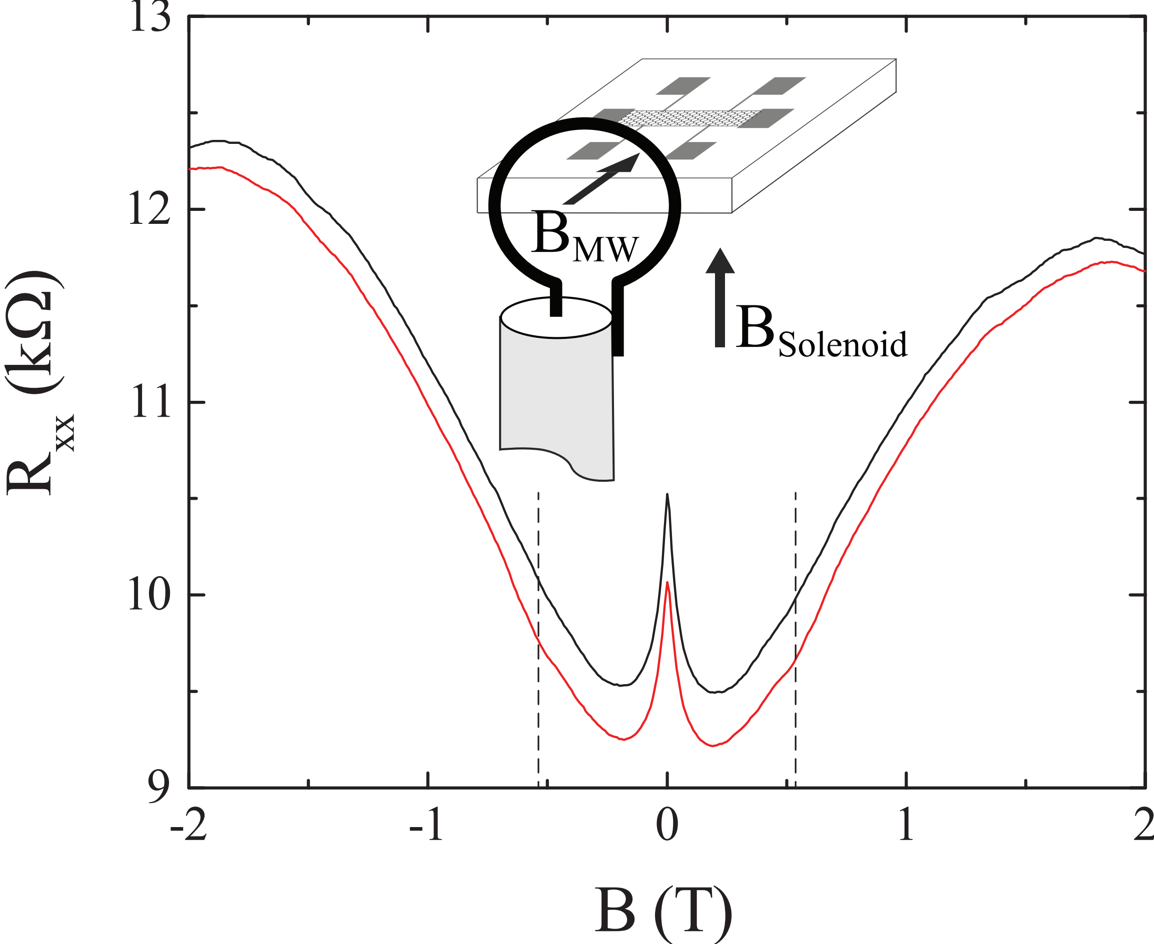

Figure 6-1: Measurements of longitudinal resistance both with (red, below) and without (black, above) applied RF at 15 GHz and 23 dBm, before subtraction to find ΔR_{xx}. Inset: Diagram of the experimental setup. The solenoid magnetic field is perpendicular to the plane of the Hall bar. Microwave radiation is applied in the plane of the sample and perpendicular to applied current by a coaxial cable connected to a loop antenna which is mounted near enough to the sample to be in the near-field regime.

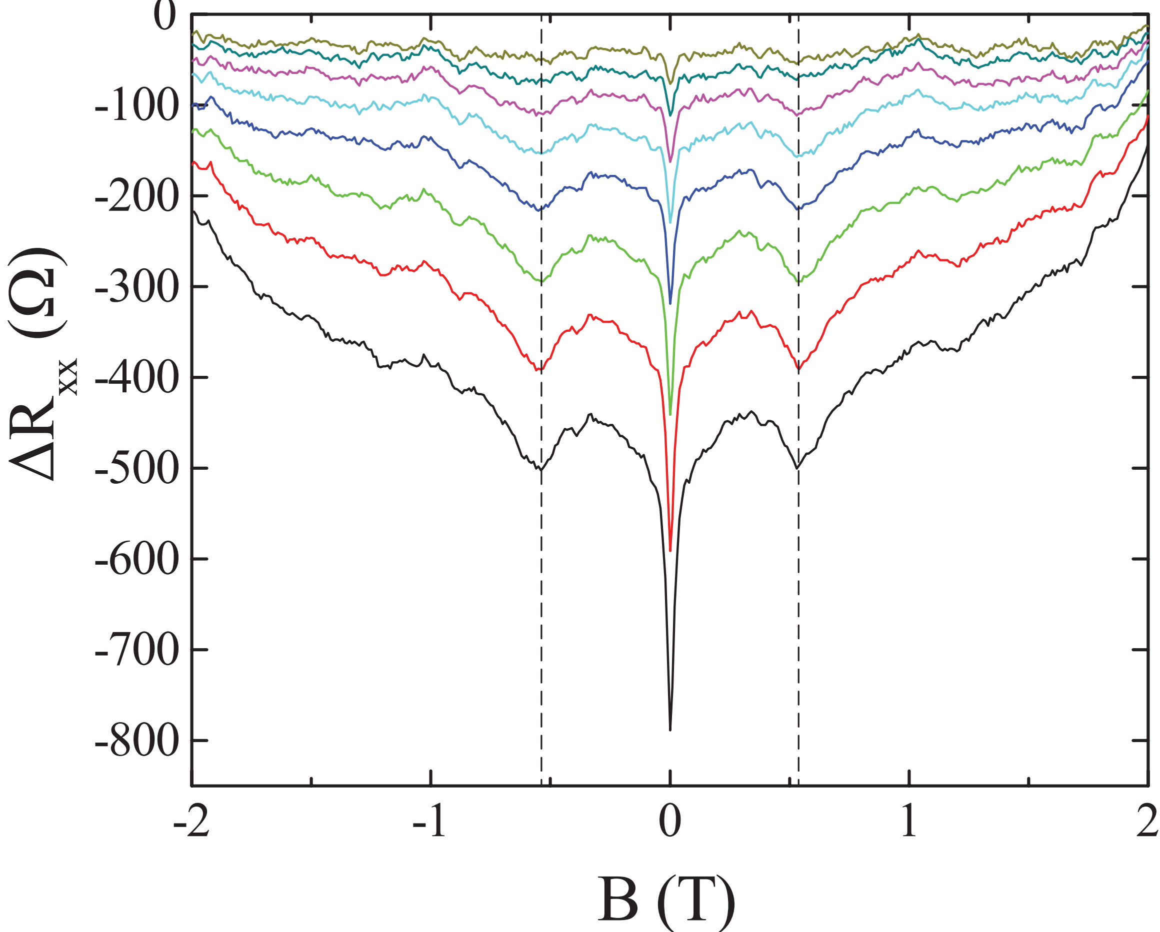

Figure 6-2: ΔR_{xx} for 15 GHz RF signal at different applied RF power levels, with a back gate voltage of $V_{\mathrm{g}} = -5.0\,\mathrm{V}$. Varying RF power does not change the ESR peak position. It is also found that ESR peak width does not appear to be significantly dependent on RF power once it is over a measurable threshold. Power levels are, from top to bottom, 9 dBm to 23 dBm in steps of 2 dBm. Note that the peaks remain stationary with increasing RF power which implies that there is no measurable temperature dependence for the g-factor.

Table 6.1: ESR peak locations at different RF frequencies and back gate voltages relative to the charge neutral point ($V_g - V_{CNP}$). RF power is constant at 20 dBm.

	−20 V	−10 V	−5 V	−1 V	0 V	1 V	5 V	10 V	20 V
15 GHz	0.55 T	0.55 T	0.55 T	0.55 T	0.55 T	0.55 T	0.55 T	0.55 T	0.55 T
19 GHz	0.70 T	0.69 T	0.69 T	0.69 T	0.70 T	0.70 T	0.70 T	0.70 T	0.70 T
21.5 GHz	0.79 T	0.78 T	0.77 T	0.78 T	0.79 T	0.79 T	0.79 T	0.78 T	0.78 T
23.6 GHz	0.87 T	0.87 T	0.87 T	0.87 T	0.88 T	0.87 T	0.87 T	0.88 T	0.87 T
27 GHz	0.99 T	0.98 T	0.98 T	0.99 T	0.98 T	0.99 T	0.98 T	0.99 T	0.99 T
29 GHz	1.07 T	1.06 T	1.05 T	1.05 T	1.07 T	1.06 T	1.06 T	1.06 T	1.07 T
31 GHz	1.14 T	1.14 T	1.14 T	1.14 T	1.14 T	1.14 T	1.14 T	1.13 T	1.14 T

$\mathrm{d}F/\mathrm{d}B = 27.3 \pm 0.3\,\mathrm{GHz\,T^{-1}}$. As was discussed in Sec. 2.3, this slope is used to find the magnitude of the g-factor, $\left|g_{\parallel}\right| = 1.95 \pm 0.02$, from

$$g = \frac{\mu}{\mu_B}, \quad \mu = h\frac{\mathrm{d}F}{\mathrm{d}B}, \tag{6.1}$$

and μ_B being the Bohr magneton. Measurements at different carrier densities give very similar results and are summarized in Fig. 6-4. There is no apparent no dependence of the g-factor on charge carrier type, density, or mobility. However, it should be noted, we are only able to determine the absolute value of the g-factor. Since the change in resistance at resonance is caused by heating, the sign of the magnetic moment has no detectable effect. The g-factors extracted for the nine different charge carrier densities have a mean value and standard deviation of $\left|g_{\parallel}\right| = 1.952 \pm 0.002$ and the mean value lies within the uncertainty of every individual g-factor. Our results are compatible with the value of $g_{\parallel} = 1.94 \pm 0.024$ reported by Mani *et al.* for holes in graphene on silicon carbide.

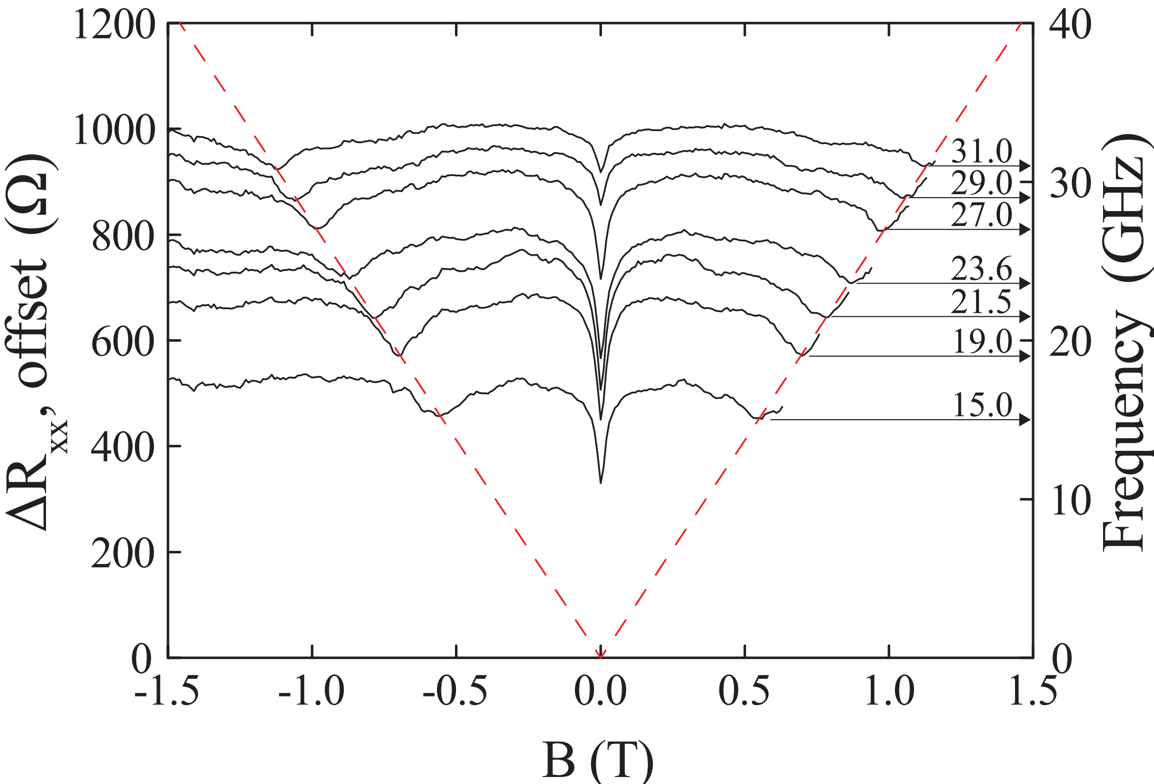

Figure 6-3: ΔR_{xx} for different frequencies at V_{CNP}, with offsets to emphasize ESR peak shift due to g-factor. The traces are offset to make the peak value in resistance coincide with the microwave frequency at which the magnetoresistance curve was recorded.

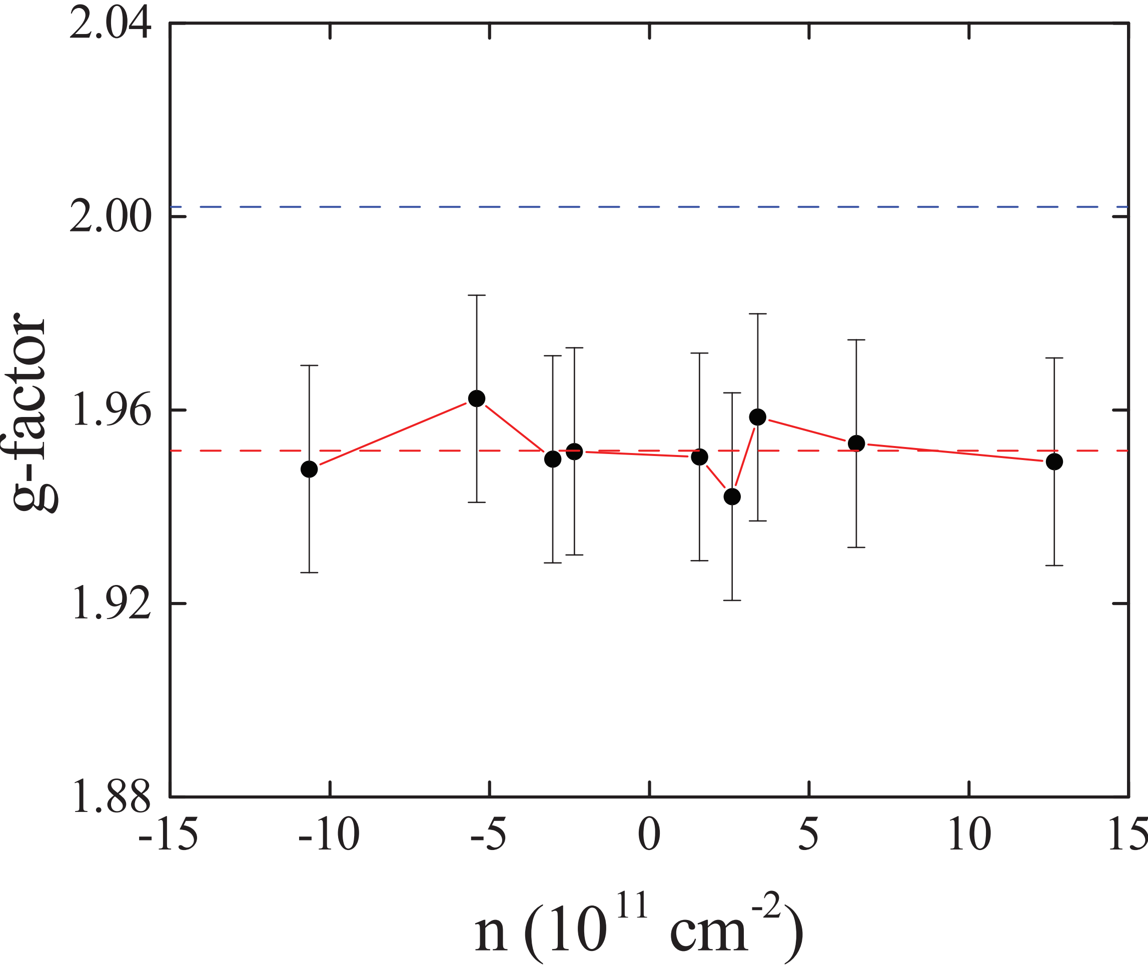

Figure 6-4: Calculated g-factor at different charge carrier densities. Negative numbers represent holes. The red dashed line shows the mean value of g-factor measurements and the blue dashed line indicates the g-factor of the free electron.

6.2 g-factor origins

We now analyze the different origins of g-factors that have either been predicted or measured in graphene or similar systems to determine the source of the g-factor measured in this work.

Previous studies with $B \perp c$-axis have shown results that are compatible with $g_\perp = 2$, by Zeeman splitting in universal conductance fluctuations on exfoliated graphene with contacts separated by about $3\,\mu\mathrm{m}$ [89], and by Zeeman splitting of spin states on a quantum dot ($d \approx 70\,\mathrm{nm}$) [49]. The results of these studies are less precise than those described here and could thus be considered compatible, though it is important to reiterate that they were performed with the magnetic field in a different orientation.

Earlier reports of ESR studies on graphite revealed a dependence of the g-factor on temperature as well as the external magnetic field orientation B relative to the (out of plane) c-axis [97, 58]. These studies indicate that when $B \perp c$-axis, $g_\perp$ is essentially constant with respect to temperature and very close to that of the free electron, with $g_\perp = 2.0023$. In contrast, when $B \parallel c$-axis, such as in the measurements described in this thesis, there is an inverse relationship between $g_\parallel$ and temperature, with $g_\parallel$ ranging from around 2.05 to over 2.15 as the temperature is lowered from 300 K to 4.2 K due to changes in effective electron density. As can be seen from Fig. 6-2, peak locations in our measurements do not change with increasing RF power. Since increased microwave excitation causes a higher carrier temperature we can deduce that there is no measurable effect on our measured g-factor due to temperature. The previously mentioned studies also predict that there is a g-factor shift relative to the value for the free electron, Δg, in quasi-2D graphite that is either positive or negative as the dominant charge carrier changes between electrons and holes respectively.

This variance is not seen in our graphene measurements with $\Delta g \simeq g - 2 \simeq -0.05$, but one might expect charge carriers in graphene to have a different g-factor compared to that of graphite due to its properties such as a Dirac-like linear dispersion relation

and zero band gap, as well as possibly different QED corrections. Substrate effects may play a role, and it should be noted that our results on Si/SiO_2 are compatible with measurements on SiC performed by Mani *et al.* within experimental error.

Similar experiments done on other 2D systems such as GaAs have been shown to measure the g-factor of the free charge carriers [148]. The dispersion relation in GaAs is parabolic, in contrast to the linear dependence in graphene. GaAs-Al_xGa_{1-x} heterostructures also show a clear dependence of the g-factor on charge carrier density. In addition to the free charge carriers, there are a number of other possible physical origins for the observed g-factor of $g \approx 2$ in graphene including vacancy defects and adatoms.

The magnitude of magnetic moments due to vacancy defects varies depending on their type and other properties of the system [93, 172, 138, 112, 163], with the highest predicted values resulting in $g \approx 1.5 - 2$ for defects on graphene ripples under strain [138]. Nanometer-sized ripples in graphene appear even when deposited on a substrate such as SiO_2 with a maximum local strain of approximately 1% [62], though due to the essentially random nature of grain boundary orientation on CVD graphene it is unlikely that these ripples would be oriented in a way that would produce our g-factor signal. Irradiation of graphene with Ar^+ ions [67] can result in vacancy defects with $g = 2.001 - 2.003$ while N^+ ion bombardment [117] can implant ions that produce a g-factor of 2.

Adatoms have a wide range of potential g-factors, but the most commonly studied adatoms, H and F, have been theoretically predicted [172, 74] to have $g = 1$ and have experimentally [110, 45] resulted in $g < 1$. Tin and iron adatoms [20] are predicted to result in a $g \approx 2$. Adatoms in general, however, tend to cluster together when placed on graphene, which can drastically reduce induced moments [70, 33, 20, 124, 110]. It has also been shown that magnetic moments in graphene due to adatoms can be tuned by changing the charge carrier density by applying a gate voltage [111, 129]. This tuning effect is highly dependent on the concentrations and types of adatoms,

but we do not see any trend in our measurements that could imply adatoms are the primary cause of our measured g-factor.

Theoretical studies of charge carrier interaction at high magnetic fields predict an effective g-factor $g^* = 2 - 4$ that oscillates depending on the filling factor ν and averages to a value of 2.3 with a high enough charged impurity concentration in the substrate [78, 162].

Vacancy defects are likely to be present in our sample and those of Mani *et al.*, and the predicted g-factors are roughly in the correct range of $g \approx 1.5 - 2$. Also, the associated g-factors should be less sensitive to changes in charge carrier density than free charge carriers. However, there is no change in g-factor as a function of charge carrier density at all, as could be expected from charge carrier density dependent Kondo screening. Also, theoretically predicted g-factors due to vacancy defects do not precisely match the measured g-factor. Some metal atoms do produce similar g-factors on graphene as those measured here, and it is possible that some metal adsorbates could be present due to the copper foil that the graphene was grown on; however, they should not be present in Mani's epitaxially grown samples. Furthermore, no theoretically predicted g-factor due to metal adatoms precisely matches our measured g-factor.

Out of all of the possible origins of the measured g-factor described, the free charge carriers are the most compelling. A similar measurement approach performed on GaAs-Al_xGa_{1-x} heterostructures measured the g-factor of free charge carriers, and the spin lifetime measured here from ESR peak widths is comparable to that of free charge carriers in graphene found by other techniques. However, we did not measure a change in g-factor as a function of charge carrier density contrary to what would be expected by the previous theory of the g-factor shift in quasi-2D graphite. It is also important to reiterate that the sign of the g-factor should change when transitioning from electrons to holes, however, our measurements only yield the absolute magnitude of the g-factor.

Table 6.2: Relevant systems with a g-factor near 2

System	g-factor	References	Experiment or Theory
C defects/vacancies	$\sim 1-2$	[93, 172, 138, 112, 163, 117, 67]	Both
Metal adatoms	$0.17-3.41$	[20]	Theory
Electron interaction effects	$2-4$ (effective)	[78, 162]	Both
2D graphite, $B \perp c$-axis	2.0023	[97, 58]	Experiment
2D graphite, $B \parallel c$-axis	$2.05-2.15$	[97, 58]	Experiment
Graphene, $B \perp c$-axis	2	[89, 49]	Experiment

6.3 Spin lifetime

Based on the resonance peak widths we also calculate the spin lifetime using Eq. 2.59 with $\Delta E = \mu \Delta B$ as the energy for the Zeeman splitting due to the applied magnetic field, and ΔB is the resonance half-width of the ESR peaks. The resonance half-width is found to have no clear dependence on charge carrier density, applied RF power, or frequency outside of measurement error, and is generally found to be $\Delta B \approx (0.080 \pm 0.015)$ T. This results in a spin relaxation time of approximately $\tau_s \approx (40 \pm 6)$ ps. With this value, we then use Eq. 2.62 to find the spin diffusion length at the CNP to be $\lambda_s \approx (0.63 \pm 0.05)$ μm where D is the diffusion constant [158] found with Eq. 2.61. These values are consistent with many previous experiments [157, 53, 66, 50, 64, 52].

Graphs displaying the relatively constant ESR peak widths with respect to all adjustable parameters are shown in Fig. 6-5, 6-6, and 6-7. Fig. 6-8 displays the result of characteristic Lorentzian peak fits at different charge carrier densities with constant RF power and frequency. Fig. 6-9 scales the fits in Fig. 6-8 in order to emphasize the relatively constant ESR peak widths found in this work. All of the peak widths measured fall within the range of $\approx (0.16 \pm 0.03)$ T.

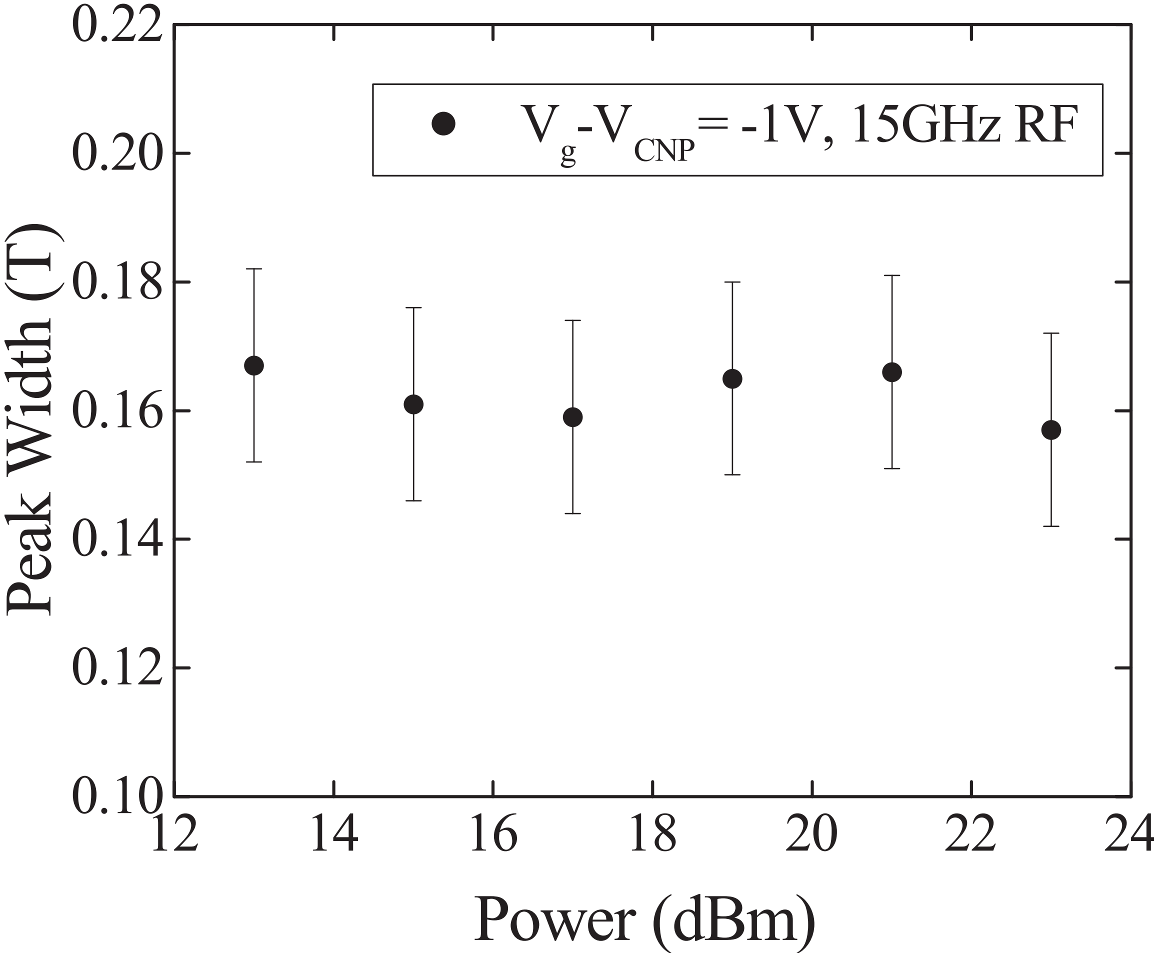

Figure 6-5: Peak widths for varying RF power but keeping back gate voltage and RF frequency constant, with $V_{\mathrm{g}} - V_{\mathrm{CNP}} = -1\,\mathrm{V}$ and $f = 15\,\mathrm{GHz}$. For powers under 13 dBm it was too difficult to separate the peaks from the noise to measure peak widths.

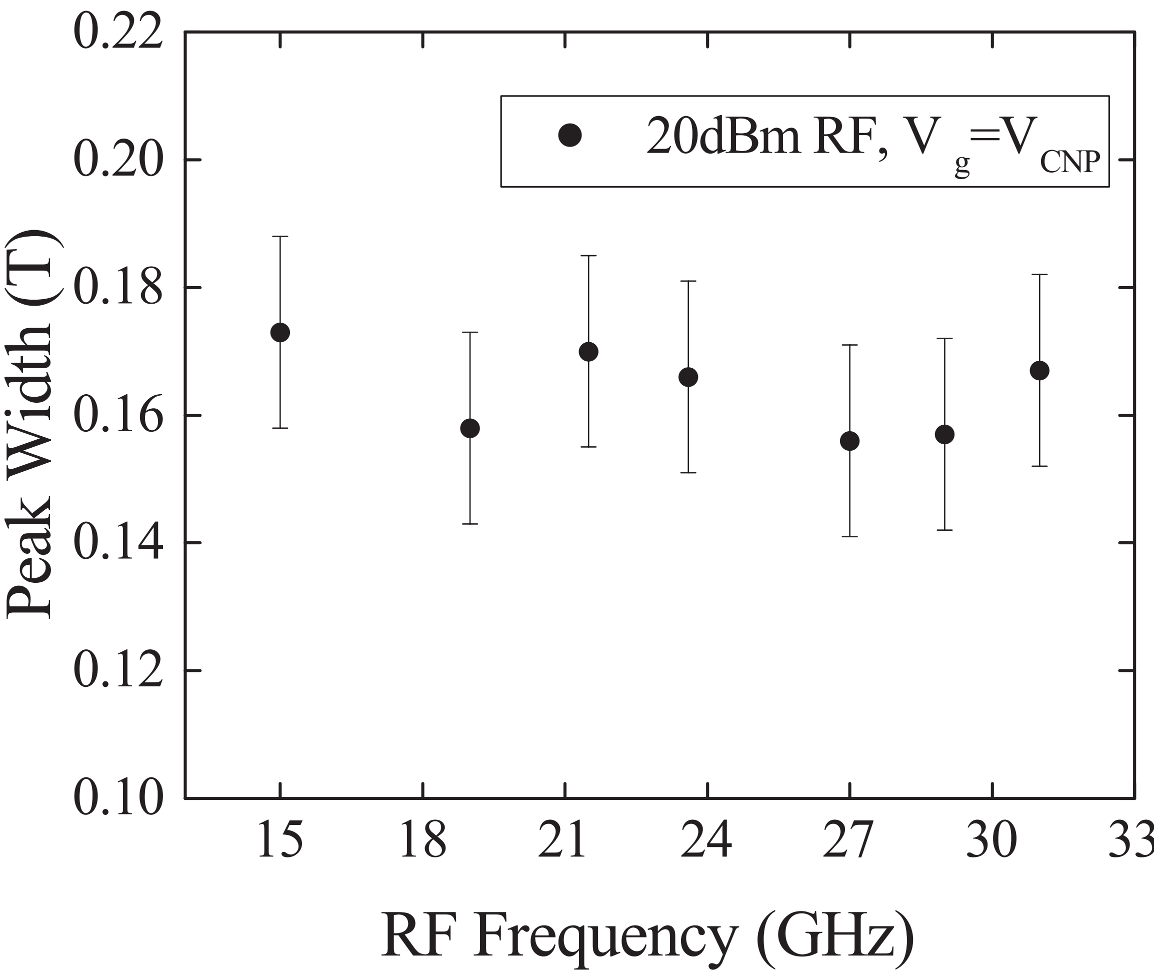

Figure 6-6: Peak widths for varying RF frequency but with constant RF power of 20 dBm and $V_{\mathrm{g}} = V_{\mathrm{CNP}}$.

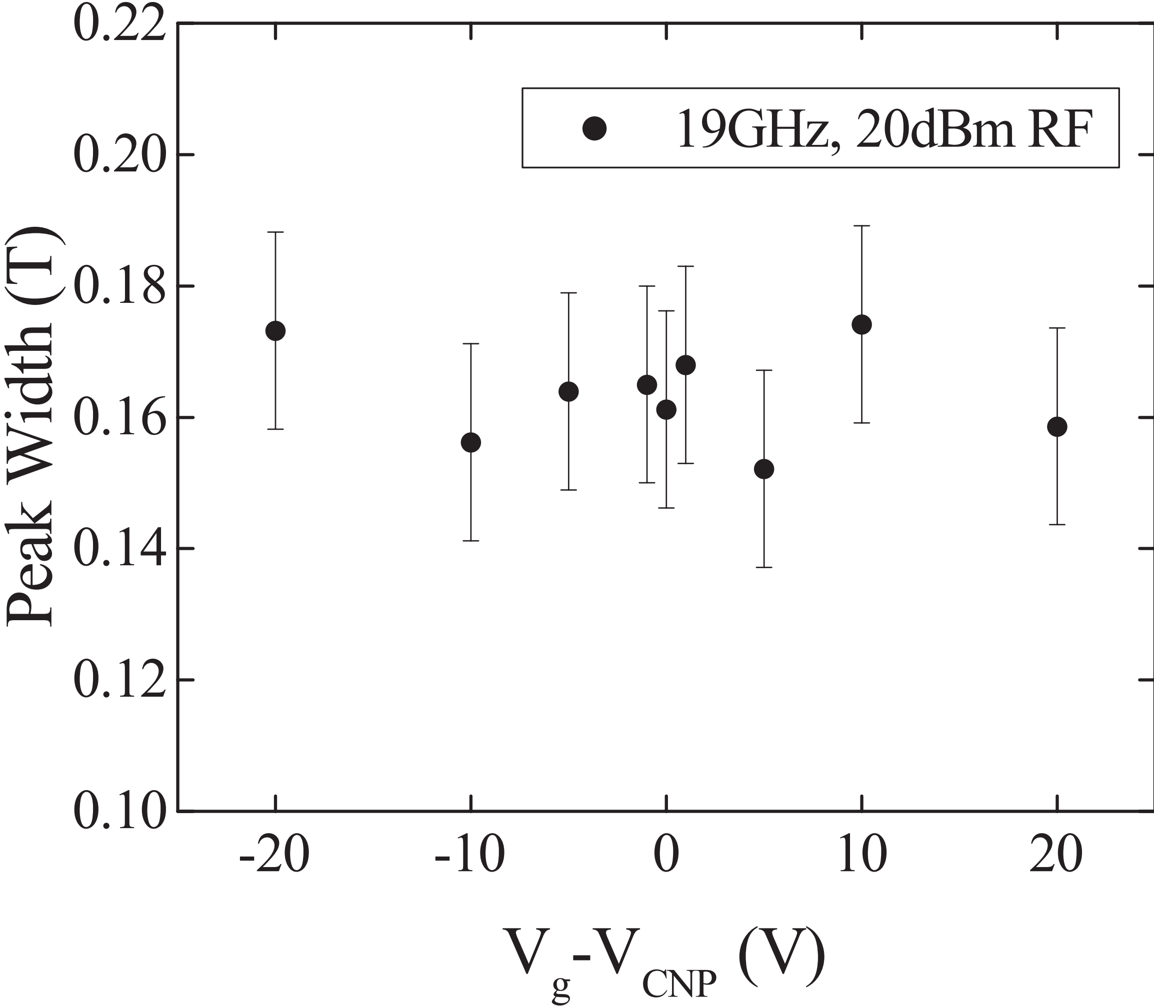

Figure 6-7: Peak widths for varying back gate voltage but keeping RF power and frequency constant at 20 dBm and 19 GHz.

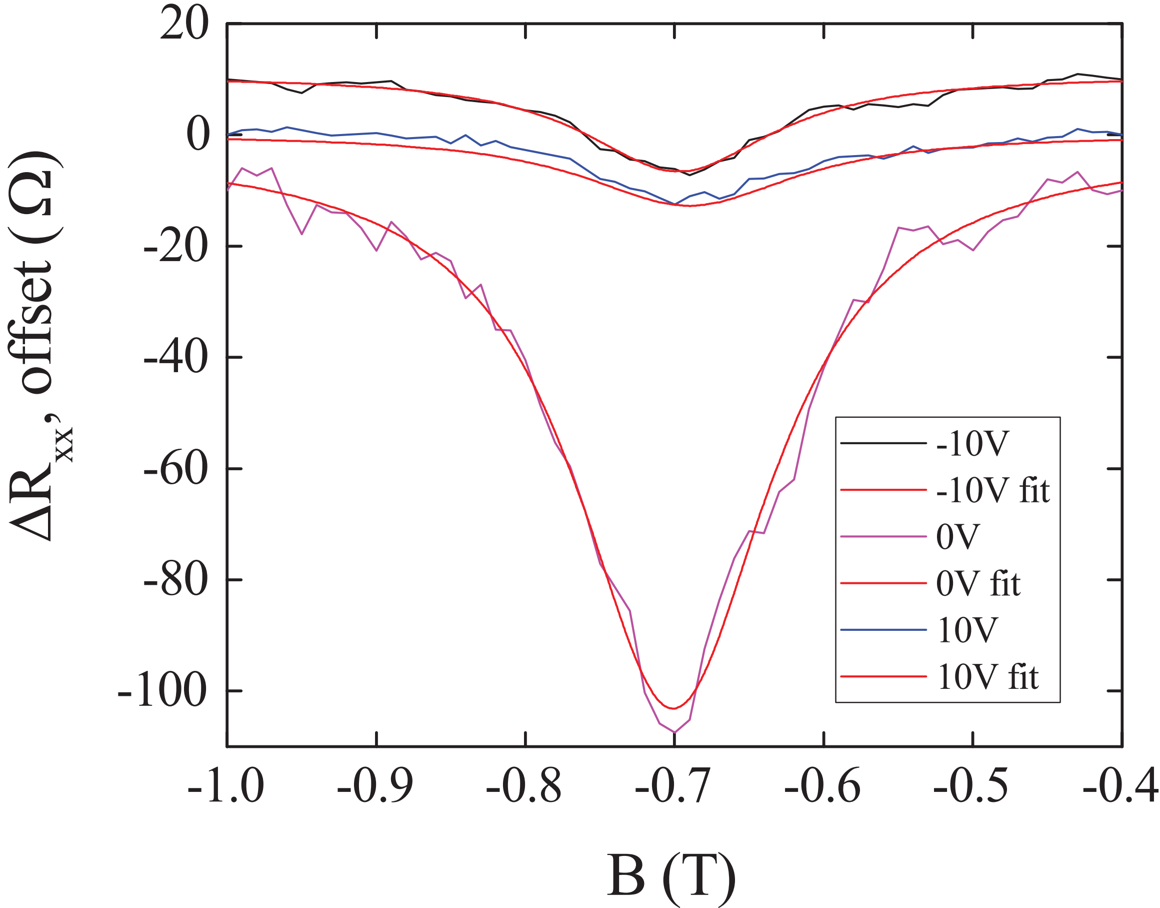

Figure 6-8: ESR peaks and Lorentzian fits after background removal for 19 GHz RF measurements at three different levels of back gate voltage ($V_g - V_{CNP}$). Peaks are separated by 10 Ω offsets for presentation.

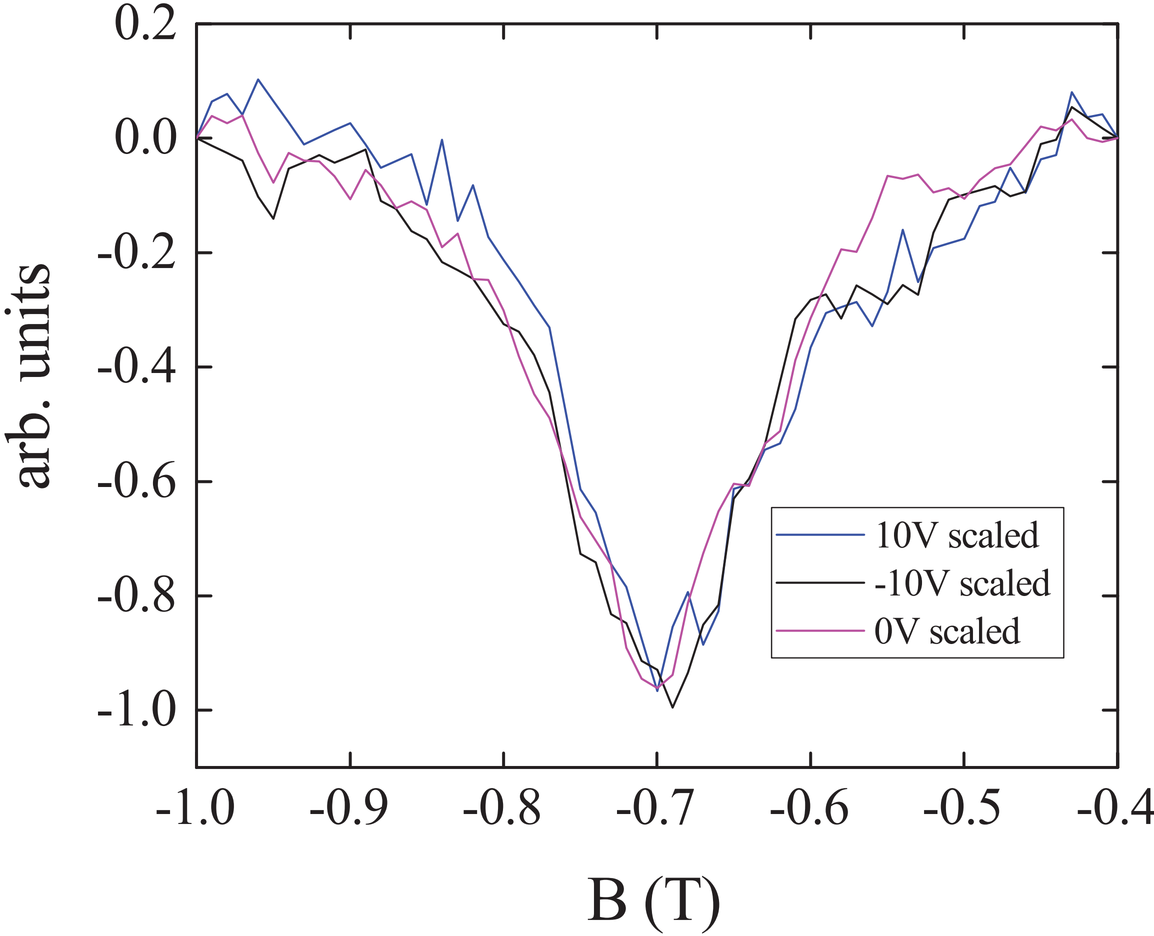

Figure 6-9: ESR peak heights from Fig. 6-8 normalized to arbitrary units and overlaid to emphasize the similarity of peak widths.

6.4 Further analysis

Invariance of the measurement values between substrates may be partially explained by the interaction parameter r_s (Eq. 2.30). Unlike other 2D systems without a linear dispersion relation, r_s for monolayer graphene is independent of charge carrier density, but it is still dependent on the relative permittivities of the materials on each side of the graphene sheet. When monolayer graphene is on SiO_2 with $\kappa_1 = 3.9$, $\kappa_2 = 1$ for vacuum, and $v_F = 1.1 \times 10^6\,\mathrm{m\,s^{-1}}$, results in $r_{s,SiO_2} \approx 0.8$. When SiC is the substrate, the Fermi velocity is about the same with $v_F = 1.15 \times 10^6\,\mathrm{m\,s^{-1}}$ [3], but the relative permittivity $\kappa_1 \approx 10$ is significantly larger. Putting all of this together in Eq. 2.30 leads to $r_{s,SiC} \approx 0.4$. Both substrates result in a value of $r_s < 1$, implying that the free charge carriers are weakly interacting in each experiment. Put another way, the electron-electron Coulomb interaction effects may be comparable in both systems, which may at least partially explain the similarity of the measured g-factors.

We stress that the sign of Δg does not change when transitioning from electrons to holes, as it would be expected, and that our value is very close to the one obtained previously by Mani *et al.* This finally suggests a more fundamental, intrinsic mechanism of spin relaxation, such as intrinsic spin-orbit coupling (SOC) [68], which is known to strongly influence the g-factor.

In summary, we have measured a resistively detected electron spin resonance in monolayer graphene. The associated absolute magnitude of the g-factor $\left|g_{\parallel}\right| = 1.952 \pm 0.002$ is independent of charge carrier type or density to within our experimental accuracy. Possible sources of the observed resonance include adsorbates and defects, with free charge carriers as the most likely cause. Discrepancies between the g-factors reported for free charge carriers in graphite and our measurements could be due to the unique electronic properties of monolayer graphene including a linear dispersion relation, substrate effects, and modified QED corrections. Additional theoretical analysis of the effective g-factor and electron spin resonance in monolayer graphene is needed to fully explain our results.

Chapter 7

Graphene on a periodic substrate

The graphene sample analyzed in this chapter was fabricated on a periodic SiO_2 substrate and an optical image is shown in Fig. 3-12. Etched trenches are 18 nm deep, 100 nm long, and are separated by mesas of 100 nm length. The deposited graphene mostly conforms to the surface but likely has suspended areas that connect the upper and lower stepped regions causing strain in the graphene. Graphene is known to produce pseudo-magnetic fields in excess of 300 T when under strain [82].

Electron spin resonance (ESR) measurements were performed on the mechanically modulated graphene sample, resulting in two sets of observed peaks. The first set is essentially the same as that discussed in the previous chapter and crosses the origin in the frequency vs. magnetic field plane. The second set of peaks has similar characteristics to the first, in that it is also linear in magnetic field and has the same slope, but crosses a non-zero frequency at zero magnetic field. This chapter reports these results and provides a possible explanation.

7.1 Secondary ESR peaks

As shown in Fig. 3-12, monolayer graphene was deposited on a SiO_2 substrate with a 200 nm period, with 100 nm mesas and valleys and 18 nm etch depth, then fabricated

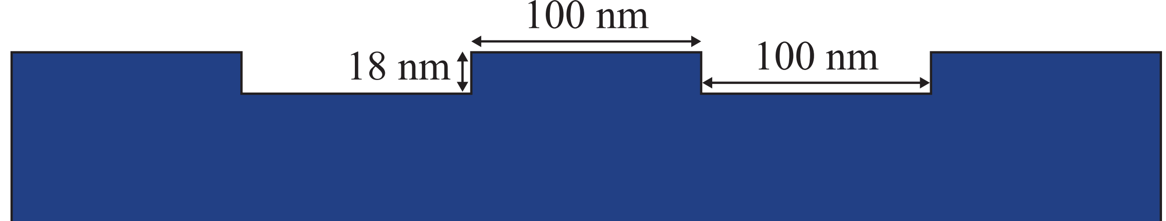

Figure 7-1: Pattern with 200 nm period etched on SiO_2 used in the ESR measurements described in this chapter. Graphene generally conforms to the surface after transfer but is under strain between the mesas and valleys, likely resulting in suspended areas that are not touching the substrate.

into a 200 µm × 22 µm Hall bar. ESR measurements were then performed in a similar manner to those described in Sec. 6.1 using the measurement setup presented in Ch. 4 at 4.2 K.

ESR measurements were made at frequencies from 0.5 GHz to 40 GHz in 0.5 GHz increments with the back gate $V_\mathrm{g} = 0$. A projection of the ESR signal amplitudes is shown in Fig. 7-2. As in Ch. 6, a line of peaks on each side of the origin traces back to the origin. These are the "primary" ESR peaks that correspond to spin splitting and have a compatible measurement to those measured for the flat Hall bar in the previous chapter, with $dF/dB = 27.3 \pm 0.2\,\mathrm{GHz T^{-1}}$ and $\left|g_\parallel\right| = 1.95 \pm 0.01$.

A "secondary" set of peaks give a more faint signal with a linear fit that traces back to 10.4 GHz at zero magnetic field. The linear curve fit for each set of peaks results in the same value of $\left|g_\parallel\right| = 1.95 \pm 0.01$. The zero field intercept is equivalent to

$$\begin{aligned} &10.4\,\mathrm{GHz} \times h = 43.0\,\mu\mathrm{eV}, \\ &\frac{43.0\,\mu\mathrm{eV}}{\mu_\mathrm{B}} = 0.74\,\mathrm{T}, \text{ and} \\ &\frac{43.0\,\mu\mathrm{eV}}{k_\mathrm{B}} = 0.50\,\mathrm{K}. \end{aligned} \tag{7.1}$$

Mani *et al.* [95] observed similar peaks with a zero field intercept at 10.76 GHz when measuring flat graphene at a temperature of 1.5 K. The secondary peaks observed by Mani were ascribed to pseudospin splitting, though there was little theoretical

background for this assertion. Our sample, however, showed the same peaks with a similar intercept when performed with mechanically modulated graphene and a significantly higher temperature of 4.2 K, much higher than the temperature of 0.5 K shown above. This is particularly interesting because one might expect thermal broadening to cause these peaks to be unobservable at such a high temperature.

7.2 Background

The picture of graphene used up until this point states that the conduction and valence bands of graphene are degenerate, and thus, at zero field one would expect two-fold degeneracy from both spin and pseudospin. However, Fig. 7-2 and 7-3 suggest that this four-fold degeneracy is completely broken at finite field. Spin splitting is expected, but the origin of the pseudospin splitting must be investigated.

A weak localization (WL) peak occurs in all of our samples, which directly reflects the degree of the valley (or pseudospin) symmetry breaking, according to McCann *et al.* [98]. WL requires intervalley scattering, as noted in Sec. 2.2.4, which is consistent with valley mixing, which lifts valley degeneracy.

The strength of intrinsic spin-orbit coupling (SOC) in graphene had been first calculated by multiple different groups to be on the order of $2\lambda_I = 1\,\mu\text{eV}$ [100, 171, 59], though they were all found to be incorrect. A more accurate picture was later determined using first principles calculations that included the effects of *d*-orbitals [44, 76] that resulted in an estimated zero-field splitting due to intrinsic SOC of 24 µeV. The four-fold degeneracy normally seen in graphene is not broken by intrinsic SOC but is instead only broken due to intrinsic bending by *d*-orbitals, which preserves time-reversal and space inversion symmetry. An electric field from sources such as a back gate or even a gauge field induced by strain [47] breaks space inversion symmetry further, resulting in a Rashba-like field of roughly $10\,\mu\text{eV}\,\text{nm}\,\text{V}^{-1}$. We can estimate a gate-induced field to be ~10 µeV by assuming a field of $1\,\text{V}\,\text{nm}^{-1}$ due to one electron

charge that is 1 nm away from the graphene sheet.

In addition to applied fields, ripples in the graphene sheet itself can induce extrinsic SOC. Gmitra *et al.* shows that this additional splitting increases roughly quadratically with the relative corrugation strain of the ripples. The energy extrapolated from the secondary ESR peaks shown in Fig. 7-2 and 7-3, 43 µeV, is of the same order of magnitude that would be expected when combining the effects of intrinsic and extrinsic SOC described above.

7.3 Hamiltonian

Here we will derive the Hamiltonian for the charge carriers in a basis that includes real spin and pseudospin. This Hamiltonian incorporates terms for the effects of intrinsic spin-orbit coupling (SOC) as well as extrinsic SOC induced by applying a field from an external source such as a back gate or strain. We will show how the band structure changes with adjustment of the Hamiltonian parameters and how the different cases relate to our observed measurements.

The basis with both real spin and pseudospin, where $\{\uparrow,\downarrow\}$ denotes the real spin and $\left\{\phi^{\mathrm{A}},\phi^{\mathrm{B}}\right\}$ is the occupation of sites on the A or B sublattices, is represented as

$$\{\uparrow,\downarrow\}\otimes\left\{\phi^{\mathrm{A}},\phi^{\mathrm{B}}\right\}\equiv\left\{\phi^{\mathrm{A}}_{\uparrow},\phi^{\mathrm{B}}_{\uparrow},\phi^{\mathrm{A}}_{\downarrow},\phi^{\mathrm{B}}_{\downarrow}\right\}. \tag{7.2}$$

Around the $\boldsymbol{K}$ point, we represent the Hamiltonian as

$$\hat{H}^0_q\cong\hbar v_{\mathrm{F}}\hat{I}\otimes\left(\hat{\sigma}_x\hat{q}_x+\hat{\sigma}_y\hat{q}_y\right)=\begin{pmatrix}0&\alpha^*&0&0\\\alpha&0&0&0\\0&0&0&\alpha^*\\0&0&\alpha&0\end{pmatrix} \tag{7.3}$$

where $\hat{I}$ is the 2×2 identity matrix, $\alpha=\hbar v_{\mathrm{F}}|q|\mathrm{e}^{-i\theta_q}$, and $\theta_q=\arctan\left(\frac{q_y}{q_x}\right)$. These are

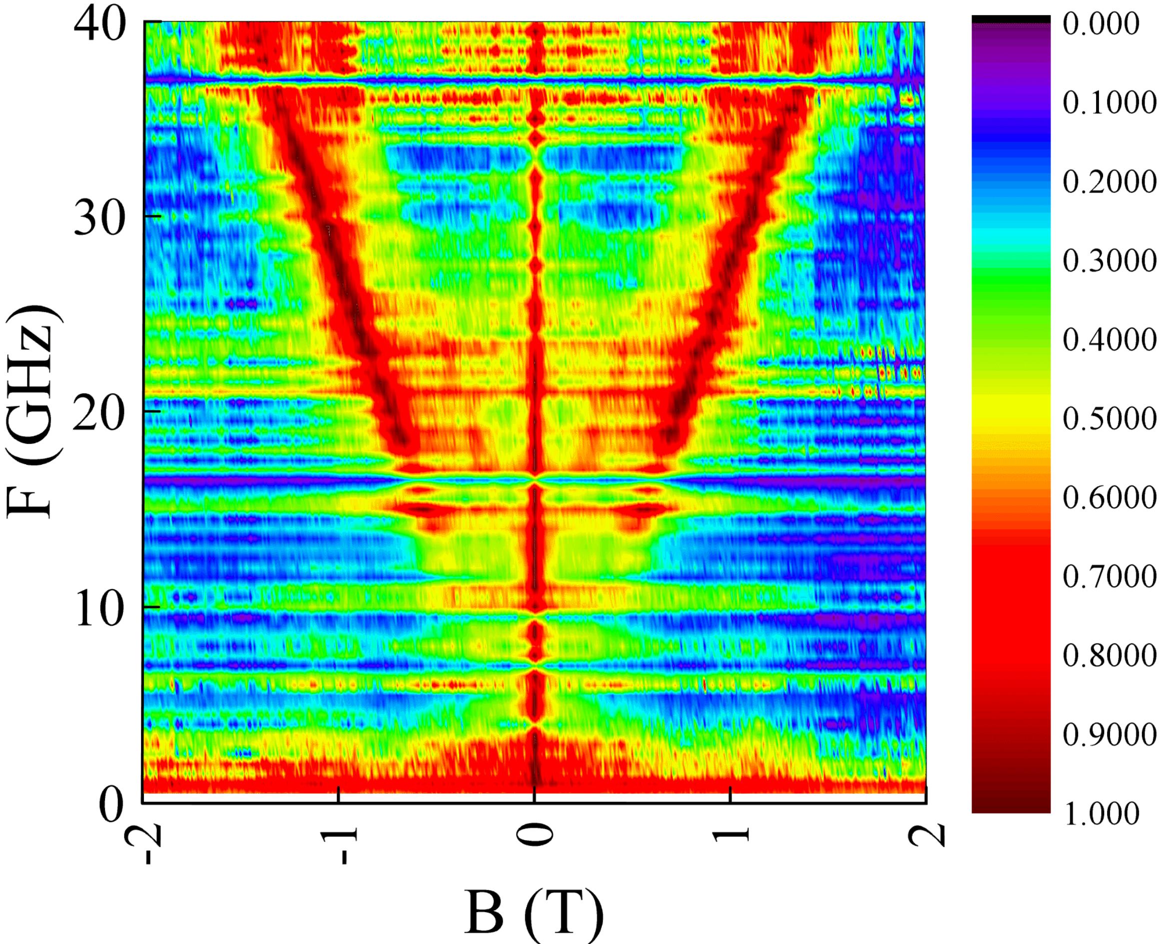

Figure 7-2: This is a projection of a three-dimensional graph displaying the ESR signal amplitudes of measurements at frequencies from 0.5 GHz to 40 GHz in 0.5 GHz increments. The ESR peaks from Ch. 6 reappear and a second set of peaks, which may indicate the breaking of spin and pseudospin degeneracy, is also evident. (Measurement taken by J. Sichau in R. Blick's group.)

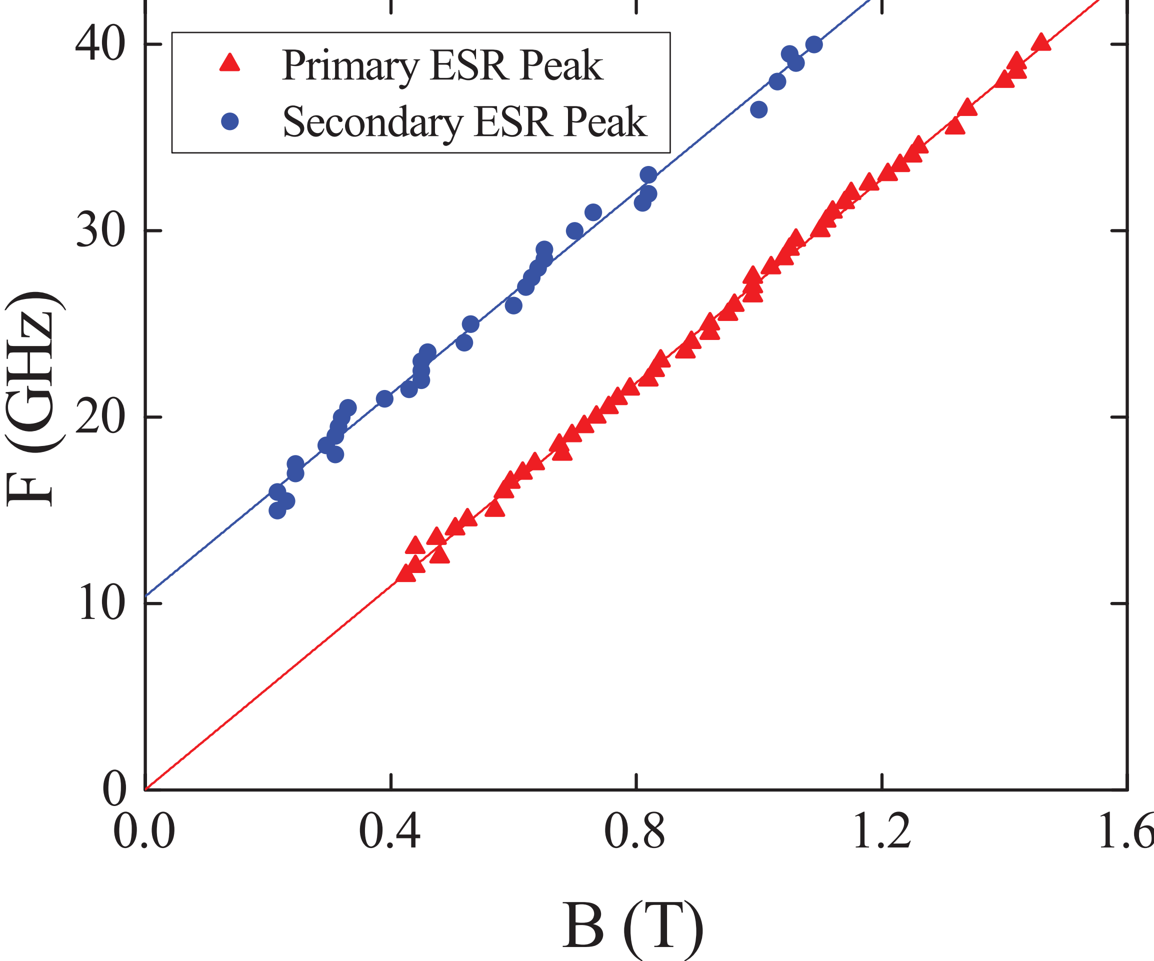

Figure 7-3: Spin (primary) and pseudospin (secondary) ESR peaks at many frequencies ranging up to 40 GHz with linear fits. Linear fits on each set of peaks result in the same slope and are offset by 10.4 GHz.

the Dirac cones, as seen in Fig. 7-4(a), which are linear in momentum and cross at $q = 0$ because they have a different pseudospin. We then add a term for the intrinsic spin-orbit Hamiltonian, which is present due to the d-orbitals [68, 44],

$$\hat{H}^{\mathrm{I}}_{\mathrm{SO}} = \lambda_{\mathrm{I}} \hat{s}_z \otimes \hat{\sigma}_z = \lambda_{\mathrm{I}} \begin{pmatrix} 1 & 0 & 0 & 0 \\ 0 & -1 & 0 & 0 \\ 0 & 0 & -1 & 0 \\ 0 & 0 & 0 & 1 \end{pmatrix} \tag{7.4}$$

where $\hat{s}_{\mathrm{z}}$ acts on spin and $\hat{\sigma}_{\mathrm{z}}$ on pseudospin. The total Hamiltonian so far is

$$\hat{H} = \hat{H}^0_q + \hat{H}^{\mathrm{I}}_{\mathrm{SO}} = \begin{pmatrix} \lambda_{\mathrm{I}} & \alpha^* & 0 & 0 \\ \alpha & -\lambda_{\mathrm{I}} & 0 & 0 \\ 0 & 0 & -\lambda_{\mathrm{I}} & \alpha^* \\ 0 & 0 & \alpha & \lambda_{\mathrm{I}} \end{pmatrix} \tag{7.5}$$

which is shown in Fig. 7-4(b). The Dirac cones are shifted at $q = 0$ causing a gap, $2\lambda_{\mathrm{I}}$, which is ~24 µeV [44] or about 5.8 GHz. The eigenvalues for the conduction (+) and valence (−) bands are then

$$\varepsilon_{\mathrm{c,v}} = \pm\sqrt{|\alpha|^2 + \lambda_{\mathrm{I}}^2}, \tag{7.6}$$

and these values are four-fold degenerate as time reversal and inversion symmetry are not broken by $\hat{H}^{\mathrm{I}}_{\mathrm{SO}}$ in the absence of a magnetic field.

An external electric field breaks space inversion further [44] with the new term written as

$$\hat{H}^{\mathrm{E}}_{\mathrm{SO}} = \lambda_{\mathrm{B}} \hat{s}_y \otimes \hat{\sigma}_x = \lambda_{\mathrm{B}} \begin{pmatrix} 0 & 0 & 0 & -\mathrm{i} \\ 0 & 0 & -\mathrm{i} & 0 \\ 0 & \mathrm{i} & 0 & 0 \\ \mathrm{i} & 0 & 0 & 0 \end{pmatrix} \tag{7.7}$$

and when added to the previously defined terms results in

$$\hat{H} = \hat{H}_q^0 + \hat{H}_{\mathrm{SO}}^{\mathrm{I}} + \hat{H}_{\mathrm{SO}}^{\mathrm{E}} = \begin{pmatrix} \lambda_{\mathrm{I}} & \alpha^* & 0 & -\mathrm{i}\lambda_{\mathrm{B}} \\ \alpha & -\lambda_{\mathrm{I}} & -\mathrm{i}\lambda_{\mathrm{B}} & 0 \\ 0 & \mathrm{i}\lambda_{\mathrm{B}} & -\lambda_{\mathrm{I}} & \alpha^* \\ \mathrm{i}\lambda_{\mathrm{B}} & 0 & \alpha & \lambda_{\mathrm{I}} \end{pmatrix}. \tag{7.8}$$

The eigenvalues at the Dirac points ($\alpha = 0$) are

$$\begin{aligned} \varepsilon_{0,1} &= -\lambda_{\mathrm{I}} \pm \lambda_{\mathrm{B}} \\ \varepsilon_{2,3} &= \lambda_{\mathrm{I}} \pm \lambda_{\mathrm{B}} \end{aligned} \tag{7.9}$$

where the bands of Fig. 7-4(b) are split into two sets of states, as shown in Fig. 7-4(c). However, when $\lambda_{\mathrm{I}} = \lambda_{\mathrm{B}}$ as in Fig. 7-4(d), the gap between the green bands disappears, recovering a pair of Dirac cones and re-establishing a double-degeneracy at $q = 0$. These states cross because they have different eigenvalues for real spin, +1 and -1. At $q = 0$ ($\alpha = 0$), the eigenstates are:

$$\begin{aligned} \Phi^0 &= \frac{1}{\sqrt{2}}[\phi_{\downarrow}^{\mathrm{A}} + i\phi_{\uparrow}^{\mathrm{B}}], \\ \Phi^1 &= \frac{1}{\sqrt{2}}[\phi_{\uparrow}^{\mathrm{A}} + i\phi_{\downarrow}^{\mathrm{B}}], \\ \Phi^2 &= \frac{1}{\sqrt{2}}[\mathrm{i}\phi_{\downarrow}^{\mathrm{A}} + \phi_{\uparrow}^{\mathrm{B}}], \\ \Phi^3 &= \frac{1}{\sqrt{2}}[\mathrm{i}\phi_{\uparrow}^{\mathrm{A}} + \phi_{\downarrow}^{\mathrm{B}}]. \end{aligned} \tag{7.10}$$

7.4 Analysis

Finally, we will give a possible theoretical explanation for our observations. In our sample, λ_{B} is a function of the electric field that is adjusted by the back gate and increases or decreases the splitting while λ_{I} does not vary with the gate. A dip in

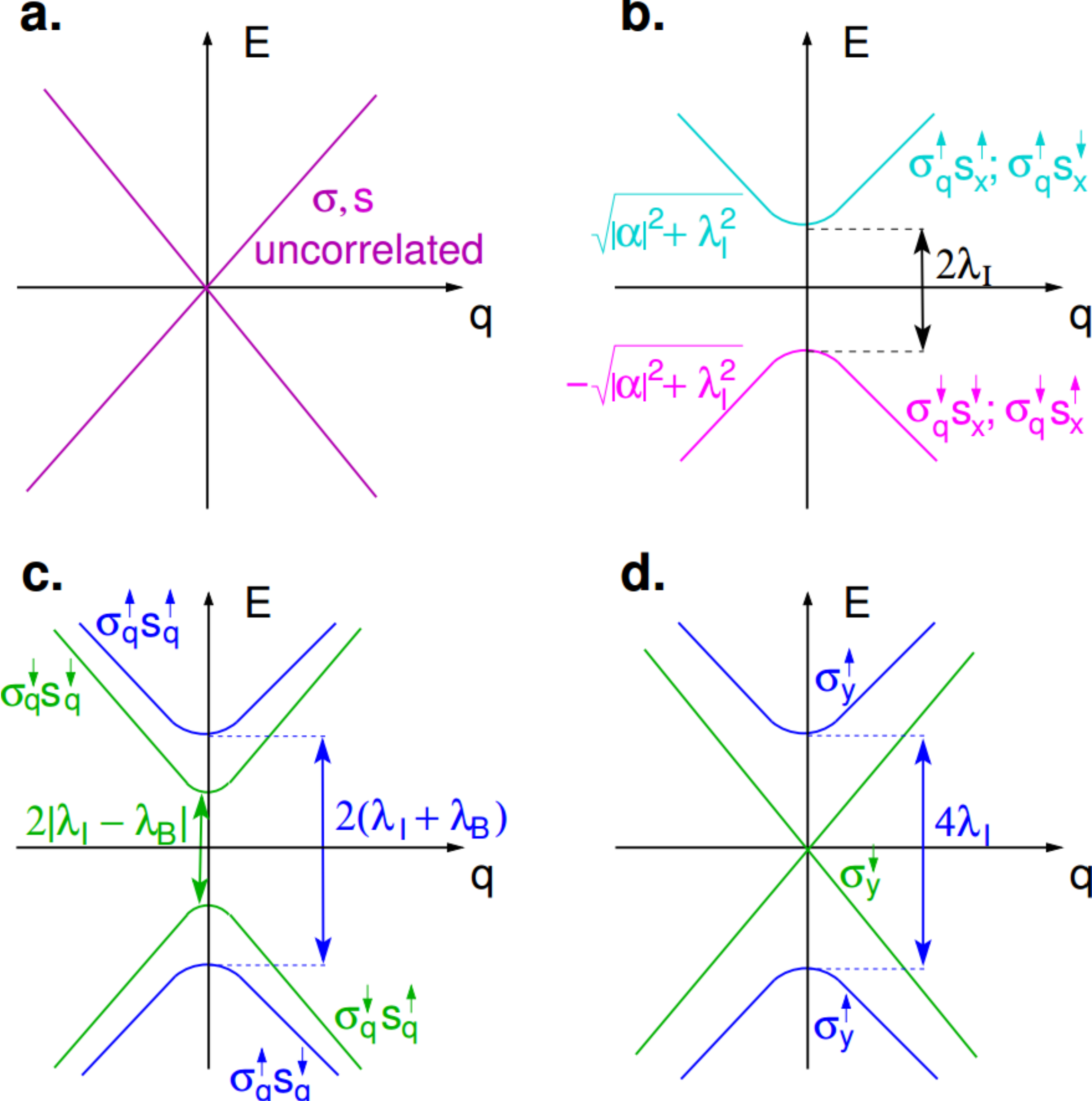

Figure 7-4: Schematic representation of the band structure of graphene (a) with no spin-orbit coupling, (b) with intrinsic SO with the parameter λ_{I}, (c) extrinsic SO, represented by λ_{B}, in addition to intrinsic SO, and (d) with both extrinsic and intrinsic SO and $\lambda_{\mathrm{I}} = \lambda_{\mathrm{B}}$, restoring one of the Dirac cones. (Simulation results by M. Prada in D. Pfannkuche's group.)

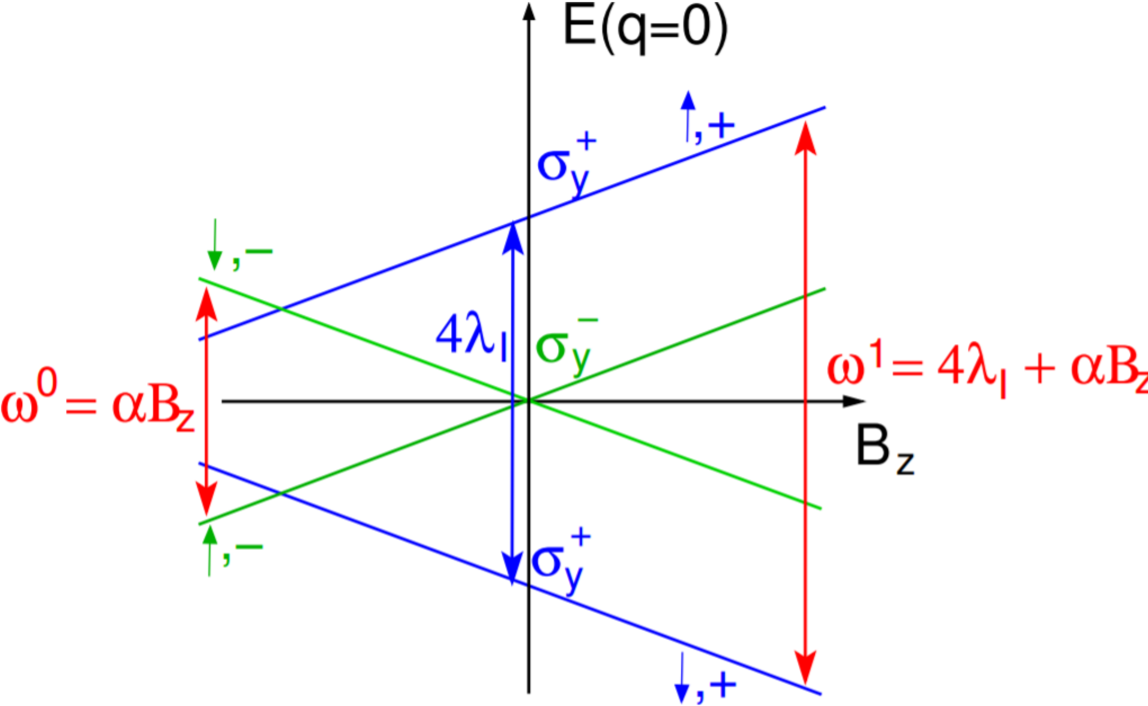

Figure 7-5: Schematic representation of the splitting of the bands at $q = 0$ by a magnetic field under the assumption the band structure in Fig. 7-4(d). Possible photo-induced transitions would require $\Delta s = 1$ (real spin) and $\Delta\sigma = 0$ (pseudospin). The latter condition implies that a transition between curves of different colors is not possible due to pseudospin conservation. (Simulation results by M. Prada in D. Pfannkuche's group.)

the density of states will occur exactly when the condition $\lambda_{\mathrm{B}} = \lambda_{\mathrm{I}}$ is met: this is the point that gives a splitting of blue bands of exactly $4\lambda_{\mathrm{I}}$ while the green lines are still doubly degenerate. The blue bands can thus be coupled by a photon in ESR experiments even in the absence of a magnetic field resulting in an expected zero-field splitting of $4\lambda_{\mathrm{I}}$.

Applying an external magnetic field causes the bands that cross at $q = 0$ (green bands of Fig. 7-4(c) and (d)) to split in two while the blue bands shift in energy. A depiction of this effect is shown in Fig. 7-5. The first set of ESR peaks would be explained by Zeeman splitting, with $\hbar\omega^0 = g\mu_{\mathrm{B}}B$, and the second set of peaks would be shifted by $4\lambda_{\mathrm{I}}$, so that $\hbar\omega^1 = g\mu_{\mathrm{B}}B + 4\lambda_{\mathrm{I}}$, about 11.6 GHz. In Fig. 7-5, the former case corresponds to the spin splitting of the green lines with $\hbar\omega^0$, and the latter case to the spin splitting between the two blue bands with $\hbar\omega^0 + 4\lambda_{\mathrm{I}}$. The blue and green bands can not couple together in ESR experiments because otherwise pseudospin would not be conserved. Photons are able to couple different real spin states but not different pseudospin states. Real spin conservation requires $\Delta s = 1$, with s denoting real spin, as the spin of the photon is one. In addition, pseudospin conservation requires that $\Delta\sigma = 0$, where σ is pseudospin. Without this condition, another set of peaks would be observed.

Of the presented band structures, Fig. 7-4(d) looks closest to the situation that we are observing and is also the most similar to a Dirac structure as it corresponds to the gate voltage set such that it minimizes the density of states. We can expect a similar situation to the work of Mani *et al.*, which resulted in similar zero-field splitting. Once the Dirac point is reached, the distance to the second peak is $4\lambda_{\mathrm{I}}$, which would explain why both measurements have similar results. However, each measurement varies from the expected value by ~1 GHz. There are several possible explanations for this discrepancy. First, we may have a situation closer to 7-4(c), with $\lambda_{\mathrm{B}} = \lambda_{\mathrm{I}} + 0.5\,\mathrm{GHz}$. Second, in-plane magnetization due to the graphene ripples may give a significant correction. Third, the measurement error bars may, in reality, be

large enough to encompass the theoretical result. The final possibility is that the theoretical first principle calculations quoted above are missing something and need to be reworked to obtain a more accurate value.

Further measurements of this sample at different gate voltages are planned. Moreover, a theoretical analysis of spin-orbit interactions and their effects on the g-factor of graphene is currently underway and will be included in a future publication.

Chapter 8

Conclusions and outlook

The sample fabrication procedures presented here result in large-area graphene devices of high quality. The 2-step lift-off aids greatly in producing unbroken large graphene structures, and the 2-step annealing process, as well as other cleaning steps, result in a realization of near-ideal mobilities, low hysteresis, and an observation of quantum Hall levels. The samples fabricated for this work used Si/SiO_2 substrates, though our methods also allow graphene transfer to many other types of substrates. Hence, our processing approach enables large-scale integration of high-quality graphene layers in devices such as THz-emitters, thermo-power couplers, and possibly flexible thin-film sensors.

We also measured a resistively detected electron spin resonance (ESR) in flat monolayer graphene. Surprisingly, the magnetic moment and associated g-factor $\left|g_{\parallel}\right| = 1.952 \pm 0.002$ was found to be insensitive to charge carrier type, density, or mobility to within our experimental accuracy, leading to a g-factor shift relative to the free-electron value of $\Delta g \simeq -0.05$. After analyzing a number of candidates for the cause of the observed resonance peaks including adsorbates and defects, free charge carriers were determined to be the origin of the measured ESR signals. Also, spin relaxation times calculated from these measurements have no significant dependence on charge carrier density, RF power, or RF frequency and were found to be $\tau_s \approx (40 \pm 6)$ ps.

Measurements of a mechanically modulated graphene sample showed two sets of ESR peaks; the first set is identical to the peaks found in the flat sample and the second is attributed to pseudospin splitting. A possible explanation for the physical origin of the zero-field splitting that takes into account the band structure of graphene and incorporates the roles of intrinsic and extrinsic spin-orbit coupling (SOC) was presented. In previous work, SOC in graphene has been modeled in the presence of orbitals with d-symmetry [44, 76]. These first-principles calculations have estimated the intrinsic SOC zero-field splitting to be as large as several $10\,\mu\text{eV}$ while the energy dispersion very close to the K-point remains linear. The magnitude of the SOC may, therefore, account for the g-factor and its behavior that we have determined experimentally. As demonstrated by Kane & Mele [68], renormalization group calculations yield an enhancement of the intrinsic SOC potential by an order of magnitude. Hence, our results support a similar intrinsic enhancement in graphene. A more detailed theoretical analysis of the observed value of Δg that includes the effects of SOC and electron-electron interactions is currently underway.

In order to further explore the g-factor of graphene, it would be useful to perform measurements with various substrates, especially those that result in a Wigner-Seitz radius (r_s, Eq. 2.30) greater than one. Experiments with graphene on a substrate that has $\kappa \lesssim 3$ and is measured in vacuum or a helium atmosphere would result in $r_\text{s} \gtrsim 1$ and allow greater understanding of the influence of electron-electron Coulomb interaction effects on the g-factor. Suspended graphene provides an upper bound with $r_\text{s} = 2.2$, but a polytetrafluoroethylene (PTFE) substrate may be a good candidate for future experiments since $\kappa_\text{PTFE} = 2.1$ would result in $r_\text{s,PTFE} \approx 1.3$ in our measurement setup. In addition, PTFE is a substrate to which graphene can be readily transferred [96].

The work presented in this thesis has revealed unanticipated properties of graphene and investigated their origins. It is likely that studies of graphene will reveal new and interesting physics for years to come.

Appendix A

Sample preparation recipes

A.1 Graphene preparation

A.1.1 Coat with PMMA

- Cut a piece of monolayer graphene on copper foil that will fit on a flat spinner chuck
- Tape over vacuum hole in spinner using scotch tape
- Place piece of copper foil on chuck, graphene side up, and tape it down on all sides with multiple layers and no gaps while minimizing graphene coverage
- Coat with “Microchem PMMA 950K A 4” and spin at 6,000 RPM for 1 min
- Remove tape
- Cut into pieces appropriate for sample size

A.1.2 Copper removal and cleaning

- Mix a solution of iron(III) nitrate or iron(III) chloride with water, $0.05\,\mathrm{g\,mL^{-1}}$

- Place a stack of PMMA/graphene/copper on top of etching solution, PMMA side up
- Wait at least 6 h, preferably overnight
- 3x: Move PMMA/graphene stack to clean deionized (DI) water, wait 20 min
- Prepare a solution of 100 mL DI water, 5 mL 32% HCl, and 4 mL H_2O_2 30%
- Place PMMA/graphene stack on HCl mixture for 15 min, PMMA side up
- 2x: Move PMMA/graphene stack to clean DI water, wait 30 min
- Prepare solution of 100 mL DI water, 1 mL NH_4OH, and 1 mL H_2O_2 30%
- Place PMMA/graphene stack in ammonia mixture for 3 min, PMMA side up
- 2x: Move PMMA/graphene stack to clean DI water, wait 30 min

A.2 Transferring graphene

A.2.1 Substrate preparation

- Cut pieces of a wafer into approximately 1 cm^2 pieces
- Hold the polished side of the wafer firmly down on cleanroom wipes and scratch the back with a diamond scribe, then snap the wafer by gently applying pressure
- Blow off dust with N_2 gun
- Remove remaining contaminants by sonicating in acetone and then in isopropanol for one minute each, then blow dry with N_2

A.2.2 Move to substrate

- Heat up convection oven to 150 °C
- For SiO_2 substrate, place in O_2 plasma asher at 300 W for 4 min
- Within one minute of opening asher, use wafer tweezers to scoop up the graphene floating on the water
- Place sample in petri dish and bake in oven for 15 min
- Cool to room temperature

A.2.3 PMMA Removal

- Place in acetic acid overnight (assuming SiO_2)
- Rince in isopropanol for 2 min
- Dry with N_2 gun

A.3 Photolithography

A.3.1 Metal contacts

- Spin on MicroChem LOR 5A at 6,000 RPM, maximum acceleration, for 1 min
- Bake at 160 °C for 1 min, air cool for 5 min
- Spin on Microposit S1805 at 6,000 RPM, maximum acceleration, for 1 min
- Bake at 115 °C for 1 min, air cool for 5 min
- Expose 2.2 s with 365 nm light at 25 W cm^{-2} (assuming SiO_2)
- Develop in Microposit MF 319 for 45 s

- Rinse in DI water for 60 s
- Dry with N_2 gun

A.3.2 Contact deposit and lift-off

- Deposit 5 nm of nickel and 50 nm of gold with physical vapor deposition (PVD)
- Place in acetone for 1 h
- Squeeze plastic pipette to gently flow acetone over the sample and remove excess metal
- Repeat previous step in two different beakers
- Place in Microposit Remover 1165 for 30 min
- Rinse in isopropanol for 60 s
- Rinse in DI water
- Dry with N_2 gun

A.3.3 Hall bar

- Spin on Microposit S1813 at 6,000 RPM, maximum acceleration, for 1 min
- Bake at 115 °C for 1 min, air cool for 5 min
- Expose 4.2 s with 365 nm light at 25 W cm^{-2} (assuming SiO_2)
- Develop in Microposit MF 319 for 45 s
- Rinse in DI water for 60 s
- Dry with N_2 gun

- Place on bottom of asher, apply O_2 plasma with asher for 4 min at 300 W
- Soak in acetone for 5 min
- Rinse in isopropanol
- Dry with N_2 gun

A.4 E-beam lithography

A.4.1 Alignment markers

- Use recipe for photolithography recipe for metal contacts to define area for alignment markers
- Use sputterer to deposit 40 nm of AuPd
- Lift-off with sonication in acetone
- Rinse in isopropanol
- Dry with N_2 gun

A.4.2 E-beam lithography recipes

- Resist:MicroChem 950 PMMA A4, spin at 4,000 RPM, maximum acceleration, for 45 s
- Bake for 90 s at 180 °C
- Develop in Allresist AR 600-56 for 30-60 s, depending on beam dosage
- Rinse for 15 s in isopropanol
- Rinse for 30 s in DI water
- Dry with N_2 gun

A.5 Thermal annealing

- Bake in rapid thermal annealer under vacuum for 16 h at 140 °C
- Mount in cryostat probe, slide probe inside tube oven
- Bake sample in-situ under vacuum at 140 °C until bar resistance stops changing

Appendix B

List of samples

Table B.1: List of samples

Name	Photo	Structure	Comments
1.92 mm Flat		1.92 mm×64 µm graphene on flat SiO_2/Si substrate	Proof of concept for ultra-large graphene device
200 µm Flat		200 µm×22 µm graphene on flat SiO_2/Si substrate	Characterized in Ch. 5, ESR measurements in Ch. 6
200 nm Period		200 µm×22 µm graphene on etched SiO_2/Si substrate with trenches of 100 nm length and 18 nm depth between 100 nm mesas	ESR measurements in Ch. 7
4 µm Period		Etched SiO_2/Si substrate with 198 nm deep trenches of 2 µm length between 2 µm mesas	Test for deposition of large-area graphene onto etched periodic pattern

Appendix C

Lists of symbols

Table C.1: Physical constants

Physical constant	Symbol	Value
Bohr magneton	$\mu_\mathrm{B} = e\,\hbar/\,(2m_\mathrm{e})$	$9.274\,010 \times 10^{-34}\,\mathrm{J\,T^{-1}}$
Boltzmann constant	k_B	$1.380\,649 \times 10^{-23}\,\mathrm{J\,K^{-1}}$
Dirac flux quantum	$\phi_0 = h/e$	$4.135\,668 \times 10^{-15}\,\mathrm{Wb}$
Electron mass	m_e	$9.109\,384 \times 10^{-31}\,\mathrm{kg}$
Elementary charge	e	$1.602\,177 \times 10^{-19}\,\mathrm{C}$
Permeability of free space	μ_0	$4\pi \times 10^{-7}\,\mathrm{N\,A^{-2}}$
Permittivity of free space	ε_0	$8.854\,188 \times 10^{-12}\,\mathrm{F\,m^{-1}}$
Planck constant	h	$6.626\,070 \times 10^{-34}\,\mathrm{J\,s}$
Reduced Planck constant	$\hbar = h/\,(2\pi)$	$1.054\,572 \times 10^{-34}\,\mathrm{J\,s}$
Speed of light in vacuum	c_0	$2.997\,925 \times 10^{8}\,\mathrm{m\,s^{-1}}$

Table C.2: Abbreviations of common terms

Abbreviation or acronym	Explanation
2DEG	Two-dimensional electron gas
CNP	Charge neutral point
CVD	Chemical vapor deposition
DI	Deionized (water)
ESR	Electron spin resonance
IPA	Isopropanol or isopropyl alcohol
MIBK	Methyl isobutyl ketone
PMMA	Poly(methyl methacrylate)
RF	Radio frequency
RIE	Reactive ion etching
SdH	Shubnikov-de Haas
SdHO	Shubnikov-de Haas oscillations
SEM	Scanning electron microscope
SOC	Spin-orbit coupling
WAL	Weak anti-localization
WL	Weak localization

Bibliography

[1] Shaffique Adam, E.H. Hwang, V.M. Galitski, and S. Das Sarma. A self-consistent theory for graphene transport. *Proceedings of the National Academy of Sciences*, 104(47):18392–18397, 2007.

[2] Tsuneya Ando. Screening effect and impurity scattering in monolayer graphene. *Journal of the Physical Society of Japan*, 75(7):074716, 2006.

[3] Tahereh Nemati Aram and Asghar Asgari. Influence of Fermi velocity engineering on electronic and optical properties of graphene superlattices. *Physics Letters A*, 379(12):974–978, 2015.

[4] Dirk Backes, Richard Hall, Michael Pepper, Harvey Beere, David Ritchie, and Vijay Narayan. Observation of geometry-dependent conductivity in two-dimensional electron systems. *Physical Review B*, 92(23):235427, 2015.

[5] Luca Banszerus, Michael Schmitz, Stephan Engels, Jan Dauber, Martin Oellers, Federica Haupt, Kenji Watanabe, Takashi Taniguchi, Bernd Beschoten, and Christoph Stampfer. Ultrahigh-mobility graphene devices from chemical vapor deposition on reusable copper. *Science Advances*, 1(6):e1500222, 2015.

[6] Amelia Barreiro, Felix Börrnert, Stanislav M. Avdoshenko, Bernd Rellinghaus, Gianaurelio Cuniberti, Mark H. Rümmeli, and Lieven M.K. Vandersypen. Understanding the catalyst-free transformation of amorphous carbon into graphene by current-induced annealing. *Scientific Reports*, 3, 2013.

[7] C.W.J. Beenakker and Henk van Houten. Quantum transport in semiconductor nanostructures. *Solid State Physics*, 44(1):228, 1991.

[8] Claire Berger, Zhimin Song, Tianbo Li, Xuebin Li, Asmerom Y. Ogbazghi, Rui Feng, Zhenting Dai, Alexei N. Marchenkov, Edward H. Conrad, Phillip N. First, and Walt A. de Heer. Ultrathin epitaxial graphite: 2D electron gas properties and a route toward graphene-based nanoelectronics. *The Journal of Physical Chemistry B*, 108(52):19912–19916, 2004.

[9] Claire Berger, Zhimin Song, Xuebin Li, Xiaosong Wu, Nate Brown, Cécile Naud, Didier Mayou, Tianbo Li, Joanna Hass, Alexei N. Marchenkov, Edward H.

Conrad, Phillip N. First, and Walt A. de Heer. Electronic confinement and coherence in patterned epitaxial graphene. *Science*, 312(5777):1191–1196, 2006.

[10] K.I. Bolotin, K.J. Sikes, J. Hone, H.L. Stormer, and P. Kim. Temperature-dependent transport in suspended graphene. *Physical Review Letters*, 101(9):096802, 2008.

[11] Kirill I. Bolotin, K.J. Sikes, Z. Jiang, M. Klima, G. Fudenberg, J. Hone, P. Kim, and H.L. Stormer. Ultrahigh electron mobility in suspended graphene. *Solid State Communications*, 146(9):351–355, 2008.

[12] Péter Boross, Dóra, Balázs, Annamária Kiss, and Ferenc Simon. A unified theory of spin-relaxation due to spin-orbit coupling in metals and semiconductors. *Scientific Reports*, 3:3233, 2013.

[13] J. Scott Bunch, Arend M. van der Zande, Scott S. Verbridge, Ian W. Frank, David M. Tanenbaum, Jeevak M. Parpia, Harold G. Craighead, and Paul L. McEuen. Electromechanical resonators from graphene sheets. *Science*, 315(5811):490–493, 2007.

[14] V.E. Calado, Shou-En Zhu, Srijit Goswami, Qiang Xu, Kenji Watanabe, T. Taniguchi, G.C.A.M. Janssen, and L.M.K. Vandersypen. Ballistic transport in graphene grown by chemical vapor deposition. *Applied Physics Letters*, 104(2):023103, 2014.

[15] I. Calizo, A.A. Balandin, W. Bao, F. Miao, and C.N. Lau. Temperature dependence of the Raman spectra of graphene and graphene multilayers. *Nano Letters*, 7(9):2645–2649, 2007.

[16] Irene Calizo, Igor Bejenari, Muhammad Rahman, Guanxiong Liu, and Alexander A. Balandin. Ultraviolet Raman spectroscopy of single and multi-layer graphene. *arXiv:0903.1922*, 2009.

[17] L. Gustavo Cançado, A. Jorio, E.H. Martins Ferreira, F. Stavale, C.A. Achete, R.B. Capaz, M.V.O. Moutinho, A. Lombardo, T.S. Kulmala, and A.C. Ferrari. Quantifying defects in graphene via Raman spectroscopy at different excitation energies. *Nano Letters*, 11(8):3190–3196, 2011.

[18] Andrea Candini, Svetlana Klyatskaya, Mario Ruben, Wolfgang Wernsdorfer, and Marco Affronte. Graphene spintronic devices with molecular nanomagnets. *Nano Letters*, 11(7):2634–2639, 2011.

[19] C. Casiraghi, S. Pisana, K.S. Novoselov, A.K. Geim, and A.C. Ferrari. Raman fingerprint of charged impurities in graphene. *Applied Physics Letters*, 91(23):233108, 2007.

[20] Kevin T. Chan, J.B. Neaton, and Marvin L. Cohen. First-principles study of metal adatom adsorption on graphene. *Physical Review B*, 77(23):235430, 2008.

[21] Vadim V. Cheianov and Vladimir I. Fal'ko. Friedel oscillations, impurity scattering, and temperature dependence of resistivity in graphene. *Physical Review Letters*, 97(22):226801, 2006.

[22] Chung Wei Chen, Fan Ren, Gou-Chung Chi, Sheng-Chun Hung, Y.P. Huang, Jihyun Kim, Ivan I. Kravchenko, and Stephen J. Pearton. UV ozone treatment for improving contact resistance on graphene. *Journal of Vacuum Science & Technology B*, 30(6):060604, 2012.

[23] J.-H. Chen, C. Jang, M. Ishigami, S. Xiao, W.. Cullen, E.D. Williams, and M.S. Fuhrer. Diffusive charge transport in graphene on SiO_2. *Solid State Communications*, 149(27):1080–1086, 2009.

[24] Jian-Hao Chen, Liang Li, William G. Cullen, Ellen D. Williams, and Michael S. Fuhrer. Tunable Kondo effect in graphene with defects. *Nature Physics*, 7(7):535–538, 2011.

[25] Isaac Childres, Luis A. Jauregui, Wonjun Park, Helin Cao, and Yong P. Chen. Raman spectroscopy of graphene and related materials. *New Developments in Photon and Materials Research*, 1, 2013.

[26] Anindya Das, S. Pisana, B. Chakraborty, S. Piscanec, S.K. Saha, U.V. Waghmare, K.S. Novoselov, H.R. Krishnamurthy, A.K. Geim, A.C. Ferrari, and A.K. Sood. Monitoring dopants by Raman scattering in an electrochemically top-gated graphene transistor. *Nature Nanotechnology*, 3(4):210–215, 2008.

[27] Walt A. de Heer, Claire Berger, Xiaosong Wu, Mike Sprinkle, Yike Hu, Ming Ruan, Joseph A. Stroscio, Phillip N. First, Robert Haddon, Benjamin Piot, Clément Faugeras, Marek Potemski, and Jeong-Sun Moon. Epitaxial graphene electronic structure and transport. *Journal of Physics D: Applied Physics*, 43(37):374007, 2010.

[28] R.S. Deacon, K.-C. Chuang, R.J. Nicholas, KS Novoselov, and A.K. Geim. Cyclotron resonance study of the electron and hole velocity in graphene monolayers. *Physical Review B*, 76(8):081406, 2007.

[29] Cory R. Dean, Andrea F. Young, Inanc Meric, Chris Lee, Lei Wang, S. Sorgenfrei, K. Watanabe, T. Taniguchi, P. Kim, K.L. Shepard, and J. Hone. Boron nitride substrates for high-quality graphene electronics. *Nature Nanotechnology*, 5(10):722–726, 2010.

[30] R. Dengler. Self inductance of a wire loop as a curve integral. *Advanced Electromagnetics*, 5(1):1–8, 2016.

[31] Xu Du, Ivan Skachko, Anthony Barker, and Eva Y Andrei. Approaching ballistic transport in suspended graphene. *Nature Nanotechnology*, 3(8):491–495, 2008.

[32] Akira Endo, Fumio Komori, Kouhei Morita, Takashi Kajiwara, and Satoru Tanaka. Highly anisotropic parallel conduction in the stepped substrate of epitaxial graphene grown on vicinal SiC. *Journal of Low Temperature Physics*, 179(3-4):237–250, 2015.

[33] Chris P. Ewels, Gregory Van Lier, Jean-Christophe Charlier, Malcolm I. Heggie, and Patrick R. Briddon. Pattern formation on carbon nanotube surfaces. *Physical Review Letters*, 96(21):216103, 2006.

[34] Jaroslav Fabian and S. Das Sarma. Spin relaxation of conduction electrons. *Journal of Vacuum Science & Technology B*, 17(4):1708–1715, 1999.

[35] Vladimir I. Fal'ko, K. Kechedzhi, and E. McCann. Weak localization in graphene. *Solid State Communications*, 143(1-2):33–38, 2007.

[36] Tian Fang, Aniruddha Konar, Huili Xing, and Debdeep Jena. Carrier statistics and quantum capacitance of graphene sheets and ribbons. *Applied Physics Letters*, 91(9):092109, 2007.

[37] Damon B. Farmer, Roksana Golizadeh-Mojarad, Vasili Perebeinos, Yu-Ming Lin, George S. Tulevski, James C. Tsang, and Phaedon Avouris. Chemical doping and electron-hole conduction asymmetry in graphene devices. *Nano Letters*, 9(1):388–392, 2008.

[38] A.C. Ferrari, J.C. Meyer, V. Scardaci, C. Casiraghi, Michele Lazzeri, Francesco Mauri, S. Piscanec, Da Jiang, K.S. Novoselov, S. Roth, and A.K. Geim. Raman spectrum of graphene and graphene layers. *Physical Review Letters*, 97(18):187401, 2006.

[39] Andrea C. Ferrari. Raman spectroscopy of graphene and graphite: Disorder, electron-phonon coupling, doping and nonadiabatic effects. *Solid State Communications*, 143(1):47–57, 2007.

[40] Lars Fritz and Matthias Vojta. The physics of Kondo impurities in graphene. *Reports on Progress in Physics*, 76(3):032501, 2013.

[41] Andre K. Geim and Konstantin S. Novoselov. The rise of graphene. *Nature Materials*, 6(3):183–191, 2007.

[42] Filippo Giannazzo, Sushant Sonde, Raffaella Lo Nigro, Emanuele Rimini, and Vito Raineri. Mapping the density of scattering centers limiting the electron mean free path in graphene. *Nano Letters*, 11(11):4612–4618, 2011.

[43] G. Giovannetti, P.A. Khomyakov, G. Brocks, V.M. Karpan, J. van den Brink, and P.J. Kelly. Doping graphene with metal contacts. *Physical Review Letters*, 101(2):026803, 2008.

[44] M. Gmitra, S. Konschuh, C. Ertler, C. Ambrosch-Draxl, and J. Fabian. Band-structure topologies of graphene: Spin-orbit coupling effects from first principles. *Physical Review B*, 80(23):235431, 2009.

[45] Héctor González-Herrero, José M. Gómez-Rodríguez, Pierre Mallet, Mohamed Moaied, Juan José Palacios, Carlos Salgado, Miguel M. Ugeda, Jean-Yves Veuillen, Félix Yndurain, and Iván Brihuega. Atomic-scale control of graphene magnetism by using hydrogen atoms. *Science*, 352(6284):437–441, 2016.

[46] A.M. Goossens, V.E. Calado, A. Barreiro, K. Watanabe, T. Taniguchi, and L.M.K. Vandersypen. Mechanical cleaning of graphene. *Applied Physics Letters*, 100(7):073110, 2012.

[47] F. Guinea, Baruch Horovitz, and P. Le Doussal. Gauge field induced by ripples in graphene. *Physical Review B*, 77(20):205421, 2008.

[48] V.P. Gusynin and S.G. Sharapov. Unconventional integer quantum Hall effect in graphene. *Physical Review Letters*, 95(14):146801, 2005.

[49] Johannes Güttinger, T. Frey, C. Stampfer, T. Ihn, and K. Ensslin. Spin states in graphene quantum dots. *Physical Review Letters*, 105(11):116801, 2010.

[50] Wei Han and Roland K. Kawakami. Spin relaxation in single-layer and bilayer graphene. *Physical Review Letters*, 107(4):047207, 2011.

[51] Wei Han, Roland K. Kawakami, Martin Gmitra, and Jaroslav Fabian. Graphene spintronics. *Nature Nanotechnology*, 9(10):794–807, 2014.

[52] Wei Han, K.M. McCreary, K. Pi, W.H. Wang, Yan Li, H. Wen, J.R. Chen, and R.K. Kawakami. Spin transport and relaxation in graphene. *Journal of Magnetism and Magnetic Materials*, 324(4):369–381, 2012.

[53] Wei Han, K. Pi, W. Bao, K.M. McCreary, Yan Li, W.H. Wang, C.N. Lau, and R.K. Kawakami. Electrical detection of spin precession in single layer graphene spin valves with transparent contacts. *Applied Physics Letters*, 94(22):222109, 2009.

[54] Jinseong Heo, Hyun-Jong Chung, Sung-Hoon Lee, H. Yang, D.H. Seo, J.K. Shin, U-In Chung, S. Seo, E.H. Hwang, and S. Das Sarma. Nonmonotonic temperature dependent transport in graphene grown by chemical vapor deposition. *Physical Review B*, 84(3):035421, 2011.

[55] Michael Her, Ryan Beams, and Lukas Novotny. Graphene transfer with reduced residue. *Physics Letters A*, 377(21):1455–1458, 2013.

[56] Michael Hilke, Mathieu Massicotte, Eric Whiteway, and Victor Yu. Weak localization in graphene: Theory, simulations, and experiments. *The Scientific World Journal*, 2014, 2014.

[57] Yuan Huang, Eli Sutter, Norman N. Shi, Jiabao Zheng, Tianzhong Yang, Dirk Englund, Hong-Jun Gao, and Peter Sutter. Reliable exfoliation of large-area high-quality flakes of graphene and other two-dimensional materials. *ACS Nano*, 9(11):10612–10620, 2015.

[58] D.L. Huber, R.R. Urbano, M.S. Sercheli, and C Rettori. Fluctuating field model for conduction electron spin resonance in graphite. *Physical Review B*, 70(12):125417, 2004.

[59] Daniel Huertas-Hernando, F. Guinea, and Arne Brataas. Spin-orbit coupling in curved graphene, fullerenes, nanotubes, and nanotube caps. *Physical Review B*, 74(15):155426, 2006.

[60] E.H. Hwang, S. Adam, and S. Das Sarma. Carrier transport in two-dimensional graphene layers. *Physical Review Letters*, 98(18):186806, 2007.

[61] E.H. Hwang, S. Adam, and S. Das Sarma. Transport in chemically doped graphene in the presence of adsorbed molecules. *Physical Review B*, 76(19):195421, 2007.

[62] Masa Ishigami, J.H. Chen, W.G. Cullen, M.S. Fuhrer, and E.D. Williams. Atomic structure of graphene on SiO_2. *Nano Letters*, 7(6):1643–1648, 2007.

[63] Yang Jie, Jia Kunpeng, Su Yajuan, Chen Yang, and Zhao Chao. Hysteresis analysis of graphene transistor under repeated test and gate voltage stress. *Journal of Semiconductors*, 35(9):094003, 2014.

[64] Sanghyun Jo, Dong-Keun Ki, Dongchan Jeong, Hu-Jong Lee, and Stefan Kettemann. Spin relaxation properties in graphene due to its linear dispersion. *Physical Review B*, 84(7):075453, 2011.

[65] P. Joshi, H.E. Romero, A.T. Neal, V.K. Toutam, and S.A. Tadigadapa. Intrinsic doping and gate hysteresis in graphene field effect devices fabricated on SiO_2 substrates. *Journal of Physics: Condensed Matter*, 22(33):334214, 2010.

[66] C. Józsa, T. Maassen, M. Popinciuc, P.J. Zomer, A. Veligura, H.T. Jonkman, and B.J. van Wees. Linear scaling between momentum and spin scattering in graphene. *Physical Review B*, 80(24):241403, 2009.

[67] S. Just, S. Zimmermann, V. Kataev, B. Büchner, M. Pratzer, and M. Morgenstern. Preferential antiferromagnetic coupling of vacancies in graphene on SiO_2: Electron spin resonance and scanning tunneling spectroscopy. *Physical Review B*, 90(12):125449, 2014.

[68] Charles L. Kane and Eugene J. Mele. Quantum spin Hall effect in graphene. *Physical Review Letters*, 95(22):226801, 2005.

[69] M.I. Katsnelson and A.K. Geim. Electron scattering on microscopic corrugations in graphene. *Philosophical Transactions of the Royal Society of London A: Mathematical, Physical and Engineering Sciences*, 366(1863):195–204, 2008.

[70] K.F. Kelly, I.W. Chiang, E.T. Mickelson, R.H. Hauge, J.L. Margrave, X. Wang, G.E. Scuseria, C. Radloff, and N.J. Halas. Insight into the mechanism of sidewall functionalization of single-walled nanotubes: An STM study. *Chemical Physics Letters*, 313(3):445–450, 1999.

[71] D.V. Khveshchenko. Electron localization properties in graphene. *Physical Review Letters*, 97(3):036802, 2006.

[72] Dong-Keun Ki, Dongchan Jeong, Jae-Hyun Choi, Hu-Jong Lee, and Kee-Su Park. Inelastic scattering in a monolayer graphene sheet: A weak-localization study. *Physical Review B*, 78(12):125409, 2008.

[73] Eun-Ah Kim and A.H. Castro Neto. Graphene as an electronic membrane. *EPL (Europhysics Letters)*, 84(5):57007, 2008.

[74] Hyun-Jung Kim and Jun-Hyung Cho. Fluorine-induced local magnetic moment in graphene: A hybrid DFT study. *Physical Review B*, 87(17):174435, 2013.

[75] Seyoung Kim, Insun Jo, D.C. Dillen, D.A. Ferrer, Babak Fallahazad, Zhen Yao, S.K. Banerjee, and Emanuel Tutuc. Direct measurement of the Fermi energy in graphene using a double-layer heterostructure. *Physical Review Letters*, 108(11):116404, 2012.

[76] Sergej Konschuh, Martin Gmitra, and Jaroslav Fabian. Tight-binding theory of the spin-orbit coupling in graphene. *Physical Review B*, 82(24):245412, 2010.

[77] Pawan Kumar and Amit Kumar. Carrier type modulation in current annealed graphene layers. *Applied Physics Letters*, 104(8):083517, 2014.

[78] E.V. Kurganova, H.J. van Elferen, A. McCollam, L.A. Ponomarenko, K.S. Novoselov, A. Veligura, B.J. van Wees, J.C. Maan, and U. Zeitler. Spin splitting in graphene studied by means of tilted magnetic-field experiments. *Physical Review B*, 84(12):121407, 2011.

[79] Myrsini Lafkioti, Benjamin Krauss, Timm Lohmann, Ute Zschieschang, Hagen Klauk, Klaus v. Klitzing, and Jurgen H. Smet. Graphene on a hydrophobic substrate: Doping reduction and hysteresis suppression under ambient conditions. *Nano Letters*, 10(4):1149–1153, 2010.

[80] Jooho Lee, Yongsung Kim, Hyeon-Jin Shin, ChangSeung Lee, Dongwook Lee, Chang-Yul Moon, Juhwan Lim, and Seong Chan Jun. Clean transfer of graphene and its effect on contact resistance. *Applied Physics Letters*, 103(10):103104, 2013.

[81] Wei Sun Leong, Hao Gong, and John T.L. Thong. Low-contact-resistance graphene devices with nickel-etched-graphene contacts. *ACS Nano*, 8(1):994–1001, 2013.

[82] N. Levy, S.A. Burke, K.L. Meaker, M. Panlasigui, A. Zettl, F. Guinea, A.H. Castro Neto, and M.F. Crommie. Strain-induced pseudo-magnetic fields greater than 300 tesla in graphene nanobubbles. *Science*, 329(5991):544–547, 2010.

[83] Qiuzi Li, EH Hwang, and S. Das Sarma. Disorder-induced temperature-dependent transport in graphene: Puddles, impurities, activation, and diffusion. *Physical Review B*, 84(11):115442, 2011.

[84] Wei Li, Yiran Liang, Dangmin Yu, Lianmao Peng, Kurt P. Pernstich, Tian Shen, A.R. Hight Walker, Guangjun Cheng, Christina A. Hacker, Curt A. Richter, Qiliang Li, David J. Gundlach, and Xuelei Liang. Ultraviolet/ozone treatment to reduce metal-graphene contact resistance. *Applied Physics Letters*, 102(18):183110, 2013.

[85] Xuesong Li, Weiwei Cai, Jinho An, Seyoung Kim, Junghyo Nah, Dongxing Yang, Richard Piner, Aruna Velamakanni, Inhwa Jung, Emanuel Tutuc, Sanjay K. Banerjee, Luigi Colombo, and Rodney S. Ruoff. Large-area synthesis of high-quality and uniform graphene films on copper foils. *Science*, 324(5932):1312–1314, 2009.

[86] Xuelei Liang, Brent A. Sperling, Irene Calizo, Guangjun Cheng, Christina Ann Hacker, Qin Zhang, Yaw Obeng, Kai Yan, Hailin Peng, Qiliang Li, Xiaoxiao Zhu, Hu Yuan, Angela R. Hight Walker, Zhongfan Liu, Lian-mao Peng, and Curt A. Richter. Toward clean and crackless transfer of graphene. *ACS Nano*, 5(11):9144–9153, 2011.

[87] Lili Liu, Miaoqing Qing, Yibo Wang, and Shimou Chen. Defects in graphene: Generation, healing, and their effects on the properties of graphene: A review. *Journal of Materials Science & Technology*, 31(6):599–606, 2015.

[88] Ming Liu, Xiaobo Yin, Erick Ulin-Avila, Baisong Geng, Thomas Zentgraf, Long Ju, Feng Wang, and Xiang Zhang. A graphene-based broadband optical modulator. *Nature*, 474(7349):64–67, 2011.

[89] Mark B. Lundeberg and Joshua A. Folk. Spin-resolved quantum interference in graphene. *Nature Physics*, 5(12):894–897, 2009.

[90] Birong Luo, Patrick R. Whelan, Abhay Shivayogimath, David M.A. Mackenzie, Peter Boggild, and Timothy J. Booth. Copper oxidation through nucleation sites of chemical vapor deposited graphene. *Chemistry of Materials*, 2016.

[91] Timothy J. Lyon, Jonas Sichau, August Dorn, Alba Centeno, Amaia Pesquera, Amaia Zurutuza, and Robert H. Blick. Probing electron spin resonance in monolayer graphene. *arXiv:1611.08782*, 2016.

[92] Timothy J. Lyon, Jonas Sichau, August Dorn, Amaia Zurutuza, Amaia Pesquera, Alba Centeno, and Robert H. Blick. High-quality large-area graphene for device applications. *arXiv:1611.06199*, 2016.

[93] Yuchen Ma, P.O. Lehtinen, Adam S. Foster, and R.M. Nieminen. Magnetic properties of vacancies in graphene and single-walled carbon nanotubes. *New Journal of Physics*, 6(1):68, 2004.

[94] D.L. Mafra, G. Samsonidze, L.M. Malard, D.C. Elias, J.C. Brant, F. Plentz, E.S. Alves, and M.A. Pimenta. Determination of LA and TO phonon dispersion relations of graphene near the Dirac point by double resonance Raman scattering. *Physical Review B*, 76(23):233407, 2007.

[95] Ramesh G. Mani, John Hankinson, Claire Berger, and Walter A. de Heer. Observation of resistively detected hole spin resonance and zero-field pseudo-spin splitting in epitaxial graphene. *Nature Communications*, 3:996, 2012.

[96] Luiz GP Martins, Yi Song, Tingying Zeng, Mildred S. Dresselhaus, Jing Kong, and Paulo T. Araujo. Direct transfer of graphene onto flexible substrates. *Proceedings of the National Academy of Sciences*, 110(44):17762–17767, 2013.

[97] K. Matsubara, T. Tsuzuku, and K. Sugihara. Electron spin resonance in graphite. *Physical Review B*, 44(21):11845, 1991.

[98] Edward McCann, K. Kechedzhi, Vladimir I. Fal'ko, H. Suzuura, T. Ando, and B.L. Altshuler. Weak-localization magnetoresistance and valley symmetry in graphene. *Physical Review Letters*, 97(14):146805, 2006.

[99] Jannik C. Meyer, Andre K. Geim, Mikhail I. Katsnelson, Konstantin S. Novoselov, Tim J. Booth, and Siegmar Roth. The structure of suspended graphene sheets. *Nature*, 446(7131):60–63, 2007.

[100] Hongki Min, J.E. Hill, Nikolas A. Sinitsyn, B.R. Sahu, Leonard Kleinman, and Allan H. MacDonald. Intrinsic and Rashba spin-orbit interactions in graphene sheets. *Physical Review B*, 74(16):165310, 2006.

[101] Silvia Minke, Jan Bundesmann, D. Weiss, and J. Eroms. Phase coherent transport in graphene nanoribbons and graphene nanoribbon arrays. *Physical Review B*, 86(15):155403, 2012.

[102] T.M.G. Mohiuddin, A. Lombardo, R.R. Nair, A. Bonetti, G. Savini, R. Jalil, N. Bonini, D.M. Basko, C. Galiotis, N. Marzari, K.S. Novoselov, A.K. Geim, and A.C. Ferrari. Uniaxial strain in graphene by Raman spectroscopy: G peak splitting, Grüneisen parameters, and sample orientation. *Physical Review B*, 79(20):205433, 2009.

[103] S.V. Morozov, K.S. Novoselov, M.I. Katsnelson, F. Schedin, L.A. Ponomarenko, D. Jiang, and A.K. Geim. Strong suppression of weak localization in graphene. *Physical Review Letters*, 97(1):016801, 2006.

[104] Joel Moser, Amelia Barreiro, and Adrian Bachtold. Current-induced cleaning of graphene. *Applied Physics Letters*, 91(16):163513, 2007.

[105] Joel Moser, Haihua Tao, Stephan Roche, F. Alzina, C.M. Sotomayor Torres, and Adrian Bachtold. Magnetotransport in disordered graphene exposed to ozone: From weak to strong localization. *Physical Review B*, 81(20):205445, 2010.

[106] K. Nagashio, T. Nishimura, K. Kita, and A. Toriumi. Metal/graphene contact as a performance killer of ultra-high mobility graphene analysis of intrinsic mobility and contact resistance. In *2009 IEEE International Electron Devices Meeting (IEDM)*, pages 1–4. IEEE, 2009.

[107] K. Nagashio, T. Yamashita, T. Nishimura, K. Kita, and A. Toriumi. Electrical transport properties of graphene on SiO_2 with specific surface structures. *Journal of Applied Physics*, 110(2):024513, 2011.

[108] Kosuke Nagashio and Akira Toriumi. Density-of-states limited contact resistance in graphene field-effect transistors. *Japanese Journal of Applied Physics*, 50(7R):070108, 2011.

[109] Rahul Raveendran Nair, Peter Blake, Alexander N. Grigorenko, Konstantin S. Novoselov, Tim J. Booth, Tobias Stauber, Nuno M.R. Peres, and Andre K. Geim. Fine structure constant defines visual transparency of graphene. *Science*, 320(5881):1308–1308, 2008.

[110] R.R. Nair, M. Sepioni, I-Ling Tsai, O. Lehtinen, J. Keinonen, A.V. Krasheninnikov, T. Thomson, A.K. Geim, and I.V. Grigorieva. Spin-half paramagnetism in graphene induced by point defects. *Nature Physics*, 8(3):199–202, 2012.

[111] R.R. Nair, I.-L. Tsai, M. Sepioni, O. Lehtinen, J. Keinonen, A.V. Krasheninnikov, A.H. Castro Neto, M.I. Katsnelson, A.K. Geim, and I.V. Grigorieva. Dual origin of defect magnetism in graphene and its reversible switching by molecular doping. *Nature Communications*, 4, 2013.

[112] B.R.K. Nanda, M. Sherafati, Z.S. Popović, and S. Satpathy. Electronic structure of the substitutional vacancy in graphene: Density-functional and Green's function studies. *New Journal of Physics*, 14(8):083004, 2012.

[113] Anindya Nath, Andrew D. Koehler, Glenn G. Jernigan, Virginia D. Wheeler, Jennifer K. Hite, Sandra C. Hernández, Zachary R. Robinson, Nelson Y. Garces, Rachael L. Myers-Ward, Charles R. Eddy Jr., D.K. Gaskill, and M.V. Rao. Achieving clean epitaxial graphene surfaces suitable for device applications by improved lithographic process. *Applied Physics Letters*, 104(22):224102, 2014.

[114] Osama M. Nayfeh, Stephen Kilpatrick, and Madan Dubey. Majority and minority carrier mobility behavior and device modeling of doped CVD monolayer graphene transistors. In *Device Research Conference (DRC), 2010*, pages 83–84. IEEE, 2010.

[115] N. Nestle, G. Denninger, M. Vidal, C. Weinzierl, K. Brunner, K. Eberl, and K. von Klitzing. Electron spin resonance on a two-dimensional electron gas. *Physical Review B*, 56(8):R4359, 1997.

[116] A.H. Castro Neto, F. Guinea, N.M.R. Peres, Kostya S. Novoselov, and Andre K. Geim. The electronic properties of graphene. *Reviews of Modern Physics*, 81(1):109, 2009.

[117] Andreas Ney, Pagona Papakonstantinou, Ajay Kumar, Nai-Gui Shang, and Nianhua Peng. Irradiation enhanced paramagnetism on graphene nanoflakes. *Applied Physics Letters*, 99(10):102504, 2011.

[118] Zhen Hua Ni, Ting Yu, Yun Hao Lu, Ying Ying Wang, Yuan Ping Feng, and Ze Xiang Shen. Uniaxial strain on graphene: Raman spectroscopy study and band-gap opening. *ACS Nano*, 2(11):2301–2305, 2008.

[119] Konstantin S. Novoselov, Z. Jiang, Y. Zhang, S.V. Morozov, H.L. Stormer, U. Zeitler, J.C. Maan, G.S. Boebinger, P. Kim, and A.K. Geim. Room-temperature quantum Hall effect in graphene. *Science*, 315(5817):1379–1379, 2007.

[120] Kostya S. Novoselov, Andre K. Geim, Sergei V. Morozov, D. Jiang, Y. Zhang, Sergey V. Dubonos, Irina V. Grigorieva, and Alexandr A. Firsov. Electric field effect in atomically thin carbon films. *Science*, 306(5696):666–669, 2004.

[121] K.S. Novoselov, A.K. Geim, S.V. Morozov, D. Jiang, M.I. Katsnelson, I.V. Grigorieva, S.V. Dubonos, and A.A. Firsov. Two-dimensional gas of massless Dirac fermions in graphene. *Nature*, 438(7065):197–200, 2005.

[122] Chuhei Oshima and Ayato Nagashima. Ultra-thin epitaxial films of graphite and hexagonal boron nitride on solid surfaces. *Journal of Physics: Condensed Matter*, 9(1):1, 1997.

[123] P.M. Ostrovsky, I.V. Gornyi, and A.D. Mirlin. Electron transport in disordered graphene. *Physical Review B*, 74(23):235443, 2006.

[124] Sílvia Osuna, Miquel Torrent-Sucarrat, Miquel Sola, Paul Geerlings, Christopher P. Ewels, and Gregory Van Lier. Reaction mechanisms for graphene and carbon nanotube fluorination. *The Journal of Physical Chemistry C*, 114(8):3340–3345, 2010.

[125] Vasili Perebeinos and Phaedon Avouris. Inelastic scattering and current saturation in graphene. *Physical Review B*, 81(19):195442, 2010.

[126] Dmytro Pesin and Allan H. MacDonald. Spintronics and pseudospintronics in graphene and topological insulators. *Nature Materials*, 11(5):409–416, 2012.

[127] Nicholas Petrone, Cory R. Dean, Inanc Meric, Arend M. van der Zande, Pinshane Y. Huang, Lei Wang, David Muller, Kenneth L. Shepard, and James Hone. Chemical vapor deposition-derived graphene with electrical performance of exfoliated graphene. *Nano Letters*, 12(6):2751–2756, 2012.

[128] K. Pi, Wei Han, K.M. McCreary, A.G. Swartz, Yan Li, and R.K. Kawakami. Manipulation of spin transport in graphene by surface chemical doping. *Physical Review Letters*, 104(18):187201, 2010.

[129] N.A. Pike and D. Stroud. Graphene with adatoms: Tuning the magnetic moment with an applied voltage. *Applied Physics Letters*, 105(5):052404, 2014.

[130] Luiz Gustavo Pimenta, Yi Song, Tingying Zeng, Mildred Dresselhaus, Jing Kong, and Paulo Araujo. Direct transfer of graphene onto flexible substrates. In *APS Meeting Abstracts*, volume 1, page 37009, 2014.

[131] A. Pirkle, J. Chan, A. Venugopal, D. Hinojos, C.W. Magnuson, S. McDonnell, L. Colombo, E.M. Vogel, R.S. Ruoff, and R.M. Wallace. The effect of chemical residues on the physical and electrical properties of chemical vapor deposited graphene transferred to SiO_2. *Applied Physics Letters*, 99(12):122108, 2011.

[132] Andrew J. Pollard, Barry Brennan, Helena Stec, Bonnie J. Tyler, Martin P. Seah, Ian S. Gilmore, and Debdulal Roy. Quantitative characterization of defect size in graphene using Raman spectroscopy. *Applied Physics Letters*, 105(25):253107, 2014.

[133] M. Popinciuc, C. Józsa, P.J. Zomer, N. Tombros, A. Veligura, H.T. Jonkman, and B.J. van Wees. Electronic spin transport in graphene field-effect transistors. *Physical Review B*, 80(21):214427, 2009.

[134] Peter Rickhaus, Romain Maurand, Ming-Hao Liu, Markus Weiss, Klaus Richter, and Christian Schönenberger. Ballistic interferences in suspended graphene. *Nature Communications*, 4, 2013.

[135] Joshua A. Robinson, Michael LaBella, Mike Zhu, Matt Hollander, Richard Kasarda, Zachary Hughes, Kathleen Trumbull, Randal Cavalero, and David Snyder. Contacting graphene. *Applied Physics Letters*, 98(5):053103, 2011.

[136] Stephan Roche and Sergio O. Valenzuela. Graphene spintronics: Puzzling controversies and challenges for spin manipulation. *Journal of Physics D: Applied Physics*, 47(9):094011, 2014.

[137] S. Russo, M.F. Craciun, M. Yamamoto, A.F. Morpurgo, and S. Tarucha. Contact resistance in graphene-based devices. *Physica E: Low-dimensional Systems and Nanostructures*, 42(4):677–679, 2010.

[138] E.J.G. Santos, Sampsa Riikonen, Daniel Sánchez-Portal, and Andrés Ayuela. Magnetism of single vacancies in rippled graphene. *The Journal of Physical Chemistry C*, 116(13):7602–7606, 2012.

[139] S. Das Sarma, Shaffique Adam, E.H. Hwang, and Enrico Rossi. Electronic transport in two-dimensional graphene. *Reviews of Modern Physics*, 83(2):407, 2011.

[140] Ken-ichi Sasaki, Katsunori Wakabayashi, and Toshiaki Enoki. Polarization dependence of Raman spectra in strained graphene. *Physical Review B*, 82(20):205407, 2010.

[141] Ken-ichi Sasaki, Masayuki Yamamoto, Shuichi Murakami, Riichiro Saito, Mildred S. Dresselhaus, Kazuyuki Takai, Takanori Mori, Toshiaki Enoki, and Katsunori Wakabayashi. Kohn anomalies in graphene nanoribbons. *Physical Review B*, 80(15):155450, 2009.

[142] Thomas Schäpers. *Semiconductor Spintronics*. De Gruyter, 4 2016.

[143] Bernhard Schrader. *Infrared and Raman Spectroscopy: Methods and Applications*. John Wiley & Sons, 1995.

[144] T. Shimada, T. Sugai, C. Fantini, M. Souza, L.G. Cançado, A. Jorio, M.A. Pimenta, R. Saito, A. Grüneis, G. Dresselhaus, Y. Ohno, T. Mizutani, and H. Shinohara. Origin of the 2450cm^{-1} Raman bands in HOPG, single-wall and double-wall carbon nanotubes. *Carbon*, 43(5):1049–1054, 2005.

[145] Charles P. Slichter. *Principles of Magnetic Resonance*. Springer Science & Business Media, 3 edition, 1990.

[146] Jie Song, Fong-Yu Kam, Rui-Qi Png, Wei-Ling Seah, Jing-Mei Zhuo, Geok-Kieng Lim, Peter K.H. Ho, and Lay-Lay Chua. A general method for transferring graphene onto soft surfaces. *Nature Nanotechnology*, 8(5):356–362, 2013.

[147] T. Stauber, N.M.R. Peres, and F. Guinea. Electronic transport in graphene: A semiclassical approach including midgap states. *Physical Review B*, 76(20):205423, 2007.

[148] D. Stein, K.v. Klitzing, and G. Weimann. Electron spin resonance on GaAs-Al_xGa_{1-x} heterostructures. *Physical Review Letters*, 51(2):130, 1983.

[149] Ji Won Suk, Alexander Kitt, Carl W. Magnuson, Yufeng Hao, Samir Ahmed, Jinho An, Anna K. Swan, Bennett B. Goldberg, and Rodney S. Ruoff. Transfer of CVD-grown monolayer graphene onto arbitrary substrates. *ACS Nano*, 5(9):6916–6924, 2011.

[150] Jie Sun, Youngwoo Nam, Niclas Lindvall, Matthew T. Cole, Kenneth B.K. Teo, Yung Woo Park, and August Yurgens. Growth mechanism of graphene on platinum: Surface catalysis and carbon segregation. *Applied Physics Letters*, 104(15):152107, 2014.

[151] Hidekatsu Suzuura and Tsuneya Ando. Crossover from symplectic to orthogonal class in a two-dimensional honeycomb lattice. *Physical Review Letters*, 89(26):266603, 2002.

[152] Y.-W. Tan, Y. Zhang, K. Bolotin, Y. Zhao, S. Adam, E.H. Hwang, S. Das Sarma, H.L. Stormer, and P. Kim. Measurement of scattering rate and minimum conductivity in graphene. *Physical Review Letters*, 99(24):246803, 2007.

[153] Zhenbing Tan, Changling Tan, Li Ma, G.T. Liu, L. Lu, and C.L. Yang. Shubnikov-de Haas oscillations of a single layer graphene under dc current bias. *Physical Review B*, 84(11):115429, 2011.

[154] Khwanchai Tantiwanichapan, Jeff DiMaria, Shayla N. Melo, and Roberto Paiella. Graphene electronics for terahertz electron-beam radiation. *Nanotechnology*, 24(37):375205, 2013.

[155] F.V. Tikhonenko, A.A. Kozikov, A.K. Savchenko, and R.V. Gorbachev. Transition between electron localization and antilocalization in graphene. *Physical Review Letters*, 103(22):226801, 2009.

[156] E. Tiras, S. Ardali, T. Tiras, E. Arslan, S. Cakmakyapan, O. Kazar, Jawad Hassan, Erik Janzén, and E. Ozbay. Effective mass of electron in monolayer graphene: Electron-phonon interaction. *Journal of Applied Physics*, 113(4):043708, 2013.

[157] N. Tombros, S. Tanabe, A. Veligura, C. Jozsa, M. Popinciuc, H.T. Jonkman, and B.J. van Wees. Anisotropic spin relaxation in graphene. *Physical Review Letters*, 101(4):046601, 2008.

[158] Nikolaos Tombros, Csaba Jozsa, Mihaita Popinciuc, Harry T. Jonkman, and Bart J. van Wees. Electronic spin transport and spin precession in single graphene layers at room temperature. *Nature*, 448(7153):571–574, 2007.

[159] Nikolaos Tombros, Alina Veligura, Juliane Junesch, J. Jasper van den Berg, Paul J. Zomer, Magdalena Wojtaszek, Ivan J. Vera Marun, Harry T. Jonkman, and Bart J. van Wees. Large yield production of high mobility freely suspended graphene electronic devices on a polydimethylglutarimide based organic polymer. *Journal of Applied Physics*, 109(9):093702, 2011.

[160] Björn Trauzettel, Denis V. Bulaev, Daniel Loss, and Guido Burkard. Spin qubits in graphene quantum dots. *Nature Physics*, 3(3):192–196, 2007.

[161] Dinh Van Tuan, Frank Ortmann, Aron W. Cummings, David Soriano, and Stephan Roche. Spin dynamics and relaxation in graphene dictated by electron-hole puddles. *Scientific Reports*, 6, 2016.

[162] A.V. Volkov, A.A. Shylau, and I.V. Zozoulenko. Interaction-induced enhancement of g factor in graphene. *Physical Review B*, 86(15):155440, 2012.

[163] Bin Wang and Sokrates T. Pantelides. Magnetic moment of a single vacancy in graphene and semiconducting nanoribbons. *Physical Review B*, 86(16):165438, 2012.

[164] Haomin Wang, Yihong Wu, Chunxiao Cong, Jingzhi Shang, and Ting Yu. Hysteresis of electronic transport in graphene transistors. *ACS Nano*, 4(12):7221–7228, 2010.

[165] S. Wiedmann, H.J. van Elferen, E.V. Kurganova, M.I. Katsnelson, A.J.M. Giesbers, A. Veligura, B.J. van Wees, R.V. Gorbachev, K.S. Novoselov, J.C. Maan, and U. Zeitler. Coexistence of electron and hole transport in graphene. *Physical Review B*, 84(11):115314, 2011.

[166] Fengnian Xia, Thomas Mueller, Roksana Golizadeh-Mojarad, Marcus Freitag, Yu-ming Lin, James Tsang, Vasili Perebeinos, and Phaedon Avouris. Photocurrent imaging and efficient photon detection in a graphene transistor. *Nano Letters*, 9(3):1039–1044, 2009.

[167] Jilin Xia, Fang Chen, Jinghong Li, and Nongjian Tao. Measurement of the quantum capacitance of graphene. *Nature Nanotechnology*, 4(8):505–509, 2009.

[168] Zheng Yan, Jian Lin, Zhiwei Peng, Zhengzong Sun, Yu Zhu, Lei Li, Changsheng Xiang, E. Loïc Samuel, Carter Kittrell, and James M. Tour. Toward the synthesis of wafer-scale single-crystal graphene on copper foils. *ACS Nano*, 6(10):9110–9117, 2012.

[169] Wei Yang, Guorui Chen, Zhiwen Shi, Cheng-Cheng Liu, Lianchang Zhang, Guibai Xie, Meng Cheng, Duoming Wang, Rong Yang, Dongxia Shi, Kenji Watanabe, Takashi Taniguchi, Yugui Yao, Yuanbo Zhang, and Guangyu Zhang. Epitaxial growth of single-domain graphene on hexagonal boron nitride. *Nature Materials*, 12(9):792–797, 2013.

[170] Matthew Yankowitz, Jiamin Xue, and Brian J. LeRoy. Graphene on hexagonal boron nitride. *Journal of Physics: Condensed Matter*, 26(30):303201, 2014.

[171] Yugui Yao, Fei Ye, Xiao-Liang Qi, Shou-Cheng Zhang, and Zhong Fang. Spin-orbit gap of graphene: First-principles calculations. *Physical Review B*, 75(4):041401, 2007.

[172] Oleg V. Yazyev and Lothar Helm. Defect-induced magnetism in graphene. *Physical Review B*, 75(12):125408, 2007.

[173] Qingkai Yu, Luis A. Jauregui, Wei Wu, Robert Colby, Jifa Tian, Zhihua Su, Helin Cao, Zhihong Liu, Deepak Pandey, Dongguang Wei, Ting Fung Chung, Peng Peng, Nathan P. Guisinger, Eric A. Stach, Jiming Bao, Shin-Shem Pei, and Yong P. Chen. Control and characterization of individual grains and grain boundaries in graphene grown by chemical vapour deposition. *Nature Materials*, 10(6):443–449, 2011.

[174] Xining Zang, Qin Zhou, Jiyoung Chang, Yumeng Liu, and Liwei Lin. Graphene and carbon nanotube (CNT) in MEMS/NEMS applications. *Microelectronic Engineering*, 132:192–206, 2015.

[175] Yuanbo Zhang, Yan-Wen Tan, Horst L. Stormer, and Philip Kim. Experimental observation of the quantum Hall effect and Berry's phase in graphene. *Nature*, 438(7065):201–204, 2005.

[176] P.J. Zomer, M.H.D. Guimaraes, N. Tombros, and B.J. van Wees. Long-distance spin transport in high-mobility graphene on hexagonal boron nitride. *Physical Review B*, 86(16):161416, 2012.

[177] Igor Žutić, Jaroslav Fabian, and S. Das Sarma. Spintronics: Fundamentals and applications. *Reviews of Modern Physics*, 76(2):323, 2004.